JUMR

Journal of Undergraduate Materials Research

"The Voice of Future Scientists and Engineers"

FEATURING RESEARCH FROM

IIT, Kanpur
Michigan Tech
NC State
Virginia Tech

GAINING THE MSE EDGE

Students design custom composite arm brace

A Publication of the Department of Materials Science and Engineering at Virginia Tech

Volume 2 | Fall 2006

WELCOME LETTER

Dear Friends,

We have come a long way since our inaugural issue last fall! This past year has been dramatic in terms of the journal's growth—growth in personnel, content, collaboration with other schools and organizations, and the number of undergraduates we hope to reach.

This year, we published papers not only from universities across the country but also from across the globe. The papers featured represent students from schools including Michigan Tech, North Carolina State University, multiple departments within Virginia Tech and the Indian Institute of Technology in Kanpur, India. These papers were chosen based on reviews by graduate students, faculty and industry professionals from across the country.

With its second volume, the journal continues to build on the communication and cooperation between the Departments of English and Materials Science and Engineering (MSE) to increase its impact. *JUMR* fosters cooperation between undergraduate and graduate students. It creates an innovative partnership between liberal arts and engineering, fulfilling the vision of Virginia Tech MSE alumnus Alfred Knobler, whose initiatives inspired the first edition of the *Journal of Undergraduate Materials Research*.

If this past year is any indicator, *JUMR*'s rapid growth will continue to draw national recognition to the research accomplishments of undergraduate students. Papers are currently being accepted for future volumes. Manuscripts will be peer- and professional-reviewed and accepted on a rolling basis with those received before May 4, 2007 being considered for publication in Volume 3.

Again, we hope that this periodical will be a strong voice for the research achievements of undergraduates in the field of materials science, and we thank each of you for helping to make this project a continued success.

Sincerely,

The Editorial Board

Back row (L-R): Navin Manjooran, Chris Bayne, Davis Eichelberger, Carlos Folgar, Morsi Mahmoud, Ben Poquette. **Front row (L-R)**: Steven Kyriakides, Jessica Pritchard, Dan Sheehan, Susan Holt, Christelle Jullian

Materials Science and Engineering
discover what we're made of...

On the cover:
Structure of polypropylene behind former Virginia Tech runningback Cedric Humes wearing a custom polypropylene-based arm brace during a game three weeks after fracturing his arm. Football photograph provided by David Knachel, Virginia Tech.

DISCLAIMER

CONTENTS

FEATURE ARTICLES

OTHER FEATURED DEPARTMENTS

RESEARCH ARTICLES

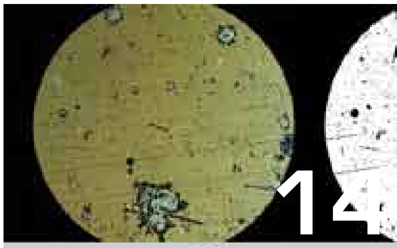

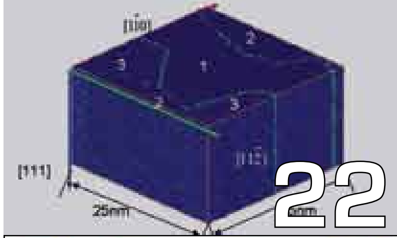

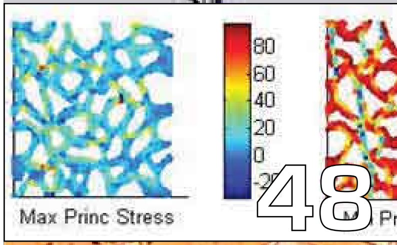

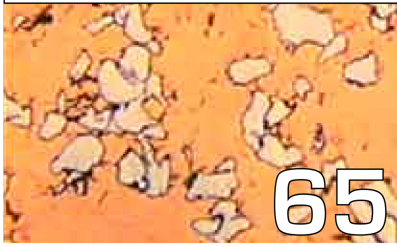

EDITORIAL CREDITS

STUDENT EDITORIAL BOARD

FACULTY EDITORIAL BOARD

FACULTY REVIEWERS

Iver Anderson, *Iowa State University*
Alex Aning, *Virginia Tech*
Stephen Kampe, *Virginia Tech*
Shawn Kelly, *Penn State*
Gary Pickrell, *Virginia Tech*
Jeff Schultz, *Virginia Tech*
William B. Spillman, Jr., *Columbia Gorge Research*
Calvin White, *Michigan Tech*

INDUSTRY REVIEWERS

Mike Bortner, *Nanosonic, Inc.*
John Franklin, *Sandia National Lab*
Matt Hallihan, *Alcoa*
Brian Hyde, *Ball Aerospace*
Abhishek Jaiswal, *Kainos Energy Corp.*
Judson Marte, *General Electric*
Garth Tormoen, *Southwest Research Institute*

GRADUATE STUDENT REVIEWERS

Ted Asare, *Virginia Tech*
Suresh Donthu, *Northwestern University*
Sihlpa Dubey, *University of Alabama*
Dan Giarnola, *Johns Hopkins University*
Mikhail Haurylau, *University of Rochester*
Elizabeth Jeffers, *Virginia Tech*
Jennifer Kauffman, *Clemson University*
Matt Lynch, *Virginia Tech*
Anup Pancholi, *University of Delaware*
Vishal Warke, *University of Alabama*
Briggs White, *University of Florida*

SPECIAL THANKS

David Clark, *Professor and Head*
  Materials Science and Engineering, Virginia Tech
Lucinda Roy, *Professor*
  English, Virginia Tech
Carolyn Rude, *Professor and Chair*
  English, Virginia Tech
Charles “Jack” Dudley, *Professor and Director*
  University Honors Program, Virginia Tech
Sarah Lewis, *Computer Technician*
  Sweet Briar College
Material Advantage (ACerS, AIST, ASM, TMS)
The Materials Research Society
Micron Technology, Inc.
Virginia Tech Center of Excellence in Undergraduate Teaching

Letter from the Department Head

David Clark, Materials Science and Engineering

Dear Students and Colleagues:

First, my sincere thanks to the hard-working editorial board for producing this unique journal. The process of publishing a journal is not simple. Decisions on design, content, reviewer selection, and editing can present significant challenges. At the same time, these challenges can help prepare you for the professional-level publishing that most of you will be involved in throughout your career. Many thanks also to all those groups who contributed to *JUMR* financially, including the VT-Center for Excellence in Undergraduate Teaching, the VT University Honors Program, the Materials Research Society, Material Advantage, Micron Technology, Inc., and of course the Departments of English and of Materials Science and Engineering. We are fortunate to have such strong support for this effort.

Next, congratulations to all the undergraduate authors published in this edition from North Carolina State University, Michigan Technological University, the Indian Institute of Technology-Kanpur, and Virginia Tech. For some of you, this is your first publication in a multi-level, peer- and professional-reviewed journal. As for any journal, papers are accepted based on quality and appropriateness of the subject matter. I am certain that your advisors and fellow researchers are proud of you.

The importance of an undergraduate research experience is well-recognized by universities, companies, and federal funding agencies, such as the National Science Foundation. We are fortunate that research is highly valued within our discipline. In fact, research has been the major driving force for the evolution of most MSE departments. This emphasis allows us to offer our undergraduate students research opportunities that may not be available in other disciplines. In addition to advancing our discipline, these research experiences are extremely valuable in preparing students for the workplace and/or graduate studies.

Many of us encourage our students to submit their research for publication. As a faculty member, I have felt the pride accompanying the acceptance of my students' papers. *JUMR* provides an opportunity for undergraduate students to publish their research in a timely manner.

In summary, on behalf of the editorial board, I encourage undergraduates performing research in materials science and/or engineering from all academic departments to submit manuscripts for review. Publishing in *JUMR* does not preclude publishing your work elsewhere as we require no copyright transfer. *JUMR* provides a voice for the entire materials research community through the work of their strong undergraduate students.

Sincerely,

David Clark

David E. Clark
Professor and Head

Michael Willemann (Fulbright Scholar and COE Outstanding Senior) with Department Head Dr. David Clark

Virginia Tech Materials Science and Engineering Class of 2006

G I MSE EDGE

Engineering Students Design Composite Bracing System for the Virginia Tech Athletic Department

Steven Kyriakides, Materials Science and Engineering

Just three weeks after fracturing a bone in his forearm, the Hokies' star tailback, Cedric Humes, was able to return to his starting role with the help of materials science.

In October of 2005, prototype composite braces for ulna fractures were constructed by a unique alliance that included Virginia Tech's Athletics and Training Departments, Virginia Tech's College of Engineering, and the Virginia Tech/Wake Forest University School for Biomedical Engineering and Sciences (SBES). After Humes was injured during a game on October 8, Mike Goforth, team trainer for the VT football team, met several times with the senior-level MSE/ESM Biomaterials class taught through Virginia Tech's College of Engineering and the linked VT/WFU SBES. Dr. Brian Love, professor of Materials Science and Engineering and instructor of the class, challenged the students to design an alternate bracing system that was much stiffer than the current polypropylene-molded structures. Their findings were organized and distributed to the Athletic Department for future evaluations. Among the suggestions was a uniaxial polypropylene/carbon fiber composite sheeting made by the Fillauer Company of Chattanooga, Tennessee. Since this sheet was made from the same matrix as other bracing materials, it was feasible to mold prototypes using existing molding equipment. Two prototypes were made, one as a bi-directional laminate and one as a uniaxial laminated composite. The resulting stiffness and strength of the laminated structures had not been fully evaluated by game time on October 27, but qualitative testing had shown that these structures were demonstrably stiffer than the current commercial devices already available. By the end of the season, Humes had played five games in six weeks with the brace, performing as though he had never been injured. The students involved were able to see the fruits of their efforts broadcast and recognized across the nation.

With this project being taken up within SBES, the goal is to share the results with trainers and students at Wake Forest. Hopefully, further bracing enhancements will evolve from the efforts of these undergraduate students.

Special thanks go to Lynn Nystrom for her articles on the subject.

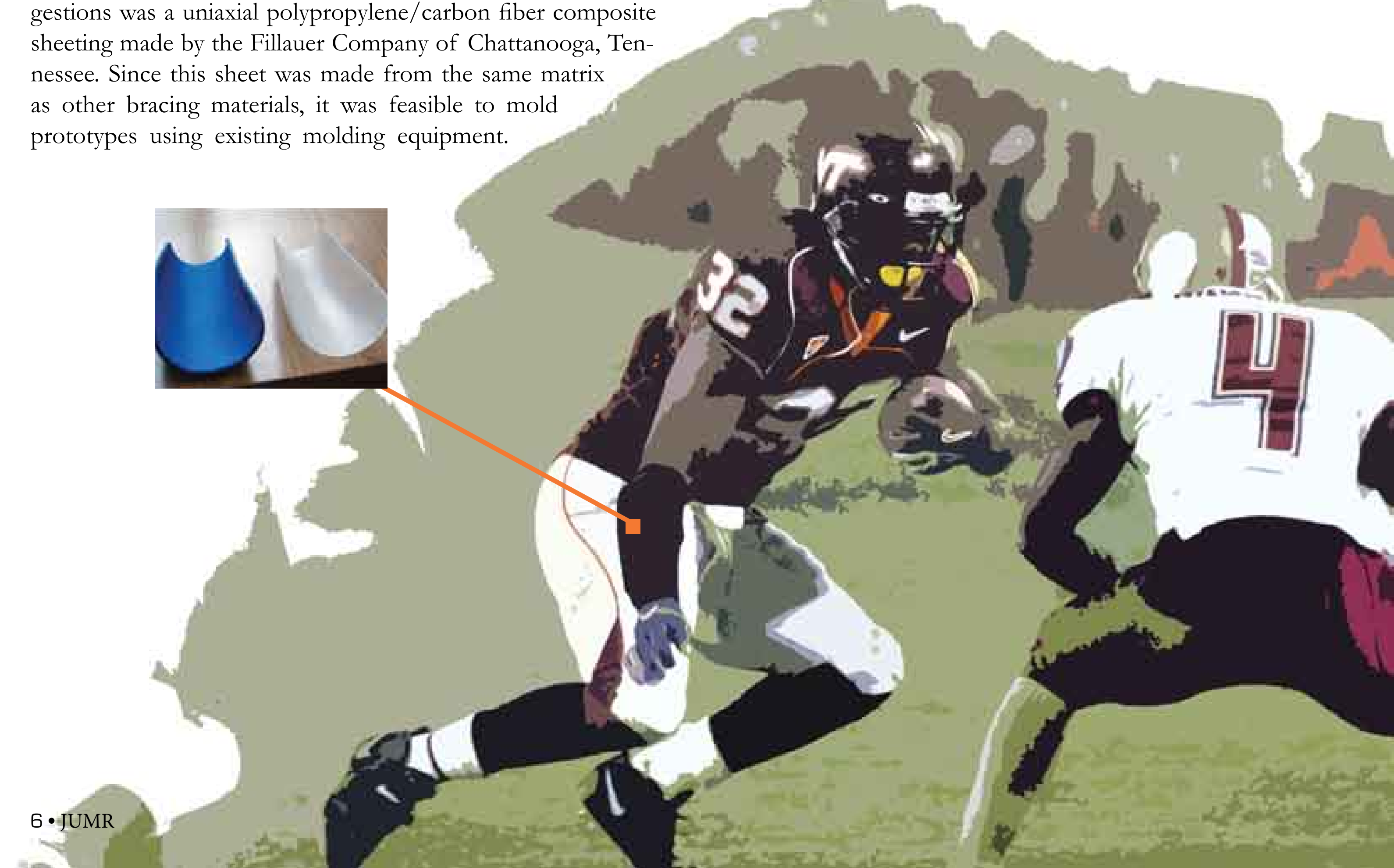

System X: An Advanced Tool for Material Science and Engineering

Carlos Folgar, Materials Science and Engineering

Virginia Tech students now have one of the world's most powerful research tools in their own backyard. In the winter of 2003, Virginia Tech researchers took major strides in supercomputer innovation when their high-profile supercomputer was ranked the third-fastest computer. It was given the name "System X" because it was the first academic supercomputer to pass 10 teraflops, or 10 trillion floating point operations per second. In addition to processing data at high speeds, it is also the cheapest available supercomputer.

System X was initially made of 1100 off-the-shelf Apple Power Mac G5 desktop computers. Presently it consists of the same number of Xserve G5s replacing the normal G5 desktops as shown in Figure 1. These computers have had their memory and speed increased, allowing more accurate predictions to be made in a shorter time.

Figure 1. System X

Materials Science and Engineering (MSE) is one of the fields addressing problems using advanced tools such as System X. One of the main reasons for using these computational resources is that experimental studies cannot provide precise information about the mechanisms that govern different phenomena at the atomic scale. Dr. Diana Farkas is one of the leading MSE professors conducting research projects at the atomic and molecular level with this supercomputer. "Before System X existed, we performed simulations in materials with a hundred thousand atoms—now we can work with hundreds of millions," said Dr. Farkas. Simulation and modeling have reached a much higher level of accuracy in tackling practical problems in materials engineering and other sciences.

One of the applications developed by Dr. Farkas' group has been the simulation of tensile tests on nanocrystalline nickel wires. This work was performed at different strain rates and at room temperature, reaching deformation levels up to 36%. Under these conditions, researchers were able to study the grain growth process by monitoring the evolution of the volume of individual grains for the different strain rates. The results clearly showed that grain growth is fundamentally driven by the stress. These virtual experiments were performed using a conventional molecular dynamics algorithm, and the interaction between the atoms was modeled using an empirical interatomic potential. Figure 2 shows the simulated nanowires after 0, 90, and 270 ps and for deformations of 0, 12, and 36% strain, respectively for a strain rate of 1.33 x 10^9 s^{-1}. The various grains are color coded, showing significant grain growth as the deformation proceeds.

(a) (b) (c)

Figure 2. Nanowires after (a) 0, (b) 90 and (c) 270 ps tensile deformation for a strain rate of $1.33 \times 10^9 s^{-1}$.

Mechanical test simulations on nanocrystalline metals were performed in tension and compression. MSE student Joshua Monk, one of the members of Dr. Farkas' group, said "these simulations have helped in the studies of both the size effect for a 10 nm grain size and the asymmetry of tensile/compressive strength." Figure 3 shows details of dislocations, stacking faults and grain boundaries (green). The blue pixels represent the perfect structure atoms; red represent the surface atoms. This study shows a clear difference in necking performance for the 8- and 18-nm tensile tests. For larger samples, it is energy-efficient to emit dislocations, but at a smaller size, grain boundary sliding is preferred.

In addition, virtual experiments performed by Edward Parker and Peter Gaudreau, MSE students, revealed that mechanical properties of nickel nano-thin films may be different at thicknesses less than 100 nm. These simulations suggest that hardness of the film increases as the film thickness decreases. More information about this significant study can be found in the research article on page 24.

System X has provided researchers an opportunity to perform precise studies of very complex phenomena, especially at the atomic level. These studies are used to establish new trends and correlations that guide designers in the search for novel materials. These achievements are examples of what can be carried out with System X and are the motivation for having such a system. In the coming years, System X will have new capabilities for expanding the frontiers in science and engineering.

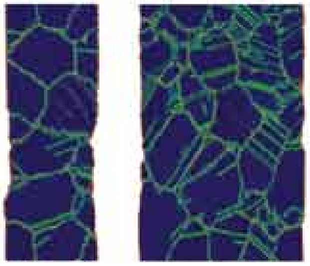

(a) (b)

Figure 3. Tensile tests for (a) 8 nm and (b) 18 nm radii

Nanotechnology: An Outsider's Perspective

Jessica Pritchard, English

Many theorize what the future holds, complete with cliché flying cars and robotic maids, but what if those seemingly imaginary theories became real? Imagine a doctor planning your surgery using a microscopic robot to get into those hard-to-reach parts of your body, or better yet—eating a hamburger or hot dog made from your daily garbage. As crazy and futuristic as it may sound, nanotechnology may hold the key to advancing society into a whole new age of technology. Like most sciences, though, there is a flip side: science at such a tiny level, 10^{-9} meters to be exact, has as many potential dangers as it does advantages.

To put the small domain of nanotechnology into perspective, imagine 1/75,000 the width of a human hair—this is a nanometer.[1] At its basic level, nanotechnology seeks to manipulate and control objects at a molecular level in order to form macroscopic objects, what scientists call the "bottom-up" approach.[2] The nanotechnology community seems split between those who believe chemistry can be controlled and those who do not.[3]

Eric Drexler, the man whom most associate with nanotechnology, earned his Ph.D. in molecular nanotechnology from MIT in 1991.[4] In an article published by Chemical and Engineering News, Drexler has a heated letter of correspondence with Richard Smalley, who won the 1996 Nobel Prize for discovering fullerenes. Drexler says, "As you know, I introduced the term 'nanotechnology' in the mid-1980s to describe advanced capabilities based on molecular assemblers: proposed devices able to guide chemical reactions by positioning reactive molecules with atomic precision."[4] These proposed "molecular assemblers" position atoms and molecules to perform specific reactions in virtually any environment. Smalley, Drexler's primary opponent in the nanotechnology arena, supports the notion that nanotechnology can supply endless advantages to society, but he argues the practicality of molecular assemblers. The main catalyst in their heated debate stems from Smalley's "sticky fingers" and "fat fingers" argument. The "sticky-fingers" argument claims the atom on the end of an assembler's hand will stick to the atom being moved, thus making it virtually impossible to precisely release the atom in the desired spot. Similarly, the "fat fingers" argument claims there is simply not enough room to perform chemical tasks with multiple fingers at a microscopic level.[5] Imagine a person with big fingers trying to dial one number at a time on a telephone—they end up pushing surrounding buttons at the same time because the space on the phone is simply too small for their finger. Drexler tackles Smalley's proposed finger theories with his plan to use ribosomes and enzymes rather than fingers. The problem with this plan, according to Smalley, is that ribosomes and enzymes only function in water, greatly limiting their capabilities.[4] Drexler counters Smalley's accusations by explaining the application of nanofactories, which "use computers for digitally precise control, conveyors for parts transport, and positioning devices of assorted sizes to assemble small parts into larger parts, building macroscopic products."[4]

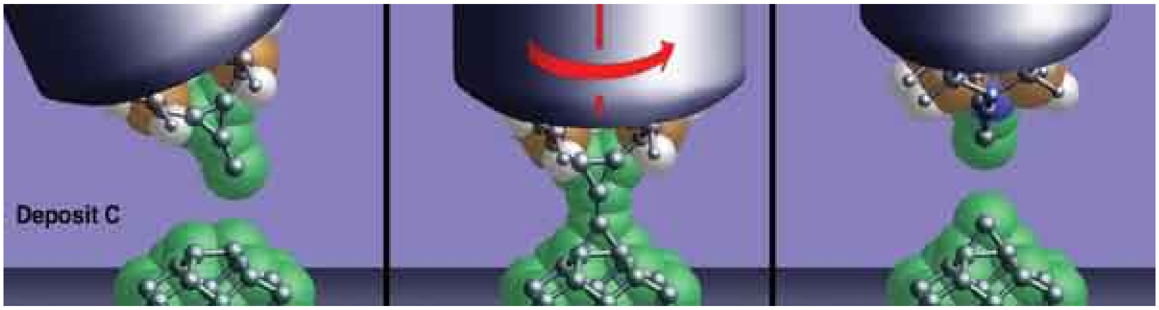

Figure 1. As conceived by Drexler, to deposit carbon, a device moves a vinylidenecarbene along a barrier-free path to insert into the strained alkene, twists 90 degrees to break a pi bond, and then pulls to cleave the remaining sigma bond. Courtesy of K. Eric Drexler.

Beyond the Drexler-Smalley debates, the fundamentals of nanotechnology encompass various potential developments in fields such as medicine and the environment. Nanotechnology devices "can be designed to interact with cells and tissues at a molecular level with a high degree of functional specificity, thus allowing a degree of integration between technology and biological systems not previously attainable."[2] For instance, they could help the brain send controlled messages to prosthetic limbs in accident victims or perhaps even treat infected cells, such as cancer, directly.[6] Such devices could also help clean up natural disasters as well as recycle and reuse materials, helping alleviate natural resource waste. The question then surfaces: what sort of new contaminants will arise from nanotechnology?[7] While we may be able to clean up things such as oil spills, what will happen to the nanoparticles involved in the process? There are many questions still unanswered.

Although nanotechnology may spur many beneficial developments, detrimental aspects, such as new contaminants, have bred a level of skepticism in society. Historically speaking, society has been making scientific developments for centuries—this is nothing new. Given people's ability to go beyond their boundaries, many question when, where, and how we draw the line on the technology we support and the technology we limit. In his article "The Question of Ethics," Donald Bruce postulates that ethical questions could surface if nanotechnology devices are applied to non-medical practices, such as extending an individual's sight into the infrared for stronger night vision. Because there is such an unknown factor in the human body, it becomes difficult to concretely define a healthy patient from an unhealthy patient. If during an annual check-up a doctor has the capacity to warn their patient of a group of malevolent cancer cells they know are incurable when the patient is simply there for a common cold, then this facet of nanotechnology may have revealed too much too soon.[6]

World War II proved no exception with testing human boundaries—though the refinement of the atom brought about nuclear power, it also brought about the nuclear bomb. Nanotechnology may help with military weapons' efficiency, but many fear unconstrained boundaries could lead to microscopic devices used to disassemble military weapons.[8] Similarly, devices having such control at a microscopic level could lead to surveillance invisible to the human eye. Nanotechnology treads a fine line between beneficial developments and developments with the potential to violate personal privacy, leading to gravely unfavorable legal issues. [8] The public paranoia surrounding this up-and-coming science seems to center primarily on its unrestrictive nature and prospective irreversibility. The Gray Goo Scenario, for instance, poses a setting in which a disassembler gets loose in the environment and begins disassembling everything—much like the episode of "Star Trek: The Next Generation" when Wesley's nanites get loose on the ship and destruct everything in their path.[8]

While the dangers of nanotechnology seem to make headlines over its positive developments, there is a level of skepticism in practically everything new and unknown—think back to the beginning phases of cars, planes, and medicine. The key to this developing science rests in establishing boundaries to avoid future misuse and potential disaster. Because there seems to be a lack of communication between scientists and society, public awareness of nanotechnology has become exaggerated and inaccurate. Ashley Shew brings up a good point in her paper "Codifying the Ethics of Nanotechnology" when she says there is a level of hypocrisy with nanotechnology in that it maintains a basic research level but insists on its capabilities to change the world.

Nanotechnology has great potential for success and great potential for failure. It could lead to a new era filled with innovative developments or an era filled with irreversible destruction. Scientists right now should keep in mind the long-term effects of their developments, even if it means going back to the old fashion list of 'good' and 'bad'—good, we can recycle and reuse waste products; bad, your neighbors could use microscopic devices to spy on you! There remains much ground for nanotechnology to explore–we are not yet in clear waters.

Figure 2. The yellow and green solutions are suspensions of silver nano-particles, and the rest are suspensions of gold nano-particles. The nano-metal suspensions are under development for biological sensing applications and for contol of harmful bacteria. Courtesy of Guo-Quan Lu.

The author would like to thank Dr. K. Eric Drexler, Nanorex Inc. for allowing us to use his mechanosynthetic reactions picture, Dr. Guo-Quan Lu, Virginia Tech for allowing us to use his gold nanoparticles picture, Ashley Shew, Virginia Tech for releasing her academic papers, which proved invaluable in this article's research process, and Navin Manjooran, Virginia Tech for supplying resourceful articles to help get the research ball rolling.

References

[1] Shew, Ashley. "The Big Nanotech Schism: How A Small Area of Study Split." STS 5205: History of Science, Virginia Polytechnic Institute and State University: December 6, 2005.

[2] Silva, Gabriel A. "Introduction to nanotechnology and its applications to medicine." Surg Neurol 2004; 61: 216-20.

[3] Shew, Ashley. "Codifying the Ethics of Nanotechnology." Presentation at IANANO's International Congress of Nanotechnology, San Francisco: November 1-3, 2005.

[4] Baum, Rudy. "Nanotechnology: Drexler and Smalley make the case for and against 'molecular assemblers.'" Chemical and Engineering News 81.48 (2003): 1 Dec. 2003 <http://pubs.acs.org/cen/coverstory/8148/8148counterpoint.html

[5] "A debate about assemblers on Physics, Fundamentals, and Nanorobotics: A rebuttal to Smalley's assertion that self-replicating mechanical nanorobots are simply not possible." Institute for Molecular Manufacturing, 2001. <http://www.imm.org/SciAmDebate2/smalley.html#FatFinger>

[6] Bruce, Donald. "The question of ethics." NanoToday. 1.1(2006): 6-7.

[7] Roco, M. C. "Broader Societal Issues of Nanotechnology." *Journal of Nanoparticle Research* 5: 181-189. Kluwer Academic Publishers: 2003.

[8] ActionBioscience. Andrew. Chen. March 2002. <http://www.actionbioscience.org/newfrontiers/chen.html>

Industry Insider: Micron Technology, Inc.

Jessica Pritchard, English

Micron Technology, Inc., founded by Ward Parkinson, Joe Parkinson, Dennis Wilson, and Doug Pitman in 1978, stands as one of the leading international providers of advanced semiconductor solutions, producing various semiconductor devices. Such devices include DRAM (dynamic random access memory) components, flash components, and CMOS (complementary metal oxide semiconductor) image sensors. With a strong focus on materials research, Micron continues to create next generation digital technology, pushing the boundaries of new imaging technology. In fact, Micron continues to hire recent graduates from around the country in materials related fields including chemical, electrical, computer, and materials engineering, as well as physics, and with their help, created one of the industry's first 1.7 micron-pixel image sensors.

In the late 1990s, Robert W. Hendricks, Professor of Electrical and Computer Engineering (ECE) at Virginia Tech, spearheaded a collaborative effort between the Departments of ECE, and Materials Science and Engineering (MSE), along with Micron of Manassas, VA. This effort led to the creation of the Center for Microelectronics, Optoelectronics, and Nanotechnology (MicrON) at Virginia Tech, of which Hendricks was the first Director. MicrON—not to be confused with Micron Technology, Inc.—is now comprised of laboratories, which focus on research in electronic materials, electronic and photonic devices, biotechnologies, and micro- and nano-electromechanical systems (MEMS and NEMS). This facility is used to enhance education in science and technology at Virginia Tech. In recent years, Dr. Hendricks has focused more on teaching, and on the creation of a microelectronics minor in the College of Engineering, along with the creation of the Micron Scholars Program. According to this program, juniors and seniors from the Departments of Chemical Engineering (ChE), ECE, and MSE receive substantial scholarships and are required to complete the microelectronics minor. The goal of this cooperation is to educate more students in microelectronics. Louis Guido, Associate Professor of MSE and ECE as well as the current Director of the MicrON laboratories, said, "The two things that attracted Micron to invest in Virginia Tech were the collection of faculty and the fact that we are trying to build this area." Growing dramatically since its beginnings, MicrON now includes 9 faculty members, 17 graduate students, and approximately 13 undergraduate students from the Departments of ECE, MSE, Mechanical Engineering, and Physics. The MicrON laboratories at Virginia Tech are comprised of 2,450 ft^2 housing advanced processing and characterization equipment for use by faculty and students. Some of the most sophisticated systems include a contact mask aligner for sub-1-μm lithography, an inductively coupled plasma etcher, a deep silicon reactive ion etcher, a plasma-enhanced chemical vapor deposition system, and a surface profilometer, as well as a well-equipped cleanroom facility. With these facilities at their disposal, students are able to manufacture and test a broad range of cutting edge materials and devices.


Micron Technology, Inc.'s Manassas, Virginia facility

Micron encourages co-ops, internships, and undergraduate research at several partner high schools and universities. As an example, many students work at the Manassas facility, gaining valuable experience in the microelectronics field. Dr. Guido said, "One of the reasons they [Micron] partnered with Virginia Tech is the good experience they've had with Tech students in the past. The feeling was that if they had more of a presence on campus, this would foster broader awareness and increase student interest. That's something that they're very interested in continuing—students doing internships in the summer, and even co-ops, because ultimately they want to hire these students." One such student is Ethan Lavery, a VT-MSE alumni and 2006 president of Materials Engineering Professional Societies (MEPS). When asked what a typical day at Micron entails, Ethan said, "I interpret data to find defect trends in silicon wafers so that I can diagnose the issue and recommend solutions to the affected areas of the fab. The data can come from SEM [scanning electron microscopy] and optical images, wafer maps, and SPC [statistical process control] charts." In terms of the overlap between the concepts and skills he learned at Virginia Tech and his current responsibilities, Ethan said, "Since I deal with defects, understanding the mechanics of why these defects occur is critical in diagnosing them. Often, these defects involve chemical properties of crystals and stress concentrations." Virginia Tech and Micron have established a strong bridge that serves as a model relationship between academia and industry.

MEPS @
VIRGINIA TECH

The Materials Engineering Professional Societies (MEPS) is both an academic and social organization that is run by the MSE student body. MEPS members represent the MSE department at professional conferences events. Additionally, MEPS helps recruit interest in MSE through the VT junior and senior open houses and the VT STARS program, which focuses on introducing high school students to MSE. The organization also hosts guest speakers and will sponsor various field trips throughout the year. Socially, MEPS participates in numerous activities, such as intramural softball, bowling tournaments, and football tailgates for the College of Engineering.


Tailgates


Professional Development


Intramurals

Outreach

Virginia Tech Department of Engineering Science and Mechanics

The department has a distinguished history. A recent review by a blue-ribbon panel concluded that ESM has a "longstanding record of excellence as a key element of the College of Engineering with national visibility". The department has twenty-five faculty members who support roughly 80 doctoral students and have research expenditures of above $6M. The department provides a strong foundation and a sturdy framework for the discovery, development, transfer, and implementation of new knowledge in the areas of mechanics of materials and material systems, fluid mechanics, dynamics and vibration, biomechanics, and computational methods. It is fully committed to providing an environment for strong undergraduate and graduate education that emphasizes fundamental understanding rather than specialization, high-quality teaching, innovation, frontier-level research, and service to the professional mechanics community. It strongly encourages undergraduate research and offer many summer undergraduate research opportunities. The ESM program is well suited to address the critical need for interdisciplinary and multidisciplinary education and research. For instance, we have faculty members who have backgrounds in engineering mechanics (the principles on which most areas of mechanical, aerospace, ocean, civil, materials, and perhaps even chemical and mining, engineering are based on) and engineering science (applied mathematicians and physicists). Some also have interests in aspects of electrical and computer engineering, computer science, and the life sciences. Engineering science is a nomenclature that characterizes a program like ours which focuses on imparting and using fundamental interdisciplinary skills that address engineering problems. They have collected superb scientists (physicists, chemists and the like), applied mathematicians, and engineers with various backgrounds (mechanical, electrical, chemical, etc.) who lead the ESM educational and research programs. The National Academy of Engineering has issued a document that states that the nation will need exactly these kinds of engineers in 2020.

North Carolina State University Department of Nuclear Engineering

The Department of Nuclear Engineering at North Carolina State University is among the strongest nuclear engineering departments in the U.S. It is the first nuclear engineering department and the first non-government 1MW research reactor facility in the U.S. The department is ABET accredited and provides undergraduate and graduate education. The undergraduate enrollment is 142 and the graduate program has 51 graduate students (MS and PhD) in the fall of 2006.

The department's faculty obtains sponsored research support from various funding institutions (DOE, DOD, NSF, NIH and industry). The department ranks second in Department of Energy (DOE) Nuclear Engineering Education Research (NEER) awards, and is the lead institution in the DOE INIE consortium for the southeast. The department has two research centers, CEAR, the Center for Engineering Applications of Radioisotopes and EPRC, the Electric Power Research Center. The main areas of research are radiation transport, computational reactor thermal-hydraulics and two-phase flow, computational reactor physics, nuclear fuel cycle optimization, nuclear materials, plasma engineering and fusion reactors and radiological engineering. The outreach program conducts two major events each year, a science teachers' workshop on nuclear science applications, and a young investigators summer program in nuclear technology. The US Department of Energy, industry, and the American Nuclear Society support these two programs. Nuclear engineering at NC State University is one of the lead programs with the US Department of Energy on the 'Harnessed Atom Program', and the lead on nuclear engineering marketing plan program.

Research facilities include the 1MW PULSTAR research reactor, neutron radiography, neutron activation analysis laboratory, prompt gamma analysis system, heat transfer and fluid flow laboratory, nuclear materials laboratories, plasma and fusion, and radioisotope applications laboratories.

The undergraduate research program offers students opportunities to work with faculty on research. The program supports undergraduate research in the summer and during the academic year. Undergraduate students participate in the annual NC State University Research Symposium, the State of North Carolina Research Symposium and many other undergraduate symposia. Undergraduate students also participate in professional conferences and present their work in poster sessions. Many students are winners of best presentation, best poster and best articles; they are recognized and awarded by the Scientific Research Society Sigma Xi and the American Nuclear Society.

Michigan Technological University Department of Materials Science and Engineering

In July of 2000, the department changed its name to Materials Science and Engineering (MSE). The name change was made to better reflect the breadth of instructional and research activities in which its students and faculty are engaged. The new name is also consistent with its sister departments at other institutions, including many that also started out as "Metallurgy" or "Minerals" departments.

The MSE undergraduate program at Michigan Tech has grown to the point where it is one of the largest undergraduate programs of its kind in the nation. The present scopes of both instructional and research programs include broad multidisciplinary approaches to refining, processing, development, application, and recycling of engineering and engineered materials. Great pride is taken in its graduates, many of whom have achieved national recognition in our profession and as businesspersons, researchers, and administrators.

The semester-based curriculum provides a solid foundation in science, mathematics, and fundamentals of materials science and engineering. The senior year centers on two activities: the year-long Senior Design experience, and 10 hours of electives. These electives are very flexible, so that students may tailor their senior year to their individual career goals. Approved courses can be taken within our Department, or in any other department of science, engineering, or mathematics.

The Senior Design projects are a crucial part of the curriculum. Students work in teams, on real projects which are submitted by our industrial partners. The industrial partner works with the team during the year. Problems are open-ended, and are very similar to problems that graduates will be solving in industry. In addition to the traditional year-long projects, students can also satisfy this requirement through the unique Enterprise Program found only at Michigan Tech. In this program students participate in developing and operating their own business over a three year period, thereby applying their technical expertise and developing important business skills at the same time.

The Department supports between 20-30 graduate students each year, mostly on Research Assistantships associated with externally-funded research programs. Funding levels have been between $1 – 1.5 million per year over the last 10 years.

Indian Institute of Technology, Kanpur, Department of Materials and Metallurgical Engineering

The Department of Metallurgical Engineering at The Indian Institute of Technology (IIT) was setup in 1960 and was later renamed Materials and Metallurgical Engineering Department in 1993. The field of study here includes the entire spectrum of materials science, starting from extraction, processing, characterization and modeling of materials and processes. This department has pioneered a unified approach in teaching and research to develop state-of-the art materials and processes for specialized applications. It is presently the leading department in the country in developing a unique approach to materials education and research. The department offers bachelors, masters and Ph.D programs.

Virginia Tech Department of Chemistry

Chemistry has been part of the curriculum at Virginia Tech since its establishment in 1872. Initially, there were two faculty members who taught chemistry (along with other classes). The first chemistry Bachelor's degree was conferred in 1892 and the first Doctorate in 1942. Today, there are 28 faculty members, 135 graduate students, 15 postdoctoral associates, and 250 undergraduate majors. The faculty has been recognized with six NSF CAREER awards, three Cottrell Scholarships, one Dreyfus New Faculty award, election of one to the National Academy of Engineering, and three Virginia Scientist of the Year awards. Today, research activity is supported by over $8 million in annual external grant funding.

Experimental Simulation of High Energy-Density Plasma Interaction with Liquid Metal Media for Inertial Fusion Reactor First Wall Studies

Elijah Martin

North Carolina State University, Department of Nuclear Engineering
Burlington Engineering Laboratory, Raleigh, NC 27695

Abstract

Inertial confinement fusion (ICF) is a promising technology positioned to address the future energy needs of the world. An advanced design concept for ICF reactors is to use a circulating liquid barrier to protect the first wall of the target chamber. With the impaction of the high energy-density plasma on the liquid barrier, sputtering and vaporization can occur causing particulate matter to enter the target chamber interior volume. In order to best engineer the design of the target chamber, this interaction must be well characterized. A small-size experimental facility was designed, constructed, and operated at NC State University to simulate the interaction of high energy-density plasma with liquid metals. This study focuses on characterization of the plasma-liquid metal plume. Characterization of the generated plumes shape and size of evolved vaporized liquid metal particulates; density and other plasma parameters were studied in this research. Electrical and spectral data were obtained for each experiment to obtain the plasma parameters including total power, impedance, electron temperature and density and identification of species. It was determined that a typical plasma generated from a 2 kV discharge has a temperature of 1.0 ± 0.3 eV and a density of $4.2 \pm 1.7 \times 10^{17}$ cm^{-3}. The height and geometric configurations of the collection substrates were changed to produce a model of the generated metallic plume. Data analysis of the substrates indicates that the plume has a higher density profile and smaller particulates at distances closer to the point of impact, and the particulate size increases and the particulate density profile decreases with increased distance from liquid metal pool.

Keywords: Inertial confinement fusion, pulsed power, time integrated optical emission spectroscopy

1. Introduction

Plasma interaction with first wall and interior reactor chamber components is an influencing factor in the design of Inertial Confinement Fusion (ICF) facilities. An economical ICF reactor must include a first wall protection scheme, due to the fact that ablation of the interior chamber walls will occur, due to the interactions between the high energy density plasma with interior components. This interaction is severe enough that the frequency and cost of replacing components would outweigh the value of power produced. The concept of a liquid metal wall, in which a circulating lithium curtain would be used, has been considered in many studies. The interaction of plasmas with moving liquid metals is a complex subject due to the influence of hydrodynamics, evaporation and droplet formation, and nucleation and agglomeration of condensed particulates. Due to this complexity, a detailed understanding of this interaction must be known before the liquid first wall protection scheme can be successfully implemented.

The concept of a liquid metal first wall for ICF facilities has been proposed and studied, including the possibility of using a moving liquid metal curtain in the National Ignition Facility (NIF).[1] Although a drywall is highly considered for laser-driven ICF facilities, wetted wall and thick liquid wall are considered more favorable for light and heavy ion drivers.[2,3]

Under the condition of plasma impact on the liquid metal wall, it is expected that high energy-density plasma will sputter the liquid metal, resulting in strong evaporation of particulate matter followed by condensation. In order to better understand the problems associated with liquid metal walls, an experiment was designed, constructed, and operated using an arc-generated plasma source positioned above a liquid metal pool. The experimental simulation of plasma-liquid interaction will be scaled using multiple parameters for comparison to actual ICF reactors, such as NIF. Arc-generated plasmas are adequately sufficient to simulate fast pulse modes of high energy-density plasma generation. Studies on devices generating similar plasmas have shown to have electron temperatures on the order of 1–2 eV and electron densities of 10^{16}-10^{17} cm^{-3}.[4,5] Due to the magnitude of the plasma density, local thermodynamic equilibrium assumptions can be made for highly excited states. Thus, the relative line method and stark broadening mechanisms can be utilized in spectral analysis.[6-8]

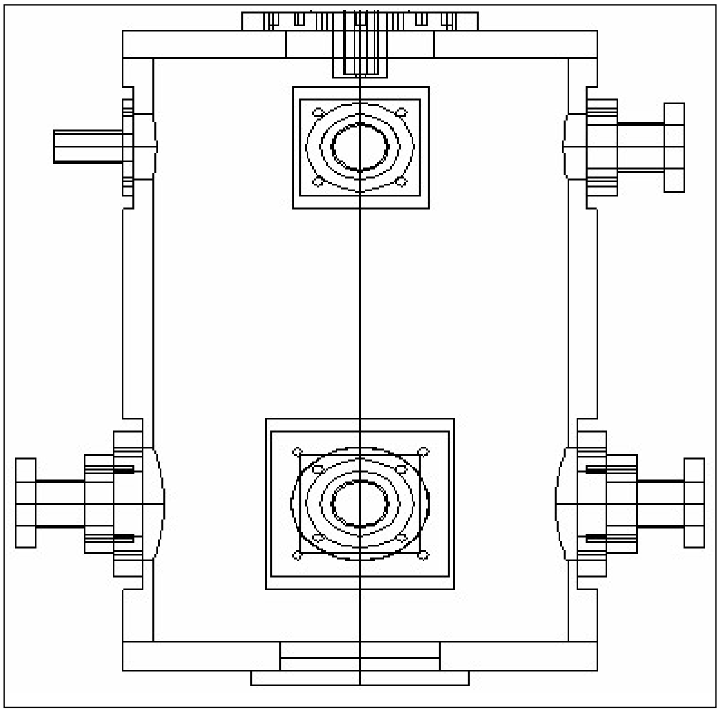

Figure 1. AGEIS chamber

2. Procedure

The experiment was contained in the AGEIS chamber (Arc Generated Explosion Impact on Substrate). The vacuum chamber, shown in Figure 1, is a steel cylinder of diameter 30.5 cm and a height of 60 cm with six radial ports and one axial port which was used for diagnostics, vacuum pumping and electrode feed-through. The chamber was accessed by a flange located at the top of the chamber.

The other ports were used for fiber optic feed-through, vacuum pumping and measurements, and power and electrode feed through. Two cylindrical electrodes with a diameter of 0.6 cm and a length of 25.5 cm were used. A 330 μF, high energy-density capacitor was connected to the cylindrical electrode located at the lower right port and the cylindrical electrode located at the lower left power was connected to ground.

When conducting an experiment, referred to as a "shot", the following steps were taken. Five polished aluminum substrates were cleaned and attached to the exoskeleton. Then a copper fuse 10 cm in length and 0.5 mm in diameter was attached to clamps which were in turn attached to the ends of the electrodes in a fashion indicated by Figure 2. Then the exoskeleton was positioned inside of the vacuum chamber. 150 ± 10 grams of lead were heated to a temperature of 350 ºC and visual confirmation of a phase transition to the liquid state was made. To better simulate the conditions of an inertial confinement fusion reactor, the vacuum chamber was pumped down to 20 ± 2 torr. Finally, the high energy-density capacitor was charged to a potential of 2 kV and the shot was taken. As the high energy-density plasma is generated between the cathode and anode which are attached to the lexan flanges located at the lower left and right ports respectively, the plasma expanded radially and impacted the liquid pool of metal.

An exoskeleton was constructed to fit inside the reaction chamber, this exoskeleton houses the lead reservoir which was moveable allowing the distance between the plasma source and liquid pool of metal to be varied. A heating element placed under the lead reservoir held the temperature at 350 ºC during the experiment. The temperature of the lead reservoir was measured using a thermocouple located between the heating

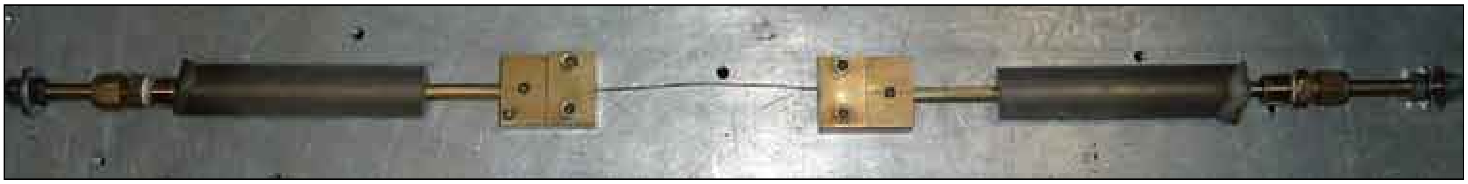

Figure 4. Geometry of electrodes inside the vacuum chamber, shown with copper fuse

element and the steel dish containing the lead reservoir. To collect the plume of metal particulates generated from the plasma impact, five polished aluminum collection substrates 2 cm in diameter were positioned above the plasma source as shown by Figures 3 and 4. The collection substrates were connected to the exoskeleton in such a way that the distance from the lead reservoir could be varied.

The collection substrates were positioned with a geometry to allow for a mirror plane of reflection located at the vertical center plane of the discharge. The discharge current was acquired by a 1:1000 Pearson coil; the discharge voltage was acquired by a 1:1000 Tektronix Capacitively-coupled HV probe. A Tektronix TDS 2024/200 MHz four-channel digital storage oscilloscope was used for data acquisition and storage. An Ocean Optics HR2000 spectrometer was used to obtain emission spectrum from the discharge. The grating of the spectrometer has 600 lines/mm and was blazed at 500 nm, the spectrometer has a resolution of 0.4 nm and a bandwidth ranging from 300 to 730 nm. The emission spectrum of the discharge was obtained using a 100 µm fiber optic, positioned such that a radial view of the expanding plasma was obtained. The 100 µm fiber optic was connected outside the vacuum chamber to a bifurcated 400 µm insulated patch cord that interfaced with the spectrometer and a monochromator attached to a Photomultiplier Tube (PMT).

Figure 3. Geometry of the collection substrates attached to the exoskeleton

Figure 4. Exoskeleton inside of the vacuum chamber

3. Results and Discussion

3.1 Electrical Waveforms

To determine the power dissipated within the high energy-density plasma and the impedance of the plasma, current and voltage waveforms were obtained. Figure 5 depicts typical discharge current and voltage waveforms.

The impedance of the discharge was calculated from Ohms Law. Figure 6 shows the plasma impedance as a function of time for a typical discharge.

Figure 5 shows that the equivalent circuit of the device was underdamped. It was assumed that the plasma had recombined when the voltage dropped to zero, roughly at time t=40 µsec, as shown by Figure 5. Confirmation of this assumption was made from energy conservation and the PMT waveform shown in Figure 7. The net input energy into the discharge was calculated from the difference between the initial and residual energy on the capacitor after the shot. The net input energy was also calculated by integrating the power dissipated within the plasma, shown in Figure 8, over the time length 0 to 40 µsec. From a comparison of both methods used to calculate the net input energy, it was confirmed that discharge was identified by when the voltage dropped to zero.

The net input energy into the plasma was averaged over all shots. On an average, the net input energy was 660 ± 0.6 J. The discharge conditions were constant so that all shots maintained the same net energy input to the system.

To determine when initial breakdown of the discharge occurred, the waveform generated by the PMT was analyzed. It was assumed that initial breakdown occurred when photon emission occurred. A monochromator was used to collect photons resulting from a neutral copper atom electronic transition at 521.8 nm.

Figure 7 shows that breakdown occurred after the initial voltage spike; Figure 7 also indicates that photon emission has terminated when the voltage drops to zero confirming the plasma recombination assumption. It was determined that pickup from the electromagnetic field generated from the shot was distorting the waveform of the PMT. Due to the above fact, an isolation transformer was used to supply AC voltage to all electrical equipment.

3.2 Time Integrated Optical Emission Spectroscopy

To determine the electron temperature of the discharge, the relative line method was utilized.[6-8] It can be shown by equilibrium quantum statistics and thermodynamics that the local thermodynamic equilibrium (LTE) distribution over the state of an atom obeys the following.[6]

$$\frac{N_m}{N} = \frac{g_m}{Z_a(T)} e^{-\frac{E_m}{kT}} \qquad (1)$$

Where N_m is the population of state m, N represents the number of same species atoms, g_m is the statistical weight of the upper level energy state m, $Z_a(T)$ represents the partition function, E_m is the upper level energy of state m, and kT is the electron temperature. The ratio of two bound states, m_1 and m_2, can be determined from Equation 1.

$$\frac{N_{m_1}}{N_{m_2}} = \frac{g_{m_1}}{g_{m_2}} e^{-\left[\frac{E_{m_1}-E_{m_2}}{kT}\right]} \qquad (2)$$

The integrated emission line intensity, i_{nm}, can be found by integrating the intensity of a transition, I_{nm}, with respect to the angular frequency, ω, along the line of sight in the plasma, L.

$$i_{nm} = \int I_{nm}(\mathrm{w})d\mathrm{w} \qquad (3)$$

The assumption was made that the plasma is homogenous along the line of sight.

$$i_{nm} = \frac{\mathrm{hw}_{nm}}{4\mathrm{p}} A_{nm} N_m L \qquad (4)$$

The angular frequency associated with the transition m → n is represented by ω_{nm}, the transition probability for the transition m → n is represented by A_{nm}, and h represents Planck's constant. A ratio of the integrated emission line intensity, R,

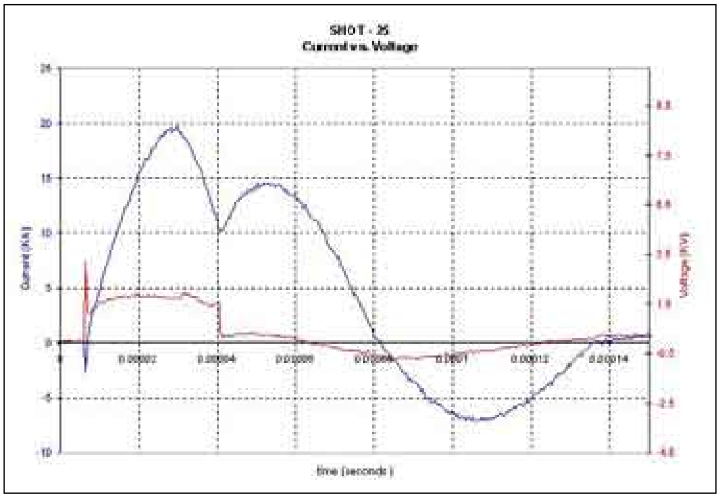

Figure 5. Current and voltage trace of a typical discharge

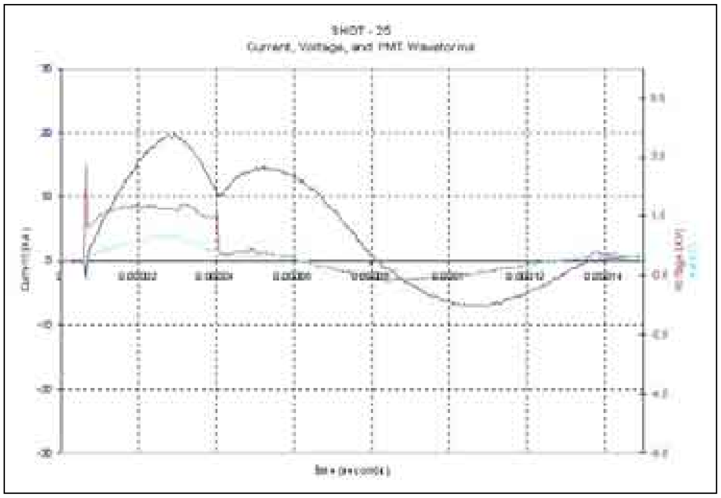

Figure 7. PMT waveform

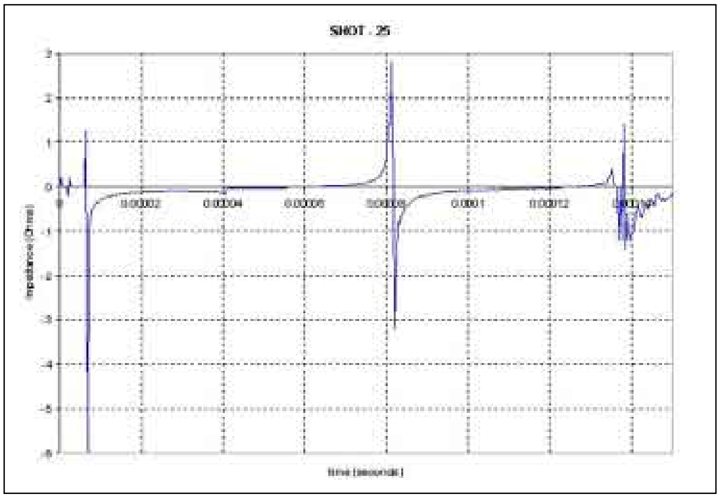

Figure 6. Transient plasma impedance

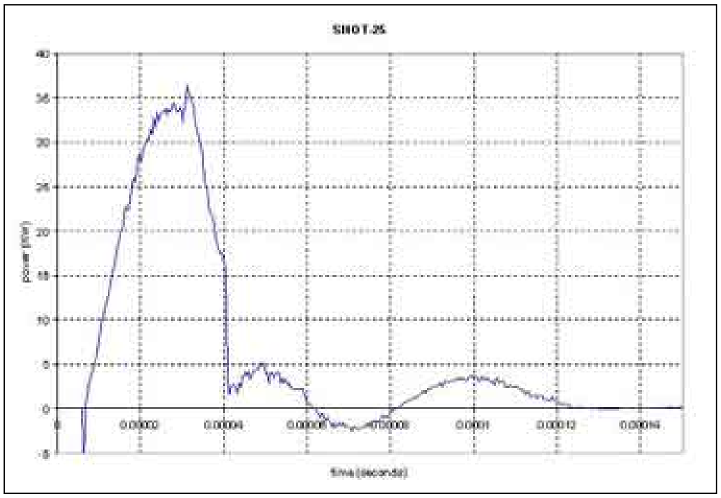

Figure 8. Transient power dissipated into the plasma

given by Equation 5 is taken for transitions $m_1 \rightarrow n_1$ and $m_2 \rightarrow n_2$.

$$R = \frac{i_{n_1 m_1}}{i_{n_2 m_2}} = \frac{\mathrm{w}_{n_1 m_1} A_{n_1 m_1} N_{m_1}}{\mathrm{w}_{n_2 m_2} A_{n_2 m_2} N_{m_2}} \tag{5}$$

Equation 2 is substituted into equation 5 to giving the following.

$$R = \frac{\mathrm{w}_{n_1 m_1} A_{n_1 m_1} g_{m_1}}{\mathrm{w}_{n_2 m_2} A_{n_2 m_2} g_{m_2}} e^{\left[\frac{E_{m_1} - E_{m2}}{KT}\right]} \tag{6}$$

The electron temperature, kT, of Equation 6 can be explicitly solved for giving the following expression.

$$kT = \frac{E_{m_2} - E_{m_1}}{\mathrm{h}\left[\frac{\mathrm{w}_{m_2 n_2} g_{m_2} A_{n_2 m_2}}{\mathrm{w}_{m_1 n_1} g_{m_1} A_{n_1 m_1}} R\right]} \tag{7}$$

Equation 7 states that given the ratio of integrated emission line intensity of two bound transitions taking place within the same species atom, the free electron temperature can be determined.

$$l\,n\left[\frac{i_{nm}}{\mathrm{w}_{mn} A_{nm} g_m}\right] = -E_m \frac{1}{kT} + l\,n\left[\frac{N L \mathrm{h}}{Z_a(T)}\right] \tag{8}$$

For LTE transitions of the same species atom the second term on the right hand side of Equation 8 is constant, the first term on the right hand side of Equation 8 is know as the Boltzmann function. The electron temperature can be determined from a plot of the Boltzmann function vs. upper level energy of the transition. Equation 8 was used to determine the electron temperature for the arc-generated plasmas of the AGEIS device. Due to the fact that the use of Equation 8 requires LTE of the excited states used, the LTE state of the discharge must be confirmed. Highly excited states of similar discharges generated by Dale *et al.* and Sharpe *et al.*[4,5] have found to meet the LTE condition. To confirm the LTE assumption, a limit on the principal quantum number of a transition in LTE is given by Fujimoto.[7]

$$p \geq \frac{118}{\Theta^{0.43}} + \frac{2.2 \cdot 10^3}{\mathrm{h}^{0.15}} \tag{9}$$

$$\Theta = \frac{T_e}{z^2} \tag{10}$$

$$\mathrm{h} = \frac{n_e}{z^7} \tag{11}$$

The electron temperature in Kelvin is represented by T_e, the electron density in m^{-3} is represented by n_e, and z represents the atomic number of the plasma species. Sharpe and Merrill *et al.*[5] reported electron temperatures of 1 to 2 eV and electron densities on the order of 10^{17} cm^{-3} obtained in similar arc-generated discharges. Assuming the plasma parameters will be similar in AGEIS, the lower limit on the principal quantum number, found using Equation 9, was in the range of 50 to 60. Numerical calculations given by Fujimoto have shown that for the given discharge conditions Equation 9 will over predict the lower limit of the principal quantum number by about one half. The lower limit on the principal quantum number for LTE transitions will be assumed to be 25 to 30. It should be noted that Equation 9 is for hydrogen like ions. The calculation conducted here is an approximation. LTE confirmation will be concluded from the linearity of the Boltzmann plot given by Equation 8. Figure 9 depicts a spectrum obtained from a typical discharge.

The following first order neutral copper lines, given in Table 1, were identified in the spectra obtained from typical discharges of AGEIS, the lines are shown with the various constants associated with the transition.[9]

To determine the line integrated emission intensity necessary for use of Equation 8, Peakfit v4.12 was used to provide a numerical integration and other parameters such as the Full Width at Half Maximum (FWHM) of the spectral lines. Figure 10 represents a fitted emission spectrum obtained from a typical discharge of AGEIS.

It was found that the profile of the spectral lines obtained from copper discharges in AGEIS have a Lorentzien profile. Equation 8 was plotted using the identified lines and constants given in Table 1. The electron temperature was determined from the slope of Figure 11.

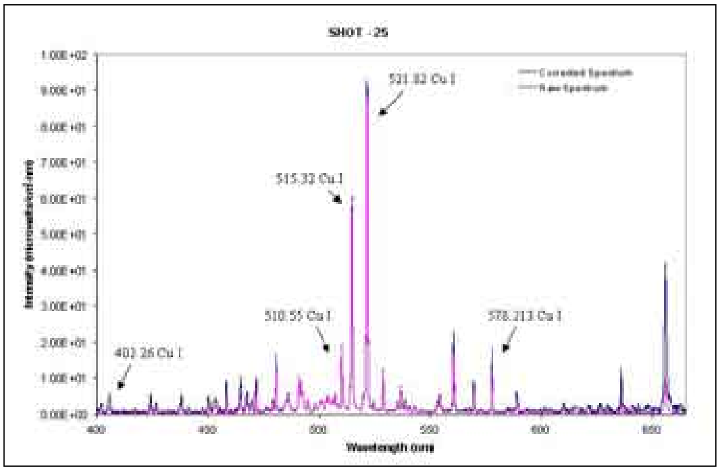

Figure 9. Emission spectra of copper discharge in AGEIS

The linearity of the Boltzmann plot shown in Figure 11 indicates that the transitions associated with the identity lines are in LTE. The electron density, in units of m^{-3}, of the discharge is determined from pressure broadening, also known as Stark broadening, of the neutral copper spectral lines identified above by the following expression.

$$n_e = \frac{FWHM}{\omega_m} \cdot 10^{23} \tag{12}$$

The Stark width, ω_m, is a function of electron density and a weak function of electron temperature; Stark width values are obtained for an electron temperature of 10000 K and electron density of 10^{23} m^{-3}. Table 2 gives Stark width values for the identified lines.

The electron temperature and density were determined by the above methods for all discharges, Table 3 gives the calculated values for each discharge.

3.3 Collection Substrates

Digital pictures of the surface of the collection substrates were taken prior and post shot for all substrates, using an Olympus BH2-UMA optical microscope at 100x magnification. The digital pictures were analyzed using ImageJ, a NIH program.[10] ImageJ produces information (in pixel units) on the particle count, average particle size, total area, and area fraction for the digital images. For each substrate 5 pictures were taken at different locations to obtain better averaging. The collection substrates are labeled 1 through 5 in the Tables 4 and 5, where substrate 3 is positioned over the center of the lead reservoir.

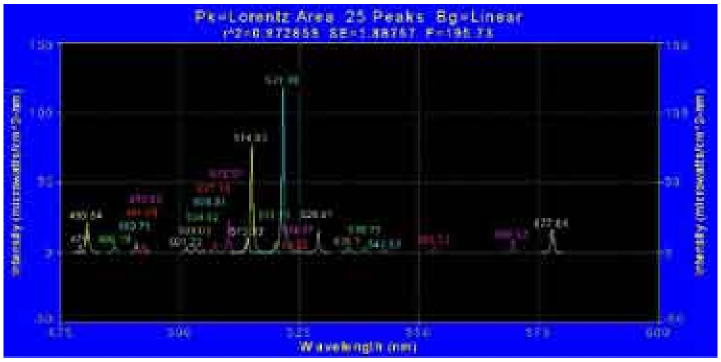

Figure 10. Fitted spectra

Figure 12 shows an original digital image, which is gray scaled and masked by ImageJ.

Due to the fact that the image is gray scaled for analysis by ImageJ, no differentiation between copper and lead particles or the lines occurring on the aluminum surface from the milling process could be determined. To account for this, background images were obtained for aluminum substrates alone and for a case when the lead pool was not present. The size of the aluminum only particles was largely due to the fact that the lines on the surface were not broken by any particulates and therefore appeared as large particles. Although this is not very accurate, it gives an estimate of the background counts and size. For the copper background, more data needs to be taken to accurately define the distribution for a copper only shot.

Preliminary data analysis conducted using ImageJ generally indicates the following trend: the lead particulate plume has a higher density profile and smaller particulates at distances closer to the point of impact with lead reservoir, and the particulate size increases and the particulate density profile decreases with increased distance from the lead reservoir. The particulate size is generally larger on substrates 1 and 5; the particulate density is generally larger on substrates 2 and 4. The particulate density can be correlated to the particulate size from the effect that masking plays in the low-density regions with the larger particle size. This masking effect occurs due to the fact that larger particulates will decrease the area for the smaller particulates to be observed or obscure the viewing of the smaller particulates that are under or on the larger particulates. More data is needed

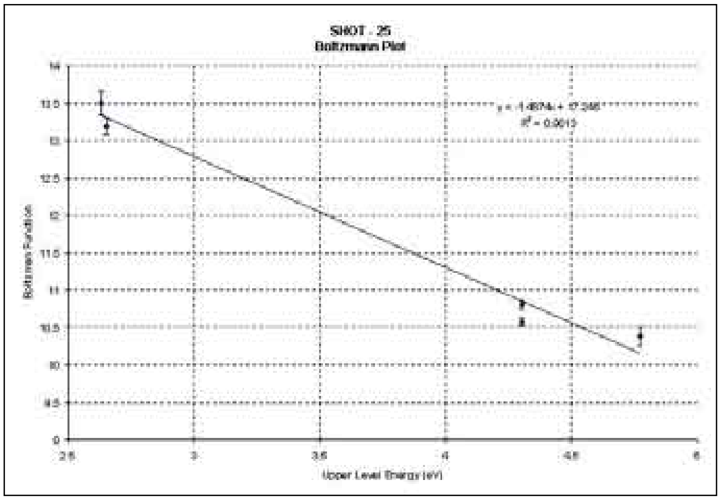

Figure 11. Boltzmann plot of identified lines

Wavelength (nm)	A_{nm} - Transition Probability (10^{-8} s^{-1})	g_m - Statistical Weight	E_m - Upper Level Energy (eV)
402.263	1.90E-01	4	4.773
510.554	2.00E-02	4	2.653
515.324	6.00E-01	4	4.303
521.82	7.50E-01	6	4.304
578.213	1.65E-02	2	2.631

Table 1. First order neutral copper lines present in emission spectra

for a full statistical analysis on the collected plume particulates but from preliminary data analysis, trends are observed in the plume.

4. Conclusions

An experiment designed to generate an arc-driven plasma which will interact with a liquid metal pool has been constructed and tested for operation. It was determined by time integrated optical emission spectroscopy that the discharge average electron density is 4.2 ± 1.7 x 10^{17} cm^{-3} and the average electron temperature is 1.0 ± 0.3 eV. All discharges were established with a net input energy of 660 ± 0.6 Joules. Analysis of collection substrates using ImageJ indicates that the interaction of the high energy-density plasma with the liquid lead reservoir leads to the generation of a lead particulate plume. Nucleation and condensation mechanisms were found to dominate in the plume as the distance from the point of impact is increased; this conclusion is supported by the following trend: the particulate size increases and particulate density decreases as the distance between the collection substrate and the lead reservoir increases. Preliminary data shows that the condensate has a high particulate density core with smaller particulate matter; as the distance from the core is increased, the particulate density decreases, and the particulate size increases. The above conclusions indicate that nucleation and condensation takes place close to the point of impact, 6-7 cm, thus hindering small particulate matter from entering the interior volume of the ICF reactor chamber. Particulate density was shown to decrease as the distance from the point of impact is increased. This effect will lower the coupling between the mechanisms (laser/ion beams) used to drive the fusion reactions, and the plume generated from the interaction of the high energy-density plasma and the liquid first wall.

Wavelength (nm)	ω_d - Stark Width (nm)
402.263	0.431
510.554	4.30E-02
515.324	0.19
521.82	0.22
578.213	7.20E-02

Table 2. Stark width values for various neutral copper lines

Experiment	Temperatue (eV)	Density (cm^{-3})	Net Energy Input (J)
SHOT-1	0.939	1.14E+18	659.9
SHOT-6	1.17	2.8E+17	659.7
SHOT-7	1.15	4.87E+17	659.2
SHOT-8	0.819	2.37E+17	666.4
SHOT-9	0.947	2.76E+17	666
SHOT-10	0.639	1.66E+17	659.6
SHOT-11	1.29	3.2E+17	666.4
SHOT-12	0.701	3.03E+17	659.9
SHOT-14	0.985	3.43E+17	659.9
SHOT-15	0.943	2.51E+17	659.9
SHOT-16	0.661	3.11E+17	660
SHOT-17	0.69	2.16E+17	659.9
SHOT-18	0.663	2.08E+17	659.9
SHOT-36	0.817	5.72E+17	659.6
SHOT-38	0.948	2.83E+17	659.7

Table 3. Electron density and temperature values

Acknowledgements

The author greatly thanks Dr. Mohamed A. Bourham of the Nuclear Engineering Department of North Carolina State University for his countless hours of mentoring and numerous discussions, without his guidance this project would not have been possible. This research was conducted at North Carolina State University to aid the development of an economical power producing inertial confinement fusion reactor.

Collection Substrate	1	2	3	4	5
SHOT-12	4.607	3.392	7.149	2.245	8.189
SHOT-14	4.275	1.783	3.404	3.673	4.669
SHOT-15	4.196	0.759	1.745	2.716	3.042
SHOT-19	1.088	0.588	0.647	0.851	1.015
SHOT-16	9.207	6.948	6.514	3.243	7.892
SHOT-17	5.504	4.408	8.787	10.06	13.08
SHOT-18	2.743	2.25	1.222	6.167	4.909

Table 5. Average particulate size in 1x10^{-2} mm^2

Collection Substrate	1	2	3	4	5
SHOT-12	30.33	32.79	25.21	37.79	17.26
SHOT-14	25.35	92.66	49.5	65.03	45.02
SHOT-15	59	164	88.51	101.8	65.31
SHOT-19	197.3	238.7	84.13	178.7	93.55
SHOT-16	33.38	18.98	18.43	33.02	17.4
SHOT-17	19.43	24.07	14.74	13.12	12.7
SHOT-18	19.86	51.79	58.28	14.09	33.65

Table 6. Particulate surface density in mm^{-2}

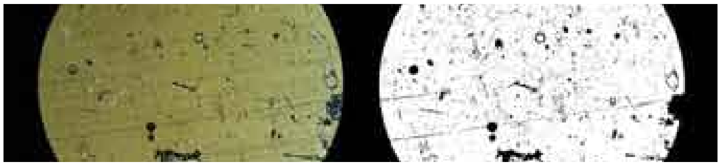

Figure 15. Original (left) and analyzed (rght) picture

References

[1] Moses, E.I. The National Ignition Facility: Status and Plans for the Experimental Program. *Fusion Science and Technology* **2003**, *44*, 11-18.

[2] Meier, W. R.; Raffray, A. R.; Abdel-Khalik, S. I.; Kulcinski, G. L.; Latowski, J. F.; Najmabadi, F.; Olson, C. L.; Peterson, P. F.; Ying, A.; Yoda, M. IFE Chamber Technology - Status and Future Challenges. *Fusion Science and Technology* **2003**, *44*, 27-33.

[3] Moir, R.W.; Bieri, R.L.; Chen, X.M.; Dolan, T.J.; Hoffman, M.A.; House, P.A.; Leber, R.L.; Lee, J.D.; Lee, Y.T.; Liu, J.C.; Longhurst, G.R.; Meier, W.R.; Peterson, P.F.; Petzoldt, R.W.; Schrock, V.E.; Tobin, M.T.; Williams, W.H. HYLIFE-II: A Molten-Salt Inertial Fusion Energy Power Plant Design – Final Report. *Fusion Technology* **1994**, *25*, 5-25

[4] Dale, G.E.; Bourham, M.A. Experimental Investigation into Melt-Layer Erosion of Plasma-Facing Materials. *Fusion Technology* **1998**, *34*, 901-907.

[5] Sharpe, J.P.; Merrill, B.J.; Petti, D.A.; Bourham, M.A.; Gilligan, J.G. Modeling of Particulate Production in the SIRENS Plasma Disruption Simulator. *Journal of Nuclear Materials* **2001**, *290*, 1128-1133.

[6] Griem, H. R. *Principles of Plasma Spectroscopy*; Cambridge University Press: Cambridge, 1997.

[7] Fujimoto, T. *Plasma Spectroscopy*; Oxford University Press: Oxford, 2004.

[8] Hutchinson, I. H. *Principles of Plasma Diagnostics*; Cambridge University Press: Cambridge, 2002.

[9] *CRC Handbook of Chemistry and Physics*. CRC Press, Boca Raton, FL, 76th edition, 1996.

[10] Image processing software package free downloads from NIH, http://rsb.info.nih.gov/ij/index.html.

About the Author

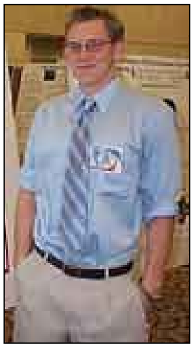

Elijah Martin

Elijah Martin is a fourth year student at North Carolina State University majoring in Physics, Nuclear Engineering, and Chemistry. He has been involved with various research projects involving plasma physics since his freshman year. His primary research interest included optical emission spectroscopy diagnostic techniques, electrical probe techniques, and magnetic confinement fusion.

Computer Simulation of a Hardness Indent Test into Nickel Nano Thin Films

Edward Parker and Peter Gaudreau

Virginia Polytechnic Institute and State University, Department of Materials Science and Engineering
Blacksburg, VA 24060

Abstract

Current experiments suggest that mechanical properties of thin films are different at thicknesses less than 100 nm. In this study, embedded atom method computer simulations are used to examine the differences in strengthening mechanisms at the nano scale. The simulation shows the mechanisms responsible for the differences in hardness with varying sample thicknesses from 12.8, 8, 6, and 4 nm. The simulation results show that as film thickness decreases the hardness of the film increases. Simulations were performed in single crystal films as well as model tricristals in order to study the effects of the grain boundaries. Tricrystalline films emitted dislocations at a lower pressure than single crystals.

Keywords: Embedded atom method, molecular dynamics, indentation, hardness, nickel, nano, thin film, visualization

1. Introduction: Behavior of Thin Films at Nano Scale

Thin films are used in several applications, including light emitting diodes (LED's), solar panels, and computer circuitry. Mechanical properties of thin films, such as hardness, are of concern when considering real world applications because mechanical properties of thin films are affected by point defects, dislocations, and grain size.[1] For example, the Hall Petch effect relates material strengthening with decreasing grain size. At the macro scale the strength of the material increases as the diameter of the grains decrease. However, this relationship between grain size and strength is lost when the grain diameter approaches the nano scale, grain sizes less than 20 nm.[2]

To completely understand nano scale behavior computer simulations are used to model atomic motions that occur during many different kinds of mechanical deformation in metals, including tensile tests and compressive loading scenarios.[3] At this point, however, there have been no attempts to model a hardness indentation on tricrystalline nickel nano thin films with varying film thickness. A tricrystalline film describes a polycrystalline film that has three grains with similar structure within the sample. The benefit of simulating the indentation is the visualization of atomic motions and dislocations as a function of time. The simulation also provides information on the mechanisms responsible for the differences between hardness data of nano scale versus macro scale film thicknesses. In this work we address 1) the response of single crystals films of varying thicknesses and 2) the effect of low angle boundaries present in the indented films.

2. Theory: Embedded Atom Method

The embedded atom method is currently a common technique used in computer simulation of metal systems.[4-7] The method provides a description of the interatomic forces in the system. It calculates the interatomic potentials in metals and models forces between atoms as follows:

$$E = \frac{1}{2}\sum_{i,j} V(r_{ij}) + \sum_{i} F(\rho_i) \qquad (1)$$

where E is the total energy of the system, $V(r_{ij})$ represents the energy between an atom and its nearest neighboring atom, and $F(\rho_i)$ represents an embedding function responsible for free electrons in the metal.[5–7] The nickel system is a face centered cubic (FCC) lattice.[1] The potentials reproduce the perfect lattice properties and were developed by Y. Mishin et al.[8]

3. Procedure

3.1 Computer Simulation Techniques

Simulating mechanical deformation in real time requires a vast number of calculations; therefore, powerful computer software is required for the simulation of a hardness test. A program called Lammps is currently being used for simulating materials using the embedded atom method.[3] These simulations can show applied forces to the lattice and the subsequent atomic motions from the deformation. Lammps is capable of mapping the Cartesian coordinates (x,y,z) of millions of atoms in real time. However, to view the atoms a visualization program called Amira is used in combination with the Lammps code. The Lammps code is modified to establish different film thicknesses and generates the coordinates for the atoms in real time, and Amira shows the atoms in motion, making it possible to view dislocation propagation, and grain boundary interactions associated with the applied force from the hardness test.[9]

3.2 Crystal Growth

To observe the hardness indent on a thin film, the different nickel films was simulated using the Voronoi grain growth method. This method is a program used to nucleate grains in a metal system utilizing the Y. Mishin EAM potential for nickel.[8] Several different grain structures were created for this experiment. Films were created as single grain perfect crystals, and crystals with three grains and varying misorientation angles of 5° and 10°. The dimensions of the film are 25nm in the $[1\bar{1}0]$ direction and 25 nm in the $[11\bar{2}]$ direction. Once the grains are nucleated, the internal stresses and grain boundaries are relaxed at 300 K by using the Lammps code. The final result of the relaxation is a tricrystalline nickel and single crystal thin film at ambient pressures between 0 and 100 bar. Figure 1 shows the structure and orientation of the relaxed samples used for indentation. The film surfaces are oriented normal to the [111] direction.

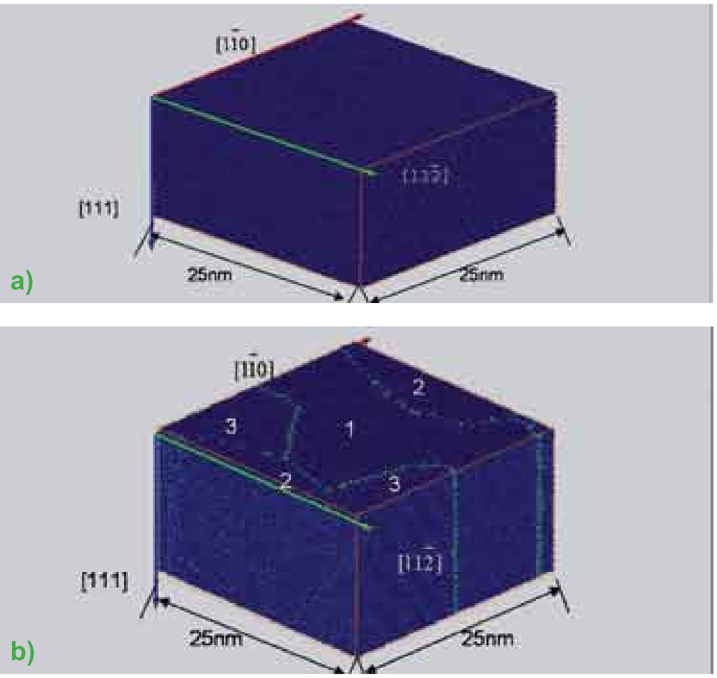

Figure 1. Structure and orientation of 12.8 nm a) single crystal and b) 10° tricrystal

3.3 Indentation Simulation

The next step is to simulate a hardness indent into the thin films using the Lammps code. A hardness indenter with a radius of 30.3 nm was chosen. The Lammps code is written to simulate the lowering of the indenter down the Z [111] direction into the various thin films. The optimal loading rate for observing the entire indentation process is 10 m/s. The force and atomic positions are outputs at 5 ps or 10 ps intervals until the hardness indent is completed after the tip travels a depth equal to 20% of the overall thickness. The simulation is performed at 300 K with the bottom surface as a fixed boundary condition in the [111] direction and periodic in the $[1\bar{1}0]$ and $[11\bar{2}]$ directions. The atoms in the fixed region are actually allowed to move within the (111) plane, but not along the [111] direction. The atomic positions are entered into visualization software (Amira) in order to view the indention process in real time 3-D visualization. Forces from the indenter are obtained during the experiment. The contact area is also calculated from the atomic positions and is used to obtain contact pressures.

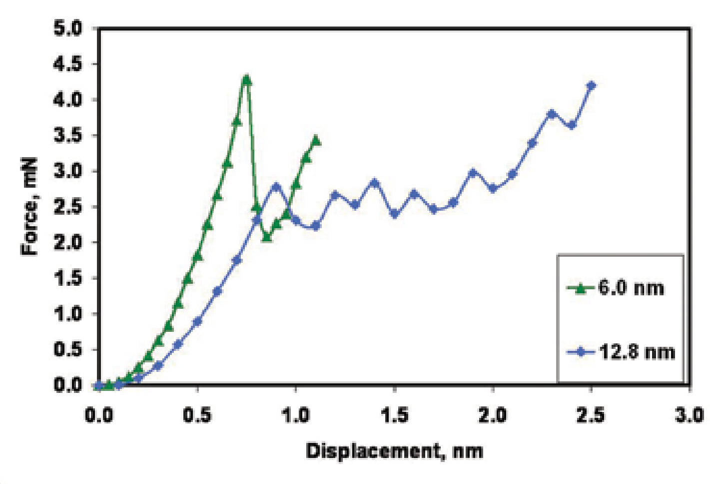

Figure 2. Force (N) vs. displacement (nm)

4. Results and Discussion

4.1 Effect of Film Thickness

Figure 2 shows the effect of thickness on the force displacement curves characteristic of the films. Figure 3 shows the simulated indentation of thin films of 6.0 nm and 12.8 nm, and Figure 4 shows the contact pressure of the indenter on the film surface for different values of film thickness. The trend that is observed is that the film thickness decreases the slope of the elastic response of the film increases. The visualization of the hardness indent showed the mechanisms responsible for the trends found in the previous graphs. Figure 2 shows the dislocation loops that were observed during the visualization of 6.0 nm and 12.8 nm sample.

In the elastic part of the indentation different slopes of the pressure versus indentation depth are observed for varying film thicknesses. However, the contact pressure necessary for the initiation of plasticity in the single crystal films is independent of the film thickness. Differences in the loops configuration are observed in the plastic part of the indentation. As the film thickness decreases, loops can not move as easily due to the fact that the space available for the dislocation loop is smaller. This impediment of formation and motion of dislocation loops leads to hardening of the material.

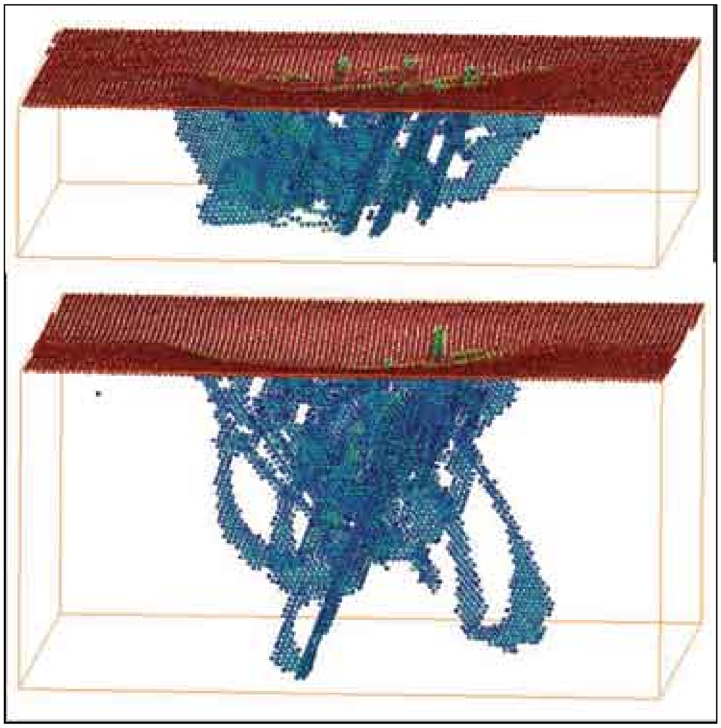

Figure 3. Indention of 6.0 nm film and 12.8 nm film at equivalent pressure of 38.10 GPa

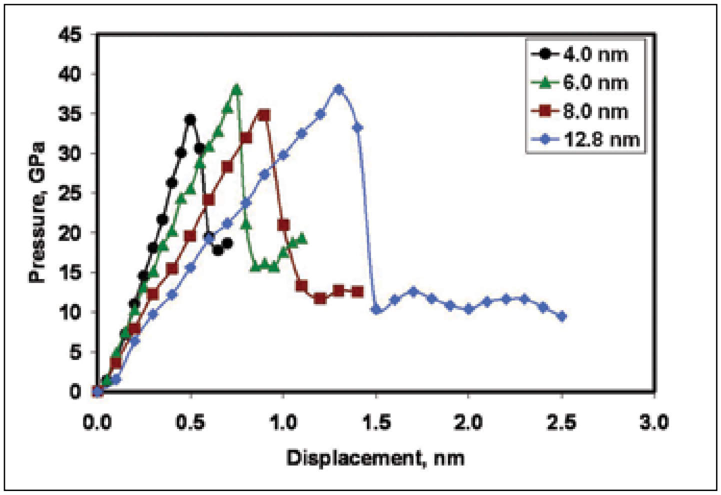

Figure 4. Pressure (GPa) vs. displacement (nm) of single crystal varying sample thickness

4.2 Effect of Grain Boundaries

From the pressure versus displacement graphs shown in Figure 3, films containing grain boundaries with misorientations of 5 and 10 degrees were used. The grain boundary planes were oriented perpendicular to the film surface. The initial linear region within the graph correlates to the elastic response of the films and the peaks correlate to the first dislocation emission. The films containing grain boundaries emit dislocations at lower contact pressures than single crystal. The higher pressures in the single crystal are due to the lack of defects within the system.

4.3 Dislocation Emitting Sites

The pressure versus displacement graphs shown in Figure 4 were studied along with the visualization of the sample to see where the dislocations were emitted. There were two locations where the dislocations initially were emitted: from the grain boundary or underneath the indenter. This comparison provided more understanding of the trend of higher pressure to emit the first dislocation in a single crystal than the lower pressure in a tricrystal, shown in Figure 5. Examples of the emitting sites are shown in Figure 6. In most cases for the tricrystalline films the dislocations emitted from initial defects. However, in some of the thinner tricrystalline films there were dislocations emitted in areas of the film with no defects. For these very thin films (40 nm) the grain boundaries were not effective emission sites for the dislocations. For the relatively thicker films the dislocations were emitted from the grain boundaries. In the single crystal films there were no initial defects and the first dislocation emitted from directly underneath the indenter every time.

4.4 Differences at the Nano Scale

One of the important reasons for simulation of nickel films was to view the different hardening effects at the nano scale. To summarize our results, Figure 7 shows that the elastic response (slope of pressure curve) is stronger, indicating much harder films at low thicknesses. Figure 7 also shows as film thickness increases, the hardness of the film begins to approach bulk hardness values. As the thickness of the film increases, another trend is apparent. Figure 8 shows that as film thickness increases, the effect of preexisting grain boundaries is stronger. In very thin films, the difference between a single crystal film and a tricrystal film is not as pronounced. In the larger films, the initial defects provide sources to form larger loops. In the smaller films these sources are still present in the tricrystalline

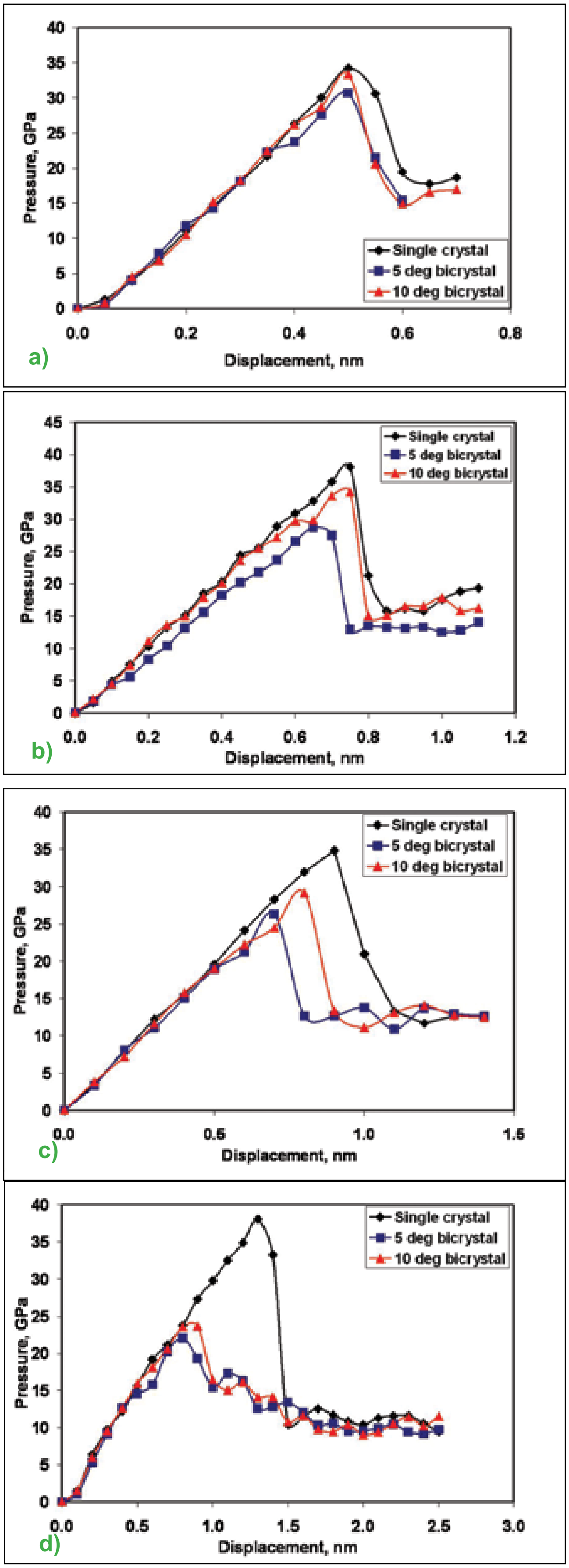

Figure 5. Pressure vs. displacement at a) 4 nm b) 6 nm c) 8 nm and d) 12.8 nm

films; however, there is not enough space between the surfaces of the film to generate a dislocation loop, this is caused by the size dependence from equation that follows:

$$s * = mb^2/(2L) \qquad (2)$$

This equation shows the critical stress of emitting a pure edge dislocation, where μ is the shear modulus of nickel with the value of 760 MPa, the burger's vector b = 2.5 Å and L the length of the dislocation loop.[10]

5. Conclusions

In the simulation of hardness indent into a nickel nano thin film the hardness increases with decreasing film thicknesses. One hardening mechanism with decreasing film thickness was the added constraint on the formation and motion of

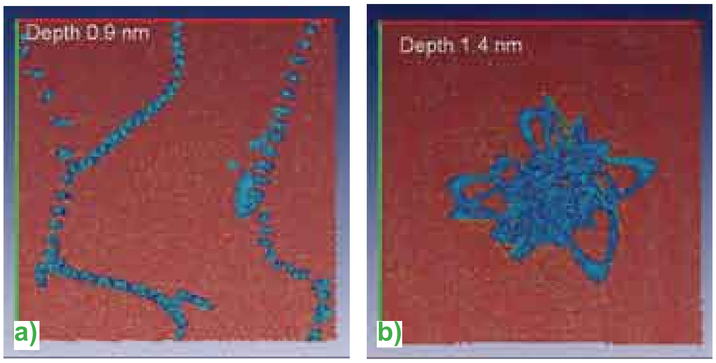

Figure 6. Emission of first dislocations in 12.8 nm thick film: a) 10deg bicrystal at a depth of 0.9 nm and pressure of 23.68 GPa b) single crystal at a depth of 1.4 nm and pressure of 33.28 GPa

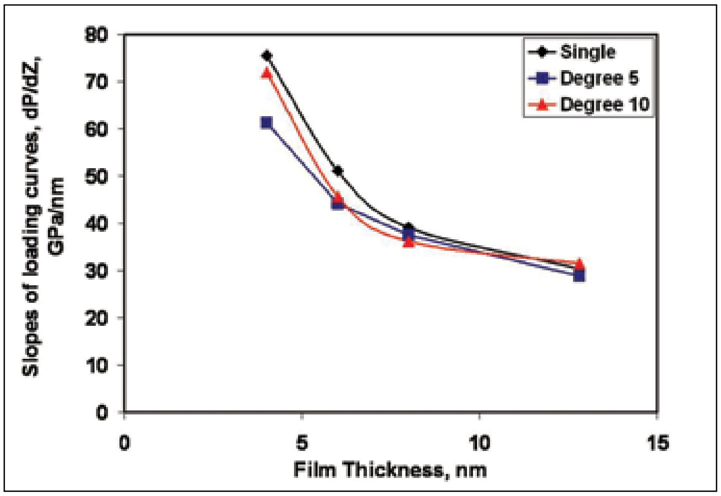

Figure 7. Slopes of loading curves vs. film thickness

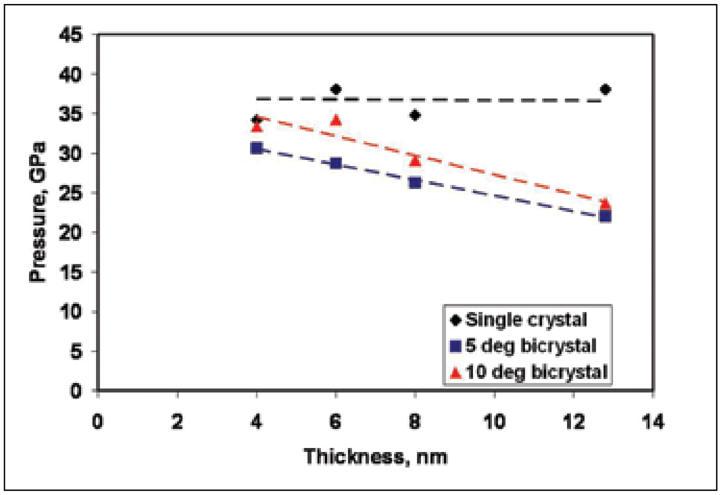

Figure 8. Peaks of loading curves vs. film thickness

dislocation loops. Hardness increases with decreasing thickness because there is less room for dislocation loops making it more difficult for the lattice to deform plastically.

In the simulation of a hardness indent into a nickel nano thin film the films with initial grain boundaries are not as hard as the single crystal films. This is to be expected because initial defects in the lattice provide sites for dislocation emission. In thicker films the presence of initial defects has a greater effect on hardness than in thinner films because the length between surfaces effects the emission of dislocation loops. As the radius of a dislocation loop increases, the force needed to emit the loop decreases.

Acknowledgements

We would like to acknowledge Dr. Farkas of Virginia Tech, graduate student Joshua Monk of Virginia Tech and graduate student Donald Ward of Brown University; for helping us in this project.

References

[1] Callister, William D. *Materials Science and Engineering, an Introduction*, Wiley, 2003.

[2] Cordill, M.J., Chambers, M. D., Lund, M. S., Hallman, D. M., Perry, C. R., Carter, C. B., Bapat, A., Kortshagen, U., Gerberich, W. W. *Plasticity Response in Ultra-Small Confined Cubes and Films*. 2005.

[3] Plimpton, S. J., Lammps Code, *Journal of Computational Physics*, 117, 1-19, **1995**, www.cs.sandia.gov/~sjplimp/lammps.html

[4] Finnis, Mike. *Interatomic Forces in Condensed Matter*. Oxford University Press, 2003, p 129-186.

[5] Hyde, Brian. Effects of Carbon on Fracture Mechanisms in Nanocrystalline BCC Iron – Atomistic Simulations, Virginia Tech Dissertation 2004, p 6-18

[6] Xie, Zhao-Yang. Atomistic Simulation of Dislocations Core Structures in B_2 NiAl Virginia Tech Dissertation Dec. 1993, p 9-13.

[7] Cabral Cardozo, Antonia Fernando. Computer Simulation of Grain Boundary Multiplicity in Ni_3Al. Virginia Tech Dissertation April 1991, p 12-17.

[8] Mishin, Y.; Mehl, M. J.; Papaconstantopoulos, D. A.; Embedded-atom potential for B_2-NiAl, *Physical Review B* 65, **1984**.

[9] www.amiravis.com

[10] Hirth, J.P; and Lothe, J. *Theory of Dislocations*. John Wiley & Sons, Inc. 1982.

[11] Deak, Peter; Frauenheim, Thomas; and Pederson, Mark R. *Computer Simulation of Materials at Atomic Level*. Wiley-VCH, 2000

About the Authors

Edward Parker

Edward Parker, originally from Raleigh, North Carolina, graduated from the Materials Science and Engineering program at Virginia Tech in the spring of 2006 with a bachelor degree. He obtained a job as a process engineer with Cree Inc. of Raleigh, NC, working with LED lighting.

Peter Gaudreau

Peter Gaudreau, originally from Woonsocket, Rhode Island, also graduated from the Materials Science and Engineering program at Virginia Tech in the spring of 2006 with a bachelor degree. He obtained a job shortly after graduation in Riverdale, Illinois as a metallurgist working with Mittal Steel.

Effect of Sintering Temperature, Heat Treatment and Tempering on Hardness of Sintered Hardened Grade Steels (SH737-2Cu-0.9C)

Saurabh Anand and Neerav Verma

Indian Institute of Technology, Department of Materials and Metallurgical Engineering
Kanpur, India 208016

Abstract

The present study examines the change in hardness of sintered hardened steel (SH737-2Cu-0.9C) sintered at different temperatures, heat treated by various methods and then tempered at different temperatures. The samples were transient liquid phase sintered at 1120 °C, 1180 °C and 1250 °C respectively. The sintered samples were characterized then for density and densification parameter. The samples were austenitized at 900 °C and cooled by four different methods viz. furnace cooling (annealing), air cooling (normalizing), oil quenching, and brine quenching. The samples were then tested for their hardness using Vickers's hardness at 10 kgf load. The trend of hardness observed was found minimum for air cooled and maximum for brine quenched. In case of sample sintered at 1250 °C, relatively higher hardness was observed. The oil and brine quenched samples were then tempered at 200 °C, 400 °C, 600 °C and 700 °C. The hardness pattern observed typically showed secondary hardness taking place (due to presence of Mn and Mo) and reaching the maximum around 600 °C.

Keywords: Sintered SH737-Cu-C steel, heat treatment, transient liquid phase sintering, quenching, tempering, secondary hardness

1. Introduction

In recent years, powder metallurgical (P/M) stainless steel components are increasingly being utilized for automotive and structural applications.[1] As compared to conventional casting techniques, P/M processing offers advantages such as lower processing temperature, near-net shaping, high final density, greater material utilization (> 95%) and a more refined microstructure that provides superior material properties.[2] In addition P/M products have greater microstructural homogeneity. The significant advances in powder production technology, new alloy design with novel properties, compaction and sintering furnace technologies boost up the growth of powder metallurgy.

The main thrust towards higher performance in powder metallurgy alloys has been achieved by introducing alloying additions such as Mo, Ni, Mn, and Cu. Most of the alloying additions enhance the strength through solid solution hardening during sintering. In addition, these alloying elements also enhance the hardenability by shifting the continuous cooling transformation curve to the right. Subsequent heat treatment results in enhancing the toughness of ferrous alloys. In addition, alloying can improve oxidation or corrosion resistance. Some applications rely on alloying to secure special magnetic properties or high temperature strength. Table 1 qualitatively shows that the alloys that are efficient in improving hardening tend to reduce the compressibility and high affinity for oxygen.

The alloying methods used for the production of ferrous P/M parts are divided into three groups: admixture of elements to a plain iron powder, diffusion bonded or partially prealloyed powders and completely prealloyed powders. Elementally admixed materials suffer heavily from segregation problems. Prealloyed iron powder though effective against segregation, significantly decreases the compressibility of the powders. In conventional powder metallurgy processing, "diffusion alloyed" powders have typically been used. This process involves heat treatment of iron powder and alloying elements in a reducing atmosphere, allowing partial diffusion and metallurgical bond formation prior to pressing and sintering. Due to partial diffusion, these powders have higher compressibility and fewer tendencies for small alloying elements to agglomerate, hence better homogeneity. The influence of chemical and microstructural homogeneity on the mechanical properties of sintered material has been studied by a number of authors.[3-5] A common alloying metal in powder metallurgy is copper, which is not sensitive to oxidation and causes sufficient increase in strength. Several sintered components are made for automotive applications by mixing copper and carbon with prealloyed iron. This material is sintered with a transient liquid phase, when copper content is less than 8%.[6-9] Formation of secondary pores at the site of original Cu particles is an inevitable consequence of transient liquid phase sintering.

This study focuses on the investigation of one such alloy, sintered hardened grade steel SH737 (designated), which has a nominal composition of Fe-1.25 Mo-1.4 Ni-0.42 Mn (wt%). The composition has been tailored with a view to alter the CCT curve characteristics in such a manner that during post sintering cooling, the sintered compact undergoes a transformation in the bainitic/martensitic region. This grade of powder has also been referred to as a sinter-hardening grade. As the name suggests, sinter-hardening achieves sinter and hardening in a single step.

2. Experimental Procedure

For the present investigation, a partially prealloyed powder mixture (Fe, 1.4 wt% Ni, 1.25 wt% Mo, 0.42 wt% Mn, 2 wt% Cu, and 0.9 wt% graphite), produced using a proprietary process developed by Hoeganaes Corp, was used as a starting material. [10,11] The as-received powder was characterized for its flow behavior as well as apparent and tap density using set MPIF standards. The results are shown in Tables 2 and 3 and in Figure 1.

Table 1. Qualitative ranking of alloying elements in prealloyed materials

	Hardenability factor	Effect on compressibility	Affinity for Oxygen
Higher	Manganese	Copper	Manganese
↓	Chromium	Nickel	Chromium
	Molybdenum	Chromium	Nickel
	Copper	Manganese	Molybdenum
Lower	Nickel	Molybdenum	Copper

Table 2. Composition of the powder

Elements	Fe	Mo	Mn	Ni	Cu	C
% (by wt)	94.03	1.25	1.4	0.42	2	0.9

Table 3. Characteristics of experimental powder

Source	D_{10} (μm)	D_{50} (μm)	D_{90} (μm)	Mode size, (μm)	Width of distribution (μm)	Apparent Density, (g/cm^3)	Tap Density, (g/cm^3)	Flow Time, (s/50g)
Hoeganaes	32	58	88	75	0.47	3.62	3.98	20

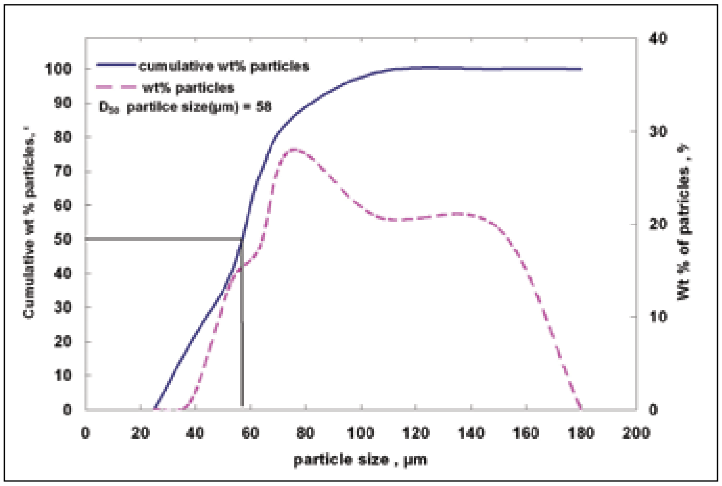

Figure 1. Weight percent of the powder particles vs. particle size

The received powder was compacted at 600 MPa in a 50 ton uniaxial hydraulic press (APEX Construction Ltd, UK). To minimize friction, the compaction was carried out using zinc stearate as a die wall lubricant. The density of compacted specimens was between 6.99 and 7.02 g/cm^3. The powder contained 0.75 wt. % acrawax, which was added to the powder to facilitate its compaction during sintering. The sintering response on densification and microstructures was evaluated on cylindrical pellets (16 mm diameter and 6 mm height). The green compacts were dewaxed in a tubular silicon carbide (SiC) furnace under a 80% N_2-20% H_2 atmosphere. The lubricant was removed from the green samples using a heat treatment at 850 °C for 30 min. To prevent cracking of green compacts by thermal shock, the compacts were slowly heated at 5 °C/min. They were then sintered at three different temperatures, i.e. 1120 °C, 1180 °C and 1250 °C respectively for 30 min in a tube furnace with a SiC heating element. The thermal profiles for the sintering are shown in Figure 2. All the sintering was carried out under a 80% N_2-20% H_2 atmosphere.

The sintered density was obtained by dimensional measurements. The densification parameter was calculated to determine the amount of densification occurred during sintering. It is expressed as:

$$\text{Densification parameter} = \frac{(\text{sintered density - green density})}{(\text{theoretical density - green density})} \quad (1)$$

The sintered samples were heat treated at 900 °C for one hour and subsequently cooled by four different methods: furnace cooling (annealing), air cooling (normalizing), oil quenching and brine quenching. The samples were polished to mirror finish and ultrasonically cleaned in acetone, followed by etching in 3% Nital. Bulk hardness of the samples was measured by LECO V - 100 - C1 Vickers hardness tester at 10 kgf load using a pyramidal shaped diamond indenter. The load was applied for 10 seconds. The recorded hardness values are the averages of five readings taken at random spots throughout the sample.

The oil and brine quenched samples sintered at different temperatures were tempered at four different temperatures (200 °C, 400 °C, 600 °C and 700 °C) for 2 hours. The microstructural analysis of the samples was carried out through optical microscopy, and then bulk hardness was measured using Vickers hardness tester at 10 kgf load.

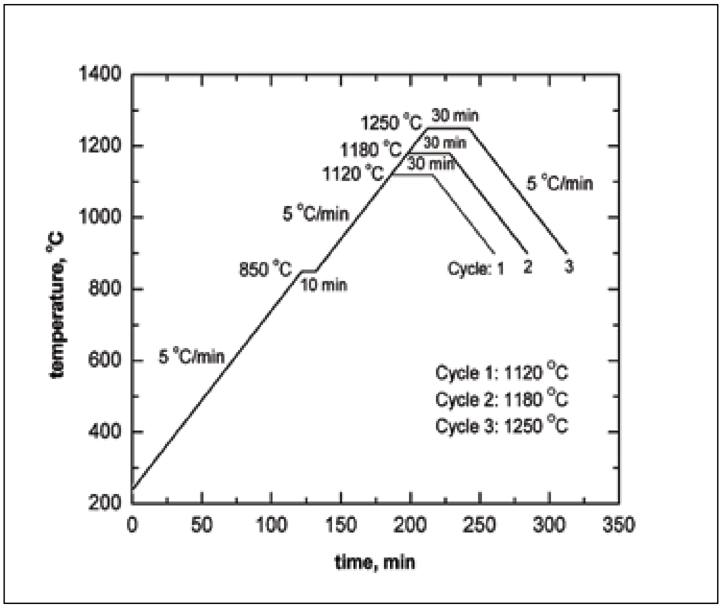

Figure 2. Sintering temperature profiles for SH737-2Cu-0.9C

3. Results and Discussion

Figure 3 shows the effect of sintering temperature on the densification response of SH737-2Cu-0.9C alloys. It is quite evident from the figure that the sintered density improves (~0.5%) with increased in sintering temperature from 1120 °C to 1250 °C. To take into account the effect of composition, all the sintered densities were normalized with respect to the respective theoretical densities. The sintered sample contains nearly 11-12% porosity. It can be inferred that the temperature has marginal effect on the densification of these alloys.

In order to account for the effect of green density on the sintered density, the densification response was qualified in terms of densification parameters. Variation of densification parameter with temperature is shown in Figure 4. The densification parameter is negative for the sintering temperatures 1120 °C and 1180 °C, thus confirming compact swelling. The

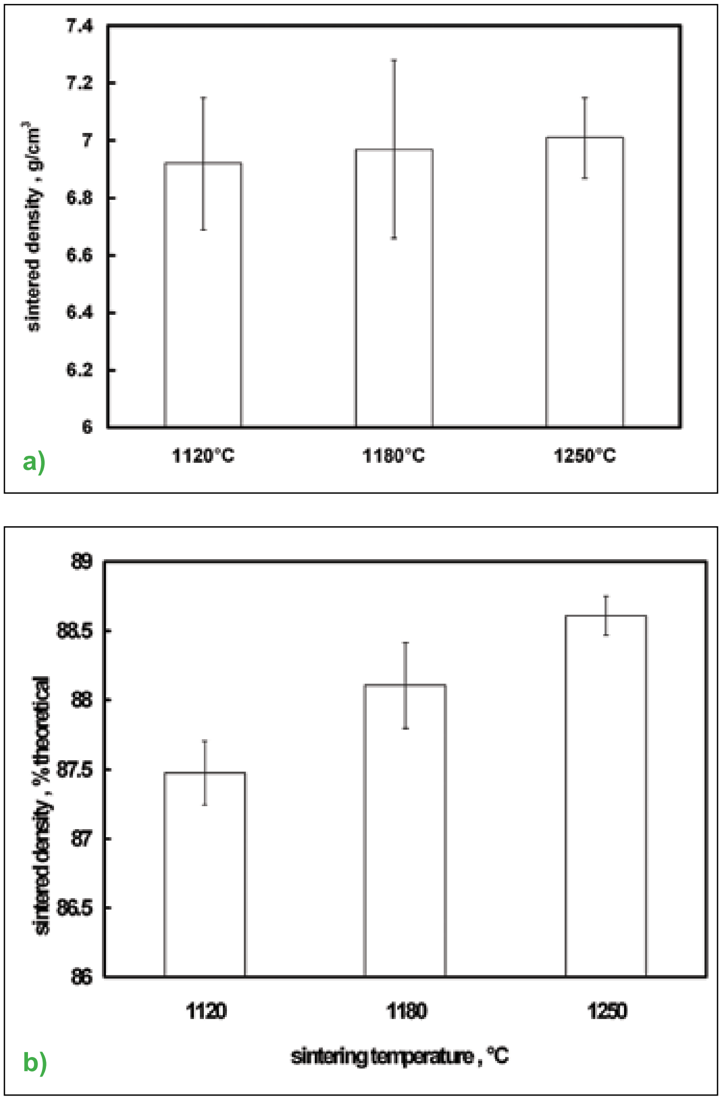

Figure 3. Effect of sintering temperature on densification: a) density b) percent theoretical density

parameter is positive for 1250 °C, thus exhibiting marginal increase in densification parameter with sintering temperature.

Table 4 shows that furnace cooling leads to the lowest hardness regardless of sintering temperature. The trend of hardness is as follows:

Furnace cooled<Air cooled<Oil quenched<Brine quenched

This can be attributed to the formation of martensite and bainite in the case of higher rate of cooling (as in oil and brine quenching).

Figure 5 shows the effect of sintering temperature on the hardness of SH737-2Cu-0.9C alloy samples cooled by various methods. It is evident from the graph that bulk hardness improves with increasing sintering temperature from 1120 °C to 1250 °C, which can be attributed to the sintered density, because there was a marginal densification achieved with increasing sintering temperature. Higher densification implies lower porosity, hence better heat transfer leading to high hardness. A higher sintering temperature further enhances the microstructural homogeneity due to inter-diffusion of alloying elements. This contributes to the enhancement of the bulk hardness, which also increases with the formation of bainite at higher sintering temperature due to comparatively faster cooling.

Figure 6 and 7 show the hardness pattern of tempered oil and brine quenched samples. The hardness increases up to 600 °C, attains a maximum, and then decreases, which is due to secondary hardening taking place in the quenched samples. Secondary hardening occurs due to presence of carbide formers like Mn and Mo above 500 °C. These elements have high diffusivity to nucleate and form a fine dispersion of alloy carbides producing secondary hardening. Secondary hardening is a process similar to age hardening, where coarse cementite particles are replaced by a new and much finer dispersion of Mo_2C and Mn_2C stable carbides. The critical dispersion causes a peak in the hardness as the carbide particles slowly coarsen, causing their strengthening ability to decrease, leading to an overall decrease in hardness.

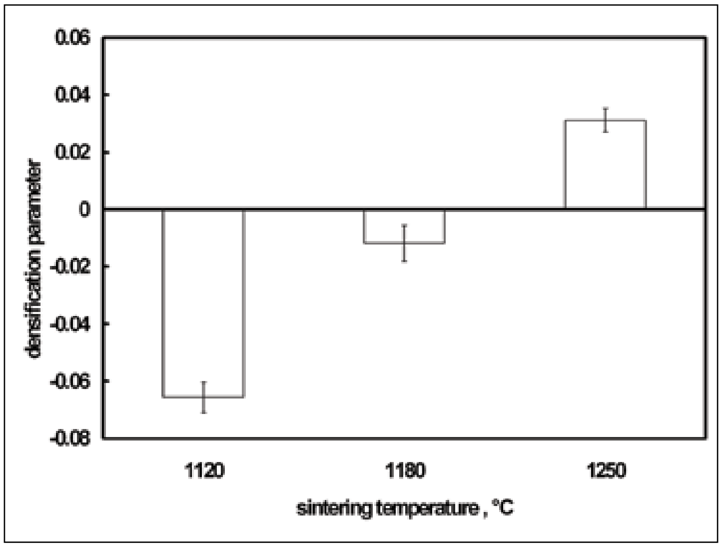

Figure 4. Effect of sintering temperature on the densification response

Table 4. Bulk hardness values of SH737-2Cu-0.9C sintered at three different temperatures (1120 °C, 1180 °C and 1250 °C) and then cooled by different methods

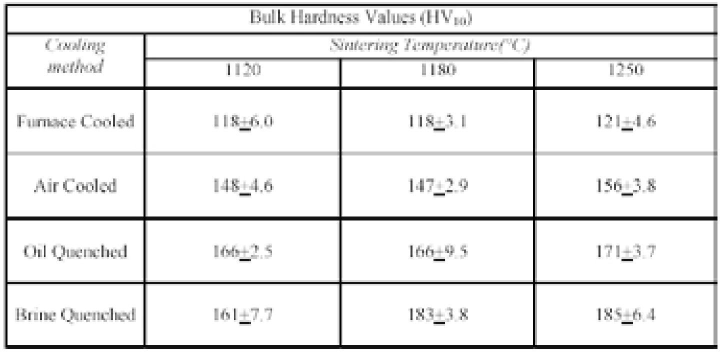

Bulk Hardness Values (HV_{10})			
Cooling method	Sintering Temperature(°C)		
	1120	1180	1250
Furnace Cooled	118±6.0	118±3.1	121±4.6
Air Cooled	148±4.6	147±2.9	156±3.8
Oil Quenched	166±2.5	166±9.5	171±3.7
Brine Quenched	161±7.7	183±3.8	185±6.4

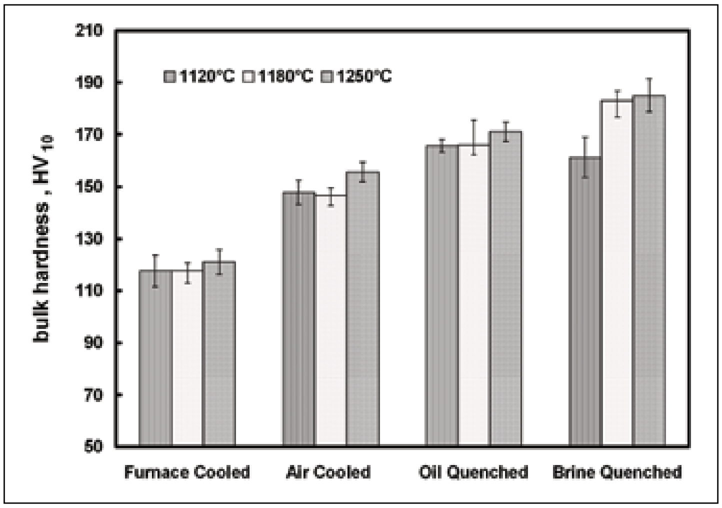

Figure 5. Bulk hardness of SH737-2Cu-0.9C samples sintered at different temperatures and cooled by different methods

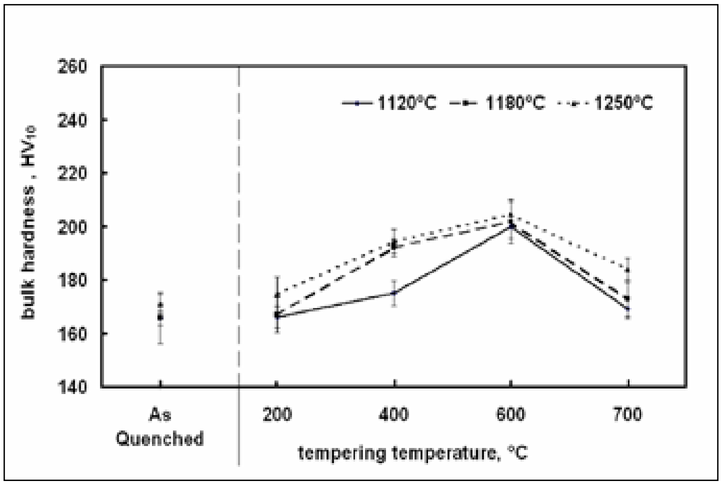

Figure 6. Effect of tempering temperatures on hardness of oil quenched SH737-2Cu-0.9C samples sintered at different temperatures

The hardness values in Table 5 and 6 show that the as-sintered samples have the same hardness as that achieved by brine quenching followed by tempering at 600 °C.

4. Conclusion

Sintered hardened grades have an advantage over simple carbon steels, as they do not require secondary processing, which is evident from the above data. The hardness of sintered SH737 samples is the same as that obtained from heat treatment and tempering, allowing the secondary hardness to take place. Sinter hardened steels have an enormous processing time advantage over simple carbon steels.

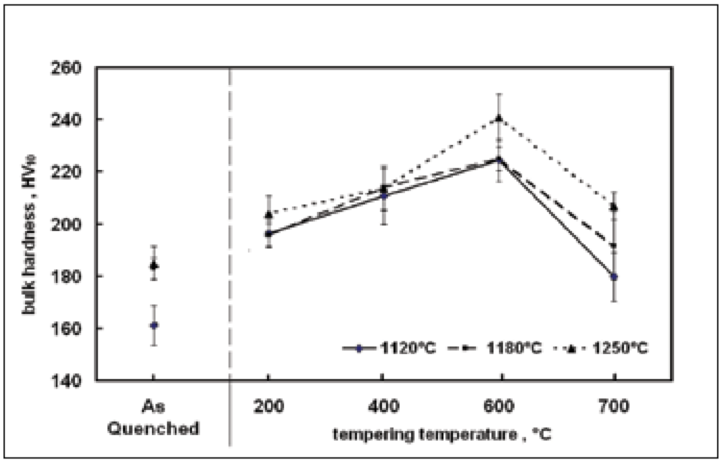

Figure 7. Effect of tempering temperatures on hardness of brine quenched SH737-2Cu-.9C samples sintered at different temperatures

Table 5. Bulk hardness values of oil quenched samples at different tempering temperatures for SH737-2Cu-0.9C for different sintering temperatures

Bulk Hardness Values (HV_{10}) for Oil Quenched + Tempered samples					
Sintering Temperature	As sintered hardness values	Tempering Temperature(°C)			
		200	400	600	700
1120°C	226 ± 4.3	166 ± 4.1	175 ± 4.7	200 ± 4.2	169 ± 3.8
1180°C	232 ± 9.4	167 ± 6.9	192 ± 3.2	202 ± 8.2	173 ± 6.3
1250°C	239 ± 4.9	174 ± 6.6	194 ± 4.4	204 ± 4.7	184 ± 4.0

Table 6. Bulk hardness values of brine quenched samples at different tempering temperatures for SH737-2Cu-0.9C for different sintering temperatures

Bulk Hardness Values (HV_{10}) for Brine Quenched + Tempered samples					
Sintering Temperature	As sintered hardness values	Tempering Temperature(°C)			
		200	400	600	700
1120°C	226 ± 4.3	196 ± 5.1	211 ± 10.6	224 ± 8.3	180 ± 9.3
1180°C	232 ± 9.4	196 ± 4.6	214 ± 8.3	225 ± 4.6	192 ± 13.1
1250°C	239 ± 4.9	204 ± 6.8	214 ± 8.6	241 ± 9.0	207 ± 5.3

Acknowledgements

The authors gratefully acknowledge Dr. Anish Upadhyaya, Associate Professor, Department of Metallurgical & Materials Engineering., IIT Kanpur, for his expert supervision and Dr. Narasimhan, Hoeganaes Corporation for providing us with the working powders.

Reference

[1] German, R. M. *Powder Metallurgy Science; 2nd ed.* Metal Powder Industries Federation: Princeton, NJ, USA, 1994.

[2] Kaysser, W. A.; Petzow, G. Present State of Liquid Phase Sintering. *Powder Metallurgy* **1985**, *28*(3), 145-150.

[3] Wastenson, G. Method of Extending the Applicability of Sintered Steel. *Powder Metallurgy* **1975**, *18*(35), 124.

[4] Sonsino, C. M.; Schlieper, G.; Huppmann, W. J. Influence of Homogeneity on the Fatigue Properties of Sintered Steel. *International Journal of Powder Metallurgy and Powder Technology*, **1984**, *20*(1), 45.

[5] Vityaz, P. A.; Nasybulin, A. K. Homogenization in Sintering and its influence on Mechanical Properties of Fe-Cr-C and Fe-Ni-C Steels. *Powder Metallurgy*, **1985**, *28*(3), 166.

[6] Danninger, H. *Powder Metallurgy International*, **1987**, *19*(1).

[7] Cimino, T. M.; Graham, A. H.; Murphy, T. F. *Industrial Heating* **2000**, *September.*

[8] Christian, K. D.; German, R. M. *International Journal of Powder Metallurgy* **1995**, *31*(1), 51-61.

[9] Smith, Y. E. *International Journal of Powder Metallurgy & Powder Tech* **1978**, *14*(2), 85.

[10] Chawla, N.; Fillari, G.; Narasimhan, K. S. in *Powder Materials: Current Research and Industrial Practices*. F.D.S. Marquis. Ed. TMS: Warrendale, PA, 1999; pp 247.

[11] Luk, S. H.; Hamill. Jr., J. A. *Advances in Powder Metallurgy and Particulate Materials*, Metal Powder Industries Federation: Princeton, NJ, 1993; pp153.

About the Authors

Saurabh Anand

Mr. Anand is currently pursuing his degree from the Department of Materials and Metallurgical Engineering at the Indian Institute of Technology, Kanpur. He has always been fascinated by the practical application of intellectual and conceptual knowledge. Recently, he has become absorbed in empirical works on powder metallurgy. Saurabh worked on a paid research project on sintered hardened grades of steel powders which included investigation of its densification, mechanical properties, and microstructural evolution. He recently completed a summer internship in an exchange program by the Australian government working on "Nanostructured Materials and Materials with Inhomogeneous Microstructure."

Neerav Verma

Neerav Verma is a senior undergraduate student of Materials and Metallurgical engineering in Indian Institute of Technology, Kanpur, India. The versatile field of Material science has always captivated him and the research areas in it have inspired him to explore them and ameliorate his knowledge to come up with decent research work. He has been involved in a rigorous research work in the field of Powder Metallurgy which included "Investigation Of Densification And Microstructural Evolution Of Sinter-Hardening Alloy Steels." He has also worked in the field of characterization of Construction Materials during his 2006 summer internship at LMC Lab, EPFL, Lausanne, Switzerland.

Microwave Sintering of Simulated Moon Rock

Michael Hunt, Amy Ducut, and Christina Lee

Virginia Polytechnic Institute and State University, Department of Materials Science and Engineering
Blacksburg VA, 24061

Abstract

The focus of this research was to determine the feasibility of using microwave energy to sinter simulated moon rock. Microwave processing is often used as an alternative to traditional sintering of ceramic materials for its energy efficiency and decreased sintering times. In lunar applications, microwaves would be a more useful for sintering than traditional methods because microwave devices may be transported more easily and with less cost. As found, moon rock does not have the needed physical and thermal properties suitable for its use as a structural material for a lunar base or orbiting structure.[1,2] However, sintered moon rock may have those required characteristics. To evaluate the potential for using microwave energy to sinter simulated moon rock, both stand-alone and hybrid heating methods were tested. Based on collected data, an 1100-watt commercial microwave oven can emit enough energy to rapidly reach the sintering temperature of moon rock using hybrid heating methods. Further research needs to be conducted to compare the physical characteristics of moon rock sintered conventionally and with microwave energy.

Keywords: Microwave sintering, simulated moon rock, regolith

1. Introduction

The construction of a lunar station has been stifled by the limitations of earth-moon transportation, namely the large expense of carrying the additional mass and volume of construction materials upon space shuttles.[1,2] A seemingly simple solution to this transportation problem is to use the available materials on the moon to build structures.

1.1 Lunar Soil and Simulants

In order to understand how these materials may be processed in a microwave field, it is important to understand how materials act in a microwave field. Research divides materials into three categories when microwave processing is discussed. Materials can be opaque, transparent, or absorbent under microwave energy.[3] The main property that dictates which category a material belongs to is the dielectric loss of the material. If there are differences in dielectrics within a given material, the microwaves will interact differently with each phase, creating local inhomogenities. A combination of liquid and solid phases develops (transient liquid-phase sintering), resulting in improved mechanical properties. This type of heating is a likely outcome for materials with various constituents like lunar rock.[2]

Since as found moon rock does not have the needed physical and thermal properties that will allow its use as a structural material for a lunar base, it will be necessary to sinter this material.[1,2] The sintered moon rock may have the required characteristics to make it a structural material. The development of microwave processing technology could allow moon rock to be used as a structural material, bypassing the expense of bringing materials to the moon.

The material used in this study is similar to the dust found on the moon's surface, with the major difference being that the dust on the moon contains a nanophase iron on its surface. The presence of nanophase iron on the surface of real lunar soil grains is particularly beneficial to microwave processing. The nanophase iron particles add to the adhesion and strength of the overall aggregate also creating additional fusion of particles. Nanophase iron on the surface of grains forms fine melts acting as a glass binder (thus providing a transient liquid-phase sintering situation).[2] Since the stimulant used in this study does not contain this phase, it was expected that research using this stimulant would be more difficult than the actual process may be.

1.2 Microwave Technology

In many instances, microwave processing improves upon conventional heating methods because it can provide a precisely controlled, energy-efficient method of heating. This efficiency stems from one of the intrinsic characteristics of microwave processing – volumetric heating. For materials that are almost transparent to microwaves, stand-alone microwave processing will heat the materials from the inside to the outside, allowing for reduced sintering times and temperature. Also, microwave processing has been used in conjunction with conventional processing to achieve an improved uniformity that neither could achieve singularly. The combination of microwave processing and conventional sintering is known as microwave hybrid heating.

Current literature suggests that only limited studies of the traditional sintering process of regolith have been performed. The addition of a microwave sintering study of regolith would fill this gap in current research.[2]

This paper discusses the use of microwave hybrid heating to sinter pressed regolith pellets in 700-watt and 1100-watt commercial microwaves.

2. Experimental Procedure

The consistent production of uniform sample pellets greatly determined the repeatability of this research. Microwave energy absorption within the pellets may have differed with density gradients, porosity, and general pellet uniformity, and this variation may have affected the sintering process and the resulting sample characteristics.

2.1 Sample Pellet Preparation

A three-piece die assembly was used to produce cylindrical pellets under bi-axial loading conditions. The die was cleaned thoroughly to ensure no loose powders, dust, or debris remained on die surfaces. After cleaning the surfaces, a release spray was used to lubricate the die cavity.

Approximately 0.3 grams of dry raw regolith powder was measured using a laboratory scale accurate to three decimal places. One drop of room temperature tap water was then added to the powder using a pipette. Following the addition of water, the slurry was mixed with a small utensil to evenly distribute the water until the powder became moist and clay-like. The wet mixture was placed in the die and pressed at 9800 psi at room temperature. The sample was removed and then dried at 100°C for one hour in a conventional oven.

2.2 Microwave Modifications

Commercial microwaves have historically varied their energy output by using a duty cycle function. The duty cycle determined length of time the power cycles on and off and is pre-programmed for each power setting. Most home-model microwaves are not equipped for measuring high temperatures.

The first modification was to enable temperature measurement capabilities, as shown in Figure 1. Two thermocouples could be inserted from the top of the microwave cavity and measure two different temperatures simultaneously, which is done to verify a functioning hybrid heating setup.

Other modifications included sealing the microwave cavity to prevent the leaking and the removal of extraneous electronic equipment to reduce the complexities of the system.

2.3 Sintering Study

For the initial hybrid heating tests, the moon rock powder was contained in a quartz crucible which was placed inside of a larger quartz crucible containing silicon carbide (SiC). The entire setup was then placed onto a piece of space shuttle tile (high temperature reusable surface insulation – silica based) as shown in Figure 1.

The wet-pressed pellet samples were used in the testing of a 25 wt % SiC - 75 wt % alumina (Al_2O_3), suscepting casket for use in hybrid heating sintering. The casket was tested on different power settings and for different time periods in an effort to create a sintering profile for the casket. The setup for these tests is shown in Figure 2.

Wet-pressed pellet samples were also processed in a conventional furnace to act as a control group against the microwave-sintered samples. These conventionally sintered samples were used to determine acceptable relative density and possible microstructure of a sintered sample of simulated moon rock.

2.3 Data Analysis

The temperature measurements for all of the stand-alone and hybrid heating powder tests were plotted and analyzed to determine the feasibility of using each method for sintering. The data collected from the 700- and 1100-watt microwaves were compared to determine how the differences in power level affected

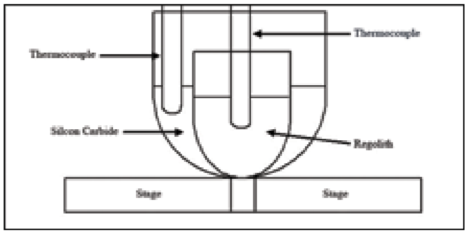

Figure 1. Schematic of hybrid heating w/ powder

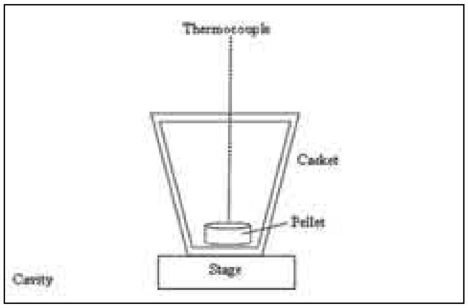

Figure 2. Schematic of susceptor casket w/ pellet

the temperatures achieved in stand-alone and hybrid heating methods.

Temperature measurements from both the hybrid heating and stand-alone heating methods were used to determine the feasibility of sintering simulated moon rock. The temperature profiles obtained from these tests were used to make comparisons between heating rates in each processing method.

3. Results and Discussion

The initial microwave absorbency test was designed to demonstrate the capability of regolith to absorb microwave energy at room temperature. The melting temperature of regolith, as taken from the literature, is approximately 1100º C.[3] An ideal sintering temperature is approximately two-thirds of the melting temperature, or about 750 °C.

As shown in Figure 3a, the temperature measured in the stand-alone set up was not sufficient to reach the desired sintering temperature. This plot shows the temperature of regolith as it heated in the 700-watt microwave oven on high power for ten

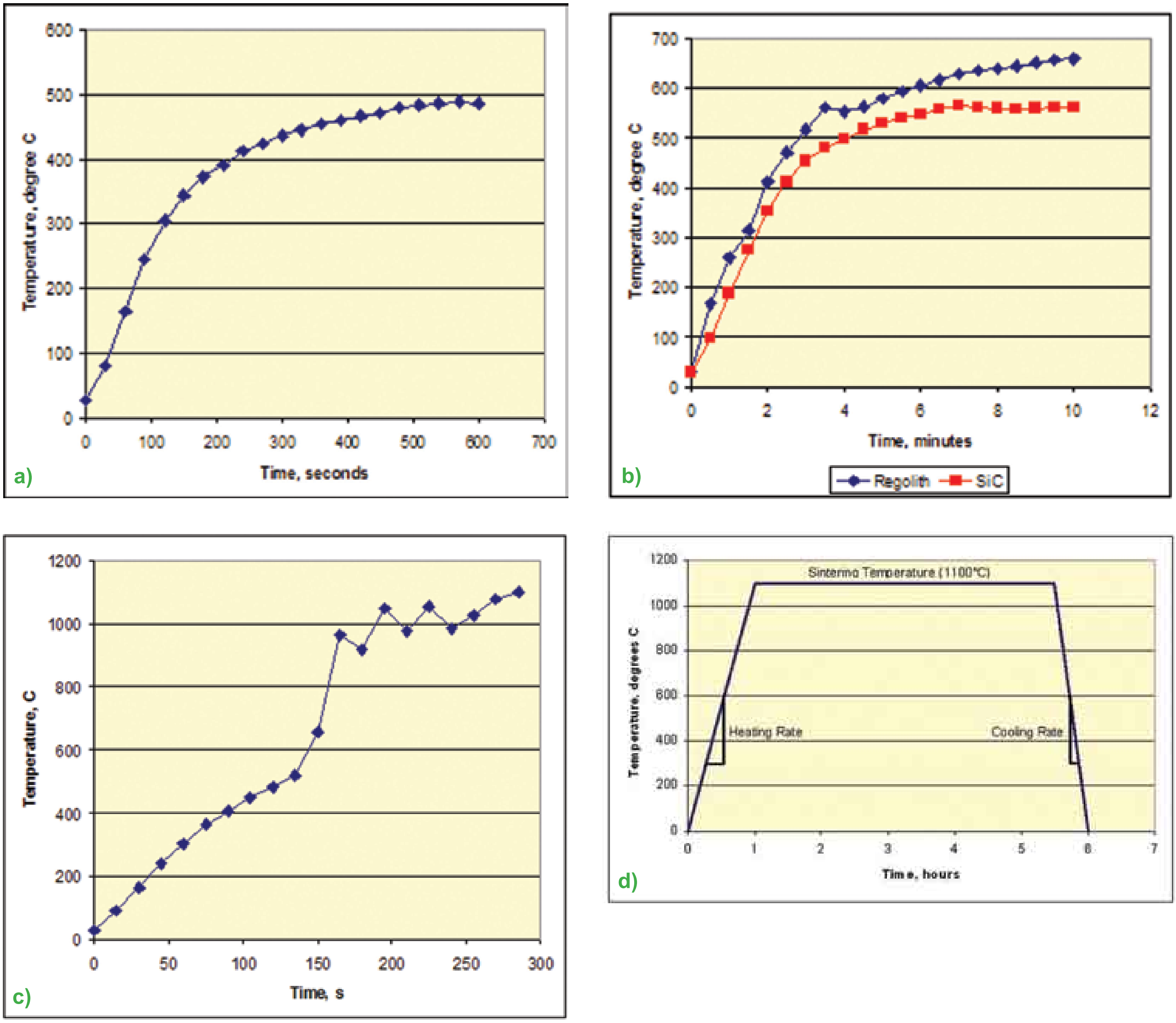

Figure 3. Heating curves for: a) stand alone microwave absorbancy test 700-watt microwave, 100% power b) hybrid heating of powered simulated moon rock 700-watt microwave, 80% power c) susceptor heating of pellet 1100-watt microwave, 80% power d) sintering profile for conventional processing of pellet

minutes. As the graph suggests, regolith could not be sintered using this technique because the temperature plateaued at only 500 ºC.

A hybrid heating setup was created to enhance the absorption characteristics of regolith. Typically an increase in the ambient temperature of a microwave absorbent material will increase its ability to respond to microwave energy during hybrid heating. This setup was tested on 80% power for ten minutes in the 700-watt microwave. Figure 3b shows the temperatures of both the regolith powder and the silicon carbide used to heat the regolith.

The temperature of the regolith plateaued just under the 700 ºC mark. Although this was still below the desired sintering temperature, it was significantly greater than the temperature achieved by stand-alone microwave processing. This test demonstrated that hybrid heating could obtain higher temperatures with lower power settings when compared to the stand-alone at full power.

The data also suggested that both the regolith and the silicon carbide were not absorbing significant amounts of microwave energy. Silicon carbide alone often reached peak temperatures (~1200 ºC) within two minutes of microwave heating. Given that the silicon carbide could not reach its peak temperature after ten minutes, it was not absorbing much microwave energy.

As a result, the data suggested that even with hybrid heating, a 700-watt microwave was not sufficient to sinter our regolith composition. All tests completed after this point were completed in the 1100-watt microwave.

The use of a suscepting casket (25 wt% SiC-75 wt% Al2O3) and a pellet was the ideal laboratory setup. This setup was heated at 80% power for four minutes and 45 seconds in the 1100-watt microwave. Figure 3c and 3d shows the heating of the regolith pellet in comparison to a conventional heating curve and illustrates the differences in time required to process using hybrid heating instead of conventional processing. Figure 3 illustrates the ability of regolith to reach its sintering temperature using a suscepting casket containing 25 wt% SiC. In addition, a lower power setting seemed to help slow down the heating process and to maintain the sintering temperature for longer periods of time.

Figure 4. Regolith glass on tip of thermocouple

The oscillating waves in Figure 3a stem from the data point measurements and the coinciding duty cycle of the microwave.

The result of using a suscepting casket and the 1100-watt microwave was not sintered regolith, but melted regolith. Figure 4 is a photograph of regolith glass bubble attached to the end of a thermocouple. The ability to reach the melting temperature of regolith indicated one significant fact—the sintering temperature was reached and surpassed.

4. Conclusions

Based on the data collected during this research, the microwave energy from the 700-watt microwave is not sufficient to sinter simulated moon rock. However, the 1100-watt microwave did provide sufficient energy to create microstructual changes, such as melting and sintering. This study also shows that it is possible to heat simulated moon rock much more rapidly using hybrid heating than conventional processing. The rapid heating may allow for unique microstructures that may not be obtained with conventional heating.

5. Future Work

Although this research did not produce sintered samples of simulated moon rock, did result in glass samples of regolith, indicating that sintering is theoretically possible. Research to produce sintered samples of simulated moon rock should be pursued in the future.

Once sintered samples are produced, a study of their mechanical properties should be completed. A comparison of the mechanical properties of conventionally sintered and microwave-sintered samples should also be pursued.

In addition, a detailed study of the differences in microstructure in conventionally and microwave-sintered samples should be conducted to determine what features in the microstructure contribute to the mechanical properties of the final products.

Acknowledgements

The authors would like to thank Dr. David Clark, Ms. Diane Folz, and Dr. Marie Paretti for their assistance and guidance in the research described herein during the 2005-2006 school year. They would also like to show appreciation to the Materials Science and Engineering Department at Virginia Tech for funding their research. Gratitude also goes to David Berry, Carlos Folgar, Matt Lynch, Morsi Mahmoud, and Patricia Mellodge for their assistance in giving the authors access to equipment and training with different pieces of equipment.

References

[1] Beck, A., Fabes, B.D., Poisl, W.H., Raymond, L.A. *Processing and Properties of Lunar Ceramics*. Department of Materials Science & Engineering, University of Arizona. American Institute of Aeronautics and Astronautics, Inc. AIAA-92-1668, 1992.

[2] Meek, Thomas T., Taylor, Lawrence A. (2005). Microwave Sintering of Lunar Soil: Properties, Theory, and Practice. *Journal of Aerospace Engineering*, **2005**, 18(3), 188-196.

[3] Clark, David E., Sutton, Willard H. *Microwave Processing of Materials. Annual Reviews,* Inc. Vol, 26. 1996, p. 299-331.

About the Authors

Amy Ducut

Amy graduated with a Bachelors of Science in Materials Science and Engineering from Virginia Tech in the spring of 2006. Currently, she is the Production Supervisor at Wyeth Pharmaceuticals in Richmond, VA. She enjoys working with people and using her materials background to make others better. During her spare time she enjoys participating in service projects and loves giving back to the community around her.

Michael Hunt

Michael graduated with a Bachelors of Science in Materials Science and Engineering from Virginia Tech in the spring of 2006. He plans to pursue a Masters of Science in Materials Science and Engineering from Virginia Tech. He has a passion for research and during the summers of 2005 and 2006, he did research at the Naval Surface Warfare Center in Bethesda, MD and at Virginia Tech respectively. He has an interest in high- temperature ceramics and materials characterization.

Christina Lee

Christina graduated with a Bachelors of Science in Materials Science and Engineering from Virginia Tech in the spring of 2006. She is currently working for Michelin as an engineer in Greenville, SC. She has a passion for animals, the environment, and green engineering. In her spare time she enjoys being outdoors, reading interesting books, and caving.

A Guide to the Calculation of Theoretical Densities of Crystal Structures for Solid Oxide Fuel Cells

Rachel Rosten, Matt Koski and Eric Koppana

Michigan Technological University, Department of Materials Science and Engineering
Houghton, Michigan 49931

Abstract

Theoretical density is an important parameter used to estimate the porosity of materials after sintering, especially if the requirements for the materials' densities are strict, such as in the case of the parts of solid oxide fuel cells. In this research paper, we provide examples of theoretical density calculations using unit cell structure and X-ray diffraction determined lattice parameters for a number of different ceramics, which are important for energy applications. Oxide perovskites, fluorites and rock salts were all investigated.

Keywords: Solid oxide fuel cells, lattice parameter, perovskite, fluorite

1. Introduction

The need for alternate forms of energy is apparent with increasing oil prices and growing concern over the limited supply of fossil fuels. Research addressing alternative energy sources continues to increase, especially in the area of fuel cells. One type of fuel cell receiving considerable attention is the solid oxide fuel cell (SOFC). Like other fuel cells, SOFCs release no polluting emissions, their only byproduct being water, and they are also much more efficient than current methods of electricity production.[1]

Solid oxide fuel cells are composed of an anode, a cathode, and an electrolyte sandwiched between them, all three of which are made from ceramics. As displayed in Figure 1, when the fuel cell is operating, oxygen molecules from air are doubly ionized on the cathode side of the fuel cell. These ions then pass through the oxygen permeable electrolyte to the anode.[2] The cathode is commonly composed of perovskite materials, such as Sr- or Ca-doped $LaMnO_3$, while the electrolyte is often composed of Yttria-stabilized zirconia.[3] On the anode side of the SOFC, hydrogen molecules are positively ionized and combine with the oxygen ions that have diffused through the electrolyte, forming water as a byproduct. Anode materials are typically composed of Ni/Yttria-stabilized zirconia.[3] The electrons released by the ionized hydrogen create a current that can be used to provide power to external devices as they return to the cathode where they are used to ionize more oxygen. In this way, the process continuously provides a constant supply of oxygen and hydrogen to the fuel cell.

The theoretical density of the materials of the anode, cathode, and electrolyte are used to calculate the porosity of the materials, a critical parameter in determining if the fuel cell will function properly. The anode and cathode must both have a reasonably high porosity (about 30%) to allow gas to diffuse through them to the electrolyte. On the other hand, the electrolyte must be fully dense to prevent the diffusion of air through it, because only oxygen ions and electrons must be allowed to diffuse between the anode and cathode if the SOFC is to function properly. These theoretical densities are calculated from the relative proportions of the atoms present in the material, as indicated by the chemical formula, their atomic masses, the known chemical structure, and the lattice parameters of the unit cell. The lattice parameters of a material were determined from X-ray diffraction (XRD) patterns of the compounds of interest presented in Figure 2. A Scintag XDS 2000 diffractometer was used to collect the diffraction patters from a 2θ range of 20-80° with a step size of 0.03° and a collection time of 12 s.

Though the procedure for calculating the theoretical density is rather straightforward, several papers

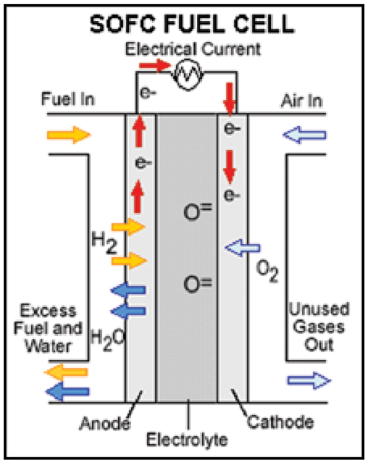

Figure 1. Schematic presentation of solid oxide fuel cell.[2]

have incorrect or conflicting values for different compounds. The methodology can also be somewhat more complicated for researchers lacking a background in chemistry or materials science and engineering. For this reason, this guide has been written. While the materials of focus in this paper are those of interest for SOFCs, the same methodology can be applied to calculate the theoretical density of almost any compound.

2. Ceramic Oxide Crystal Structures

2.1. Perovskite Structure

Perovskites are materials with a chemical formula of ABO_3. The basic crystal structure is cubic, with one A cation at the center and a B cation at each corner of the cube. The oxygen anions are located at the center of each cube edge as shown in Figure 3. Materials used in SOFCs typically have substitutions of some of the atoms at the A site, the B site, or both. For example, if the A site is a La ion, 5% of these ions may be replaced by Sr^{2+} ions. In addition, there can be deficiencies at some of the sites, meaning that some of the sites are vacant and the ratio of the elements present is not exactly 1:1:3. Furthermore, many perovskites have distorted unit cells, that is, rather than being cubic, they may be rhombohedral or orthorhombic.

2.2. Fluorite Structure

Another material type of interest in SOFCs is the fluorite structure, which has a chemical formula of AO_2. The crystal structure shown in Figure 4 consists of cubes with B anions at each corner and A cations at the center of every other cube. A unit cell contains four sets of cube pairs, with each pair containing one cube with an A cation and one without. Another way of considering the structure is as an FCC arrangement lattice of anions with the cations occupying the tetrahedral sites, leaving the octahedral sites unoccupied. As with the perovskites, substitutions and deficiencies are often used in fluorites of interest to SOFCs.

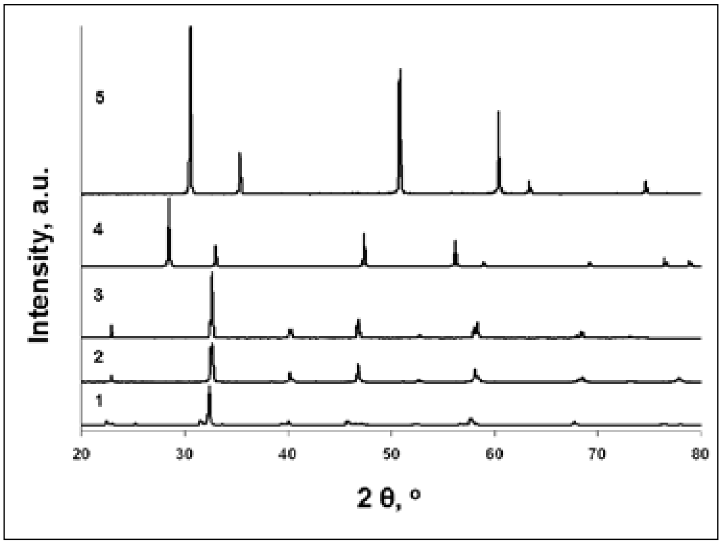

Figure 2. XRD scans of perovskite and fluorite structures used for calculating lattice parameters 1) $LaMnO_3$; 2) $La_{0.6}Sr_{0.4}Fe_{0.8}Co_{0.2}O_3$; 3) $(La_{0.9}Sr_{0.1})_{0.95}Cr_{0.85}Mg_{0.1}Ni_{0.05}O_3$; 4) 20 mol % Gd_2O_3 + 80 mol % CeO_2; 5) 10.07 mole % Sc_2O_3 + 0.92 mole % HfO_2 + 1.03 mole % CeO_2 + 1.4 mole % TiO_2 + 86.58 mole % ZrO_2

2.3. Rock Salt Structure

A third structure considered is rock salt, which has a chemical formula of AO. The A and O ions are located at the corners of simple cubes, with adjacent cubes formed as mirror images of one another as displayed in Figure 5. In other words, the A and B ions alternate in their location in the lattice. As is the case with the fluorites, it takes four cube pairs to form a unit cell.

3. Theoretical Density Calculation

3.1. Examples of Calculations of Perovskites

a) $(La_{0.9}Sr_{0.1})_{0.95}Cr_{0.85}Mg_{0.1}Ni_{0.05}O_3$ (LSCMN)

The chemical formula of the perovskite $(La_{0.9}Sr_{0.1})_{0.95}Cr_{0.85}Mg_{0.1}Ni_{0.05}O_3$ indicates that the basic structure of the material is $LaCrO_3$, where A = La and B = Cr, but 10% of the La atoms are substituted by Sr atoms, 10% of the Cr atoms are substituted by Mg atoms, and 5% of the Cr atoms are substituted by Ni atoms. In addition, 5% of the unit cells will have neither a La atom nor a Sr atom; that is, there is a 5% deficiency at the perovskite A site. It is necessary to calculate the average mass of a unit cell, but first the formula mass is calculated using the masses

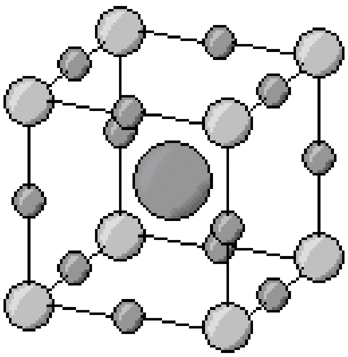

Figure 3. A schematic presentation of perovskite structure

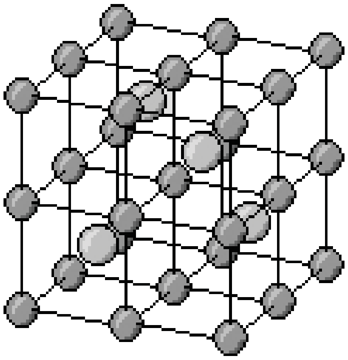

Figure 4. A schematic presentation of fluorite structure

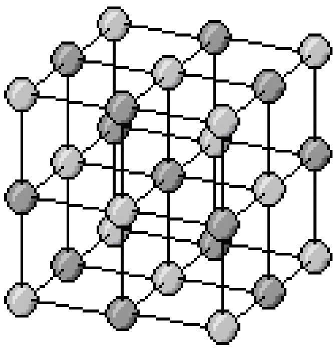

Figure 5. A schematic presentation of rock salt structure

referenced in Table 1 and the subscripts of the chemical formula.

From the chemical formula, 90% of 95% of A sites, or 85.5% of sites, contain and La ion and similarly 9.5% are occupied by a Sr ion, and 5% contain no ion at the perovskite A site; thus, the average mass of the A site will be

$$0.855*138.91 + 0.095*87.62 + 0.05*0 = 127.0920 \text{ amu} \quad (1)$$

Using the same principles for the B site and O ions, the total formula mass is

$$0.855*138.91 + 0.095*87.62 + 0.85*51.996 + 0.1*24.312 + 0.05*58.71 + 3*15.999 = 224.652 \text{ amu} \quad (2)$$

Since 1 amu = $1.6605*10^{-24}$ g, the formula mass is then $3.7304*10^{-22}$ grams.

The unit cells of this structure are orthorhombically distorted. From XRD analysis, a = 5.46 Å, b = 7.75 Å, and c = 5.51 Å, so the volume of the orthorhombic unit crystal is simply a*b*c, which equals 233.15 Å^3, or $233.15*10^{-24}$ cm^3.

Density is simply mass divided by volume. Because of the orthorhombic structure, there are four formula units in each unit cell, which requires the formula mass to be multiplied by four in calculating the theoretical density. The density is then

$$\rho_{LSCMN} = (4*3.7304*10^{-22} \text{ g})/(233.15*10^{-24} \text{ cm}^3) = 6.40 \text{ g/cm}^3 \quad (3)$$

b) $LaMnO_3$ (LM)

$LaMnO_3$ is another perovskite with orthorhombic distortion; therefire, the formula mass must again be multiplied by four to calculate the proper density. There are no substitutions of the ions at the A or B sites for this material, so we simply add the atomic masses of La, Mn, and three times O to determine a formula mass of 241.857 amu, $4.016*10^{-22}$ g. Lattice parameters from XRD analysis are a = 5.70 Å, b = 7.72 Å, and c = 5.54 Å. Using these parameters, the volume of the unit cell is $2.4378*10^{-22}$ cm^3. The density is then,

$$\rho_{LM} = (4*4.016*10^{-22} \text{ g})/(2.44*10^{-22} \text{ cm}^3) = 6.59 \text{ g/cm}^3 \quad (4)$$

c) $La_{0.6}Sr_{0.4}Fe_{0.8}Co_{0.2}O_3$ (LSFC)

An example of a perovskite with rhombohedral distortion is $La_{0.6}Sr_{0.4}Fe_{0.8}Co_{0.2}O_3$. However, the lattice parameters and volume determined for the unit cell are for a hexagonally shaped unit cell. There are two formula units in a rhombohedra, and three rhombohedra to a hexagonal unit cell. As a result, the formula mass must be multiplied by six to calculate the proper mass of the unit cell. So while the formula mass is then 222.855 amu, or $3.7006*10^{-22}$ grams, the average mass of the unit cells is $2.2204*10^{-21}$ grams. The volume is more difficult to calculate from the lattice parameters, because the angles of the unit cell are not right angles, but the XRD software can also calculate volume and in this case determined the volume to be $3.49x10^{-22}$ cm^3. Thus the calculated theoretical density for this material is

$$\rho_{LSFC} = (2.2204*20^{-21} \text{g})/(3.49*10^{-22} \text{ cm}^3) = 6.36 \text{ g/cm}^3 \quad (5)$$

Table 1. Atomic masses for all discussed materials

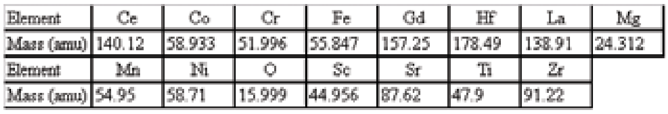

Element	Ce	Co	Cr	Fe	Gd	Hf	La	Mg
Mass (amu)	140.12	58.933	51.996	55.847	157.25	178.49	138.91	24.312
Element	Mn	Ni	O	Sc	Sr	Ti	Zr	
Mass (amu)	54.95	58.71	15.999	44.956	87.62	47.9	91.22	

3.2. Examples of Calculations of Fluorite

a) 10.07 mole % Sc_2O_3 + 0.92 mole % HfO_2 + 1.03 mole % CeO_2 + 1.4 mole % TiO_2 + 86.58 mole % ZrO_2

There is a solid solution of Sc_2O_3, HfO_2, CeO_2, and TiO_2 in the ZrO_2 lattice. The calculation of the density of this solid solution is more difficult than the previous calculations because the chemical formula must be determined before the formula mass can be calculated. ZrO_2, which forms the matrix of this solid solution, is a fluorite, so final formula should be of the form AO_2, though the ratio will not be exactly 1:2. This is because of the 3:2 anion to cation ratio for Sc_2O_3, as opposed to the 2:1 ratio for the other oxides, which results in an oxygen deficiency. One mole of the solution is made from 10.07 mol% Sc_2O_3, 0.92 mol% HfO_2, 1.03 mol% CeO_2, 1.4 mol% TiO_2, and 86.58 mol% ZrO_2. Due to the aforementioned ratio, in one mole of the solution there are actually 0.2014 moles of Sc for every 0.0092 moles of Hf ions, 0.0103 moles of Ce ions, 0.0140 moles of Ti ions, and 0.8658 moles of Zr ions present. Likewise there are 0.3021 mol + 0.0184 mol + 0.0206 mol + 0.0280 mol + 1.7316 mol = 2.1007 moles of O ions.

Taking these numbers as they are, the formula for the solution would be $Ce_{0.0103}Hf_{0.0092}Sc_{0.2014}Ti_{0.0140}Zr_{0.8658}O_{2.1007}$. However, the formula should be of the form AO_2, as this simplifies density calculations due to the fact that there are four AO_2 formula units in each unit cell. To conform to this the fractions of the atoms at the A site must be normalized to 1 using the sum of all the subscripts at the A site, which equals 1.1007. Instead of $Ce_{0.0103}Hf_{0.0092}Sc_{0.2014}Ti_{0.014}Zr_{0.8658}$, the subscripts become 0.0103/1.1007 = 0.0094, 0.0092/1.1007 = 0.0084, 0.2014/1.1007 = 0.1830, 0.0140/1.1007 = 0.0127, and 0.8658/1.1007 = .7866. The subscript of $O_{2.1007}$ must also be adjusted accordingly to 2.1007/1.1007 = 1.9085, yielding the formula of the second solution as $Ce_{0.0094}Hf_{0.0084}Sc_{0.1830}Ti_{0.0127}Zr_{0.7866}O_{1.9085}$ (CHSTZ) as the chemistry for the solid solution. The mass of this chemical formula is 113.939 amu. The average mass of a unit cell is thus 455.758 amu, or $7.5680*10^{-22}$ grams.

If the calculated lattice parameter is a = 5.09 Å, or $5.09*10^{-8}$ cm, the theoretical density is then

$$\rho_{CHSTZ} = 7.5680*10^{-22}/(5.09*10^{-8} \text{ cm})^3) = 5.74 \text{ g/cm}^3 \quad (6)$$

b) 20 mol % Gd_2O_3 + 80 mol % CeO_2

The procedure for this example is very similar to that of the previous example, though somewhat simpler. One mole of the solution will contain .40 moles of Gd ions, .80 moles of Ce ions, and 2.20 moles of O ions, for a chemical formula of $Ce_{0.80}Gd_{0.40}O_{2.20}$ which, when normalized to a ratio of 1:2, becomes $Ce_{0.667}Gd_{0.333}O_{1.833}$ (CG).

The formula mass is then equal to 175.161 amu, which is $2.9086*10^{-22}$ grams. One unit cell, therefore, has an atomic mass of $1.1635*10^{-21}$ grams. The lattice parameter, as determined by XRD, is equal to 5.424 Å or $5.424*10^{-8}$ cm. The density is then

$$\rho_{CG} = 1.1635*10^{-21}/(5.424*10^{-8})^3 = 7.29 \text{ g/cm}^3 \tag{7}$$

Example of Calculation of Rock Salt

This is the simplest of the densities to calculate. The atomic mass of Ni is 58.71 amu and that of O is 15.999 amu, so the mass of the chemical formula is 74.709 amu. Since the mass of a unit cell is 4 times that of the chemical formula, the mass of a unit cell is equal to 298.836 amu, or $4.9623*10^{-22}$ grams. The lattice parameter of NiO is equal to 4.176.[4] The density then is simply

$$\rho_{NiO} = 4.9623*10^{-22}/(4.176*10^{-8} \text{ cm})^3 = 6.81 \text{ g/cm}^3 \tag{8}$$

4. Conclusions

The theoretical densities of important materials can be calculated if the structures of the materials are known and the lattice parameters determined using XRD analysis. In some cases, the chemical formula of the material must also be calculated. Three structures of interest in the study of SOFCs are perovskites, fluorites, and NiO, which has the rock salt structure. The theoretical densities of the perovskites $(La_{0.9}Sr_{0.1})_{0.95}Cr_{0.85}Mg_{0.1}Ni_{0.05}O_3$, $LaMnO_3$, and $La_{0.6}Sr_{0.4}Fe_{0.8}Co_{0.2}O_3$ were calculated to be 6.40 g/cm^3, 6.59 g/cm^3, and 6.36 g/cm^3 respectively. Those of the fluorites $Ce_{0.0094}Hf_{0.0084}Sc_{0.1830}Ti_{0.0127}Zr_{0.7866}O_{1.9085}$ and $Ce_{0.667}Gd_{0.333}O_{1.833}$ were found to be 5.74 g/cm^3 and 7.29 g/cm^3, respectively. Finally, the theoretical density of NiO was calculated as 6.81 g/cm^3.

Acknowledgements

This work done at Michigan Tech under the supervision of Dr. Nina Orlovskaya in her Materials for Energy Laboratory and was funded by NSF DMR project "NSF-Europe Materials Collaboration: Self-organized Nanostructured Thin Films for Catalysis in Perovskite Related Membrane Reactors" 0502765. Rachel Rosten's summer work was funded by a Michigan Tech Summer Undergraduate Research Fellowship (SURF). Matt Koski and Eric Koppana's summer work was funded by the Research and Engineering Apprenticeship Program of the Academy of Applied Science and the Army Research Office.

References

[1] Adler, S.B. Fuel Cells: Current Status and Future Challenges. 2005. *The Bridge*, **2005**, *35*(4), 28-32.
[2] U.S. Department of Energy. Types of Fuel Cells, Solid Oxide Fuel Cells. 04/26/06 http://www.eere.energy.gov/hydrogenandfuelcells/fuelcells/fc_types.html (accessed 7/11/06)
[3] Singhal, S.C. Solid Oxide Fuel Cells for Stationary, Mobile, and Military Applications, *Solid State Ionics*. **2002**, 152-153, 405.
[4] International Centre for Diffraction Data ICDD Card Number 75-0269

About the Authors

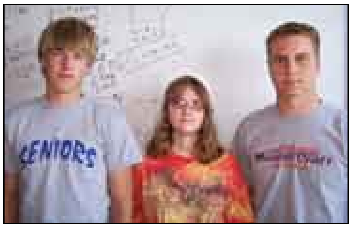

(L-R) Matt Koski, Rachel Rosten and Eric Koppana

Rachel Rosten

Rachel Rosten is a senior at Michigan Technological University pursuing a degree in Materials Science and Engineering as well as Physics with a 4.0 GPA. She is a recipient of the Provost's Award for Scholarship, the highest award for scholarship awarded to seniors at MTU. Rachel began work on the NSF project in January 2006 and has been focusing on the characterization of materials that are candidates for oxygen permeability membranes. n addition she tutors in both the Math Learning Center and the Physics Learning Center, where she helps students with difficulties in undergraduate math and physics courses.

Matt Koski

Matt Koski recently graduated from L'Anse High School (L'Anse, Michigan) with a 4.0 GPA and was the valedictorian of his class. He will be a freshman at Michigan Technological University in September of 2006. Matt chose to attend Michigan Technological University because it is nationally ranked for engineering and is close to home. This summer, Matt worked in the Materials Science and Engineering Department at Michigan Tech under the Engineering Apprenticeship Program helping with research work focusing on fuel cells.

Eric Koppana

Eric Koppana is a recent graduate of Calumet High School (Michigan) with a 3.7 GPA. He will be a freshman at Michigan Technological University in the fall of 2006. His interest in engineering brought him to Michigan Tech, one of the top universities in the state. Eric was given the opportunity to work in the Materials Science and Engineering Department doing mostly fuel cell materials research in a program called the Research and Engineering Apprenticeship Program. This program is supported by the Academy of Applied Science.

Tunable Three-Dimensional Magnetic Coordination Polymers

Joseph M. Zadrozny

Virginia Polytechnic Institute and State University, Department of Chemistry
Blacksburg, VA 24061

Abstract

Four chlorinated phenyltricyanoethylenes were synthesized and reacted with vanadium hexacarbonyl to form ferrimagnetic coordination polymers. Species chlorinated at the 2, 3, or 4 position of the ring as well as a dichlorinated analogue with substitution at both the 2 and 6 positions were examined. The magnetic ordering temperatures of the polymers were reproducible and ranged from 140 to 288 K. All compounds displayed soft ferrimagnetic behavior, and their structure-property relationships are discussed.

Keywords: Magnetic coordination polymers, phenyltricyanoethylene, ferrimagnetism

1. Introduction

In 1991, Manriquez and coworkers reported the discovery of the first room temperature molecule-based magnet, prepared from the reaction of vanadium hexacarbonyl and tetracyanoethylene (TCNE).[1] This compound, believed to be a network of V^{2+} bridged by TCNE radical anions, is limited in application due to its rapid decomposition upon exposure to air. A possible source of the air-sensitivity is the V^{2+} ions, as these are highly susceptible to oxidation.[2] Replacing V^{2+} with later transition metal ions such as Mn^{2+} or Fe^{2+} may overcome this limitation, however, such substituted compounds have been found to be non-magnetic at room temperature.[3] Therefore, discovering a replacement for TCNE has become desirable for synthesizing useful, room temperature molecule-based magnets. The goal of this study was to find an acceptor starting material, which when paired with one of these later transition metals, would yield an air-stable, room temperature magnet.

However, as only vanadium was used in this study, it was hoped that a way to maximize the temperature at which the material is magnetic through tuning only the acceptor could be found. Once this was known, different metals could be utilized to find air-insensitive room temperature magnets.

2. Background

2.1 Magnetic Ordering

Given a network of species containing unpaired electrons, there are two general types of magnetic interaction that can lead to long-range magnetic order with a net magnetic moment. One type, termed ferromagnetism, occurs when all of the electron spins are aligned in the same direction. Conversely, antiferromagnetism occurs when adjacent spins in a compound align in opposite directions, effectively canceling each other out and resulting in no net magnetic moment. Ferrimagnetic ordering is similar to antiferromagnetic ordering, only adjacent spins are unequal in magnitude resulting in a net magnetic moment. Figure 1 illustrates ferromagnetic, antiferromagnetic, and ferrimagnetic ordering schematically.

In most compounds, measurements show the net magnetization diminishing at elevated temperatures as enough kinetic energy becomes available to overcome the thermodynamic tendency to align at lower temperatures. This is because increased thermal energy allows electrons to be excited to higher orbitals, which are not necessarily aligned with the applied magnetic field. The temperature below which the moments start ordering is referred to as the Curie temperature (T_c).

2.2 Molecule-based Magnets

Two different types of molecule-based magnet starting materials were used in this project. The first is an easily reduced organic molecule (aka acceptor), that is designed to bridge two

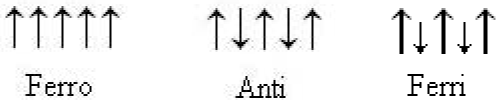

Figure 1. Ferromagnetic, antiferromagnetic and ferrimagnetic coupling systems

or more metal ions upon accepting an electron from each. The second starting material consisted of vanadium atoms (derived from vanadium hexacarbonyl), which contribute electrons to two organic molecules to form the divalent V^{2+} cation in conjunction with the loss of its six carbonyl functional groups. The remaining (three) d-electrons on the cation give rise to local moments which do not completely cancel each other out, resulting in a net magnetic moment. Magnets created in this manner are of technological importance because their magnetic properties can be tuned by varying either of the two starting materials (i.e. using slightly different molecules as the acceptor, or by using different metal ions).

Molecule-based magnets can be advantageous over atom-based magnets. For example, molecule-based magnets can often be synthesized at or near ambient conditions as opposed to their atom-based counterparts, which typically require very high temperatures for formation. In addition, molecule-based magnetic materials often have a higher magnetization per unit mass ratio than atom-based magnets. The cause of this is two fold: first, lighter nonmetal elements are often incorporated into the atomic structures, and second, the molecule-based magnetic compounds tend to have an open-framework type structure as opposed to the dense, tightly packed atomic lattices of atom-based magnets.

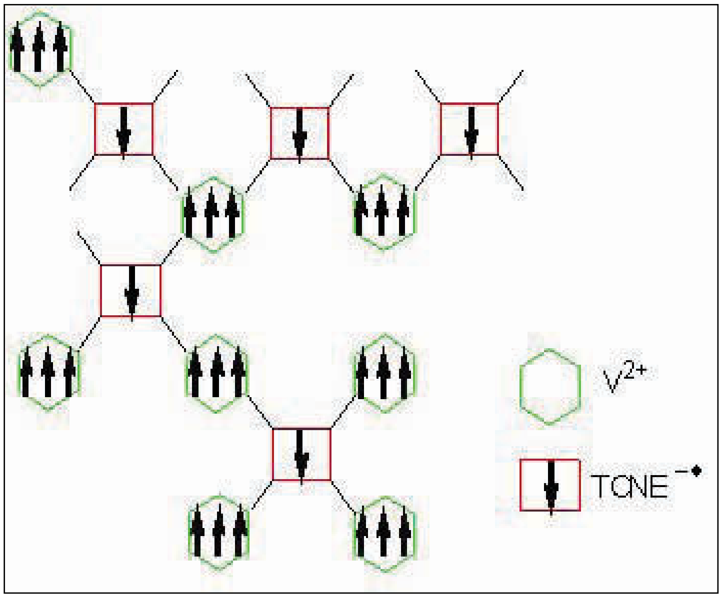

Figure 2. Spin coupling scheme for a $V[TCNE]_x \cdot y[CH_2Cl_2]$ ferrimagnetic polymer

Although these types of compounds are amorphous,[4] the overall stoichiometry for $V[TCNE]_x \cdot y[CH_2Cl_2]$ type materials has been determined to be roughly two electron acceptor molecules for every vanadium ion through elemental analysis ($x \sim 2$).[5] As illustrated in Figure 2, the result is one unpaired electron (a net spin of ½) per formula unit.

This study attempted to determine whether magnets with metals ions other than vanadium could be synthesized which retain the high ordering temperature of vanadium-based magnets, while being immune to decomposition upon exposure to air. To test this hypothesis, the research was conducted with the specific purpose of probing how the electronic structure of the organic bridges connecting the metal atoms affects the ordering temperature. The various organic bridges synthesized for study are shown in Figure 3. These organic bridges are all similar to TCNE but feature a phenyl ring that may be substituted with chlorine to modify the steric (size) and electronic properties of the molecule, which, when reacted, allows for tunability of the synthesized magnets.

3. Procedure

3.1 General Considerations

Magnet synthesis was performed in a chemically inert nitrogen atmosphere, while all other procedures were carried out under ambient conditions. Vanadium hexacarbonyl was synthesized following procedures outlined in the literature.[6]

3.2 Materials

Solvents used for synthesis of the magnetic polymers and electrochemistry were distilled from P_2O_5. All other solvents

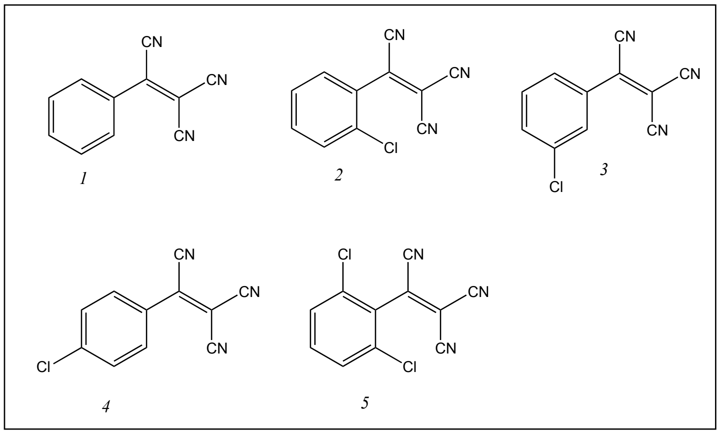

Figure 3. Synthesized electron acceptors

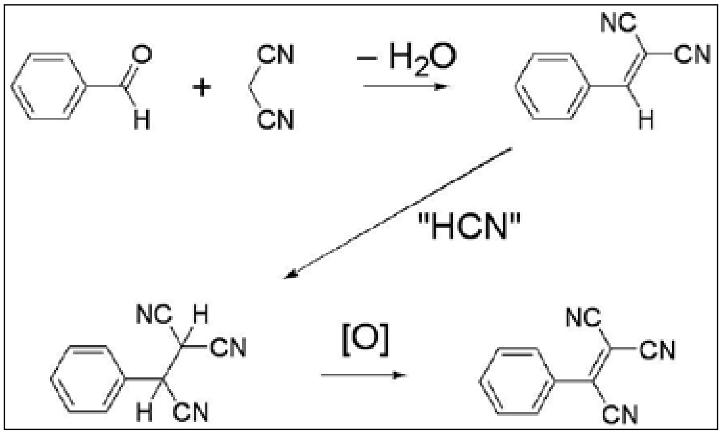

Figure 4. Reaction scheme for electron acceptor synthesis

were used as received. 2-(2-chlorophenyl), 2; 2-(3-chlorophenyl), 3; 2-(4-chlorophenyl), 4; and 2-(2,6-dichlorophenyl)-1,1,2-tricyanoethylene,5 were synthesized in a similar manner to 2-Phenyl-1,1,2-tricyanoethylene,1; as shown in Figure 4.

3.3 Synthesis

2-(2,6-dichlorophenyl)-1,1-dicyanoethylene, [6]

First, 2,6-dichlorobenzaldehyde, 2.27 g (1.3 mmol), was added to 20 mL 100 % ethanol in a 100 mL beaker. Next, 0.874 g of 1.32 mmol malononitrile was added to the ethanol/benzaldehyde solution. Then, three drops of piperidine were added, and the solution was stirred briefly. The solution was then placed in an evaporating dish to remove the solvent. The collected solid was then redissolved in dichloromethane and stirred with decolorizing carbon. The resulting solution was filtered into a separate flask, and the remaining solvent was evaporated using a rotoevaporator.

2-(2,6-dichlorophenyl)-1,1,2-tricyanoethane, [7]

First, 1.76 g (7.55 mmol) of [6] (synthesized as shown above) was added to 200 mL of 100% ethanol in a 250 mL beaker. 1.01 g of 15.3 mmol potassium cyanide was dissolved in 50 mL of deionized water contained in a separate 500 mL beaker. Once both solids had dissolved, the ethanol solution was added to the aqueous solution. Next, 250 mL of deionized water was then added to the aqueous solution to double the solution volume. Then, the reaction vessel was placed in an ice bath for 45 minutes, after which, the vessel was removed from the ice bath and 2 mL of chilled, concentrated hydrochloric acid was added. Next, the solution was stirred briefly, and then the vessel was covered overnight. Finally, the solid formed was collected via vacuum filtration and a buchner funnel.

2-(2,6-dichlorophenyl)-1,1,2-tricyanoethylene, [5]

First, 0.450 g (1.799 mmol) of [7] (synthesized as shown above) was added to a 100 mL of diethylether, while 0.5 g of N-chlorosuccinimide were added to 80 mL of deionized water in a separate 100 mL beaker. Once the solids in both solutions had dissolved, the aqueous solution was added to the ether solution. Next, the resulting mixture was stirred vigorously for 15 min. Then, the ether layer was collected with a separatory funnel and dried with several scoops of anhydrous sodium sulfate. Next, the solution was filtered into a new flask, and the ether was evaporated using a rotoevaporator. The collected solid was then purified by column chromatography using silica gel as the stationary phase and chloroform ($CHCl_3$) as the elutant.

Magnetic Solid, [8]

First, 37.4 mg, 0.171 mmol, of vanadium hexacarbonyl were dissolved in 1 mL degassed dichloromethane (CH_2Cl_2) in a 10 mL sample vial, while 90.8 mg of 0.366 mmol of [5] were added to 2 mL degassed CH_2Cl_2 in a 50 mL round bottom flask. Next, the vanadium solution was added to the acceptor solution by filtering through a coarse glass frit. Then, the vessel was sealed, and the solution stirred with a magnetic stirbar for approximately 30 minutes. Finally, the resulting black solid was then collected by filtering through a medium fritted glass filter and dried in-vacuo for 1 hour.

3.4 Material Characterization

A CH Instruments Model 600A Potentiostat was used for electrochemical analysis. Specimens were prepared with 0.125 mol of a given ethylene solid added to 25 mL of a 0.1 M $[n\text{-}Bu_4N][PF_6]$ solution of acetonitrile. The electrochemical potential of the sample was then scanned from 0 to -800 mV at a rate of 100 mV/s. A polished carbon working electrode was used with a Ag/AgCl reference electrode in a 10 mL glass cell. All magnetic measurements were collected with a Quantum Design MPMS XL Superconducting Quantum Interference Device (SQUID). Curie temperatures of the magnets were found by cooling from 300 to 5 K in a magnetic field of 10 Oe and measuring the magnetization of the sample from 5 to 300 K in 1 K increments. Magnetic hysteresis measurements were performed at 5 K with a scanning range of -100 to 100 Oe in increments of 3 Oe.

Infrared (IR) spectra for the compounds were obtained as potassium bromide (KBr) pellets by adding the compound to powdered KBr. All spectra were obtained in the range of 4000 – 400 cm^{-1} on a MIDAC M-series FTIR spectrometer.

All 1H NMR spectra were acquired in $CDCl_3$ with the use of a Varian Inova400 spectrometer.

4. Results and Discussion

4.1 Synthesis

Table 1 gives the relevant yield and characterization data for the syntheses reported in section 3.3.

Nuclear magnetic resonance (NMR) and IR techniques were chosen as the primary methods for characterizing the products of our reactions. As can be seen for [6], a singlet at 7.95 ppm results from the benzyllic proton and the protons on the aro-

Table 1. Yield and characterization

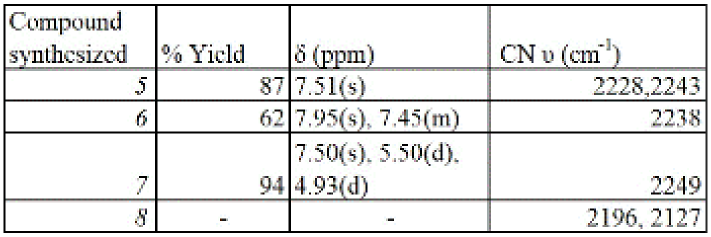

Compound synthesized	% Yield	δ (ppm)	CN υ (cm^{-1})
5	87	7.51(s)	2228,2243
6	62	7.95(s), 7.45(m)	2238
7	94	7.50(s), 5.50(d), 4.93(d)	2249
8	-	-	2196, 2127

matic ring give rise to the multiplet at 7.45 ppm. Analysis of [7] shows no major difference in the chemical shift of the aromatic protons but the introduction of two doublets. These doublets disappear from the spectrum after the reaction with NCS, giving evidence that the Hydrogen atoms are eliminated as a double bond is formed in [5]. Similar behavior was observed in the other acceptors.

NMR analysis of the magnetic solid [8] was not performed due to the insolubility of the polymer. IR spectra give evidence towards the formation of the polymer, as the CN stretch moves to lower wavenumbers, which is presumably from electron donation by the vanadium ions into the antibonding orbitals of the acceptor. The other magnetic polymers synthesized displayed similar behavior.

4.1 Critical Temperature

As can be seen in Figure 5, the T_c is affected by the position of substitution on the arene ring. The unsubstituted acceptor gives a polymer with a T_c near 200 K, while the 2, 3, and 2,6 substituted acceptors gives polymers with T_c's of 240, 260, and 288 K, respectively. Surprisingly, substitution at the 4 position of the phenyl ring results in a magnetic material that orders at a lower temperature than the unsubstituted material. Substitution at the 2 or 3 positions each cause ordering above that of the unsubstituted acceptor, and substitution at both the 2 and 6 positions on the ring gives an enhanced T_c raising effect which leads to a polymer with the highest T_c out of all those studied in this paper. The measurements of the T_c for each of the polymers have been reproducible within ± 5 K.

At first glance, this trend can be rationalized by recognizing the π-electron donating ability of the chlorine atom. It appears that at the 2 and 3 positions on the ring, the σ-withdrawing effect of the chlorine atom is more powerful than the π-donating effect. At the 4 position, however, the donating effect could overcome the withdrawing effect, resulting in a lower measured T_c. By donating electron density into the arene ring, which is already electron rich, communication between the spins of the vanadium ions is lessened, which correlates to a lower ordering temperature. However, electrochemical measurements presented later contradict this approach.

4.2 Magnetic Hysteresis

The coercivity (H_c) is the value of the applied field where the curve crosses the x-axis. The saturation magnetization is the maximum value reached by the magnetization. All compounds exhibited coercivities (that is, the magnitude of the field required to return the magnetization of a material back to zero) between 1 and 5 Oe, with the exception of the polymer made from substitution at the 4 position, which required 11 Oe. Table 2 lists the H_c values as they correspond to each polymer.

All of the compounds are soft magnets by definition, as hard magnetic materials show H_c values in excess of 125 Oe.[6] The measured H_c values stem from the low anisotropy of the vanadium atoms. A system shows small H_c values when the starting metal ion used is essentially isotropic, which is expected for these compounds as the three unpaired electrons from octahedral vanadium would reside in the t_{2g} orbitals.[7]

The saturation magnetization of these compounds also provides insight into their magnetic coupling. One mole of unpaired electrons contributes 5585 emu*G/mol to the magnetization of a material.[8] Therefore, the saturation magnetization for the polymer formed with the 2,6-dichlorinated acceptor should be in excess of 26000 emu*G/mol for ferromagnetic interactions (5 unpaired electrons × 5585 emu*G/mol). If we assume a 2:1 stoichiometric ratio of electron acceptors to vanadium ions, then the saturation magnetization is calculated to be 4923 emu*G/mol, which is closer to the net magnetization resulting from

Table 2. Coercivities

Magnet	H_c (Oe)
Unsubs	1.9
4-Cl	11.4
3-Cl	5.0
2-Cl	2.1
2,6-Cl	4.6

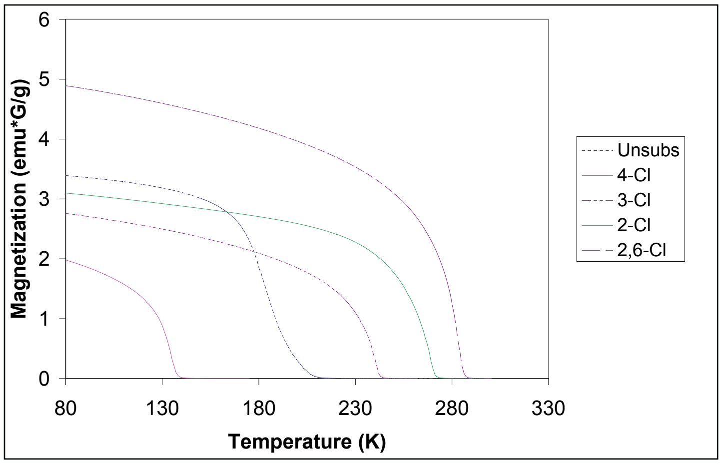

Figure 5. Critical temperature data for the synthesized magnetic polymers

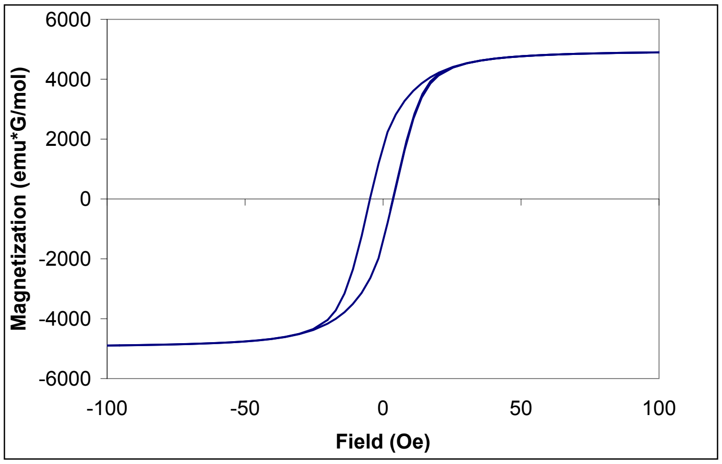

Figure 6. Magnetic hysteresis curve for the 2,6-dichlorotricyanoethylene coordination polymer

one mole of unpaired electrons, indicating that the synthesized compounds are ferrimagnets.

4.3 Cyclic Voltammetry

Table 3 gives important information concerning our electron acceptors. The potentials displayed directly correlate to the voltage output required by the potentiostat to either reduce (shown in the middle column) or oxidize (shown in the far right column) the sample. The middle column shows that reducing the acceptor molecules becomes easier when chlorine is substituted onto the phenyl ring. This contrasts with what is observed for the T_c data, where the T_c of the polymer made with position 4 is lower than that of the polymer made with position 1. This difference between the two data sets suggests that some factor other than simply the electron withdrawing/donating ability of chlorine is affecting the T_c.

Figure 7 shows the cyclic voltammogram of the unsubstituted phenyltricyanoethylene. All of the compounds were shown to be reversible by cyclic voltammetry, which suggests that the bridging electron acceptors are stable upon accepting an electron from the vanadium during synthesis.

5. Conclusions

Changing the position of the halide functional group on the phenyl ring altered the T_c of the synthesized magnet, giving rise to tunability. Substitution at the 4 position of the phenyl ring in phenyltricyanoethylene produced a solid upon reaction with $V(CO)_6$. These solids ordered at lower temperatures than the polymers made with unsubstituted acceptors. Substitution at the 2 and 3 positions yielded polymers with higher T_c than the polymer made with the unsubstituted acceptor. From this data, it appears that the T_c increasing effect from chlorine substitution is additive, as the T_c of the compound created from the disubstituted acceptor was higher than for any of the other compounds, which means that a potential pathway towards reaching a maximum T_c has been found for this class of compounds. Further studies would allow us to explore this route and hopefully arrive at higher T_c magnetic materials than were reported here.

The magnetic polymers synthesized were found to be air sensitive. The limited applications for air-sensitive molecule-based magnets warrant future work to synthesize polymers using other non-vanadium first row transition metals. In addition, synthesizing magnets made from poly-substituted acceptors may hold promise for improved room-temperature magnets. If the T_c increasing effects of chlorine substitution are truly additive, synthesizing a magnet with 2, 3, 5, 6-tetrachlorinated phenyltricyanoethylene would display the highest possible T_c for this class of magnetic compounds.

Table 3. Oxidation and reduction peak potentials. All potentials given are versus an Ag/AgCl reference electrode

Sample	$E_{p,red}$ (V)	$E_{p, ox}$ (V)
Unsubs	-0.44	-0.36
2,6-Cl	-0.34	-0.28
2-Cl	-0.39	-0.33
3-Cl	-0.34	-0.27
4-Cl	-0.38	-0.31

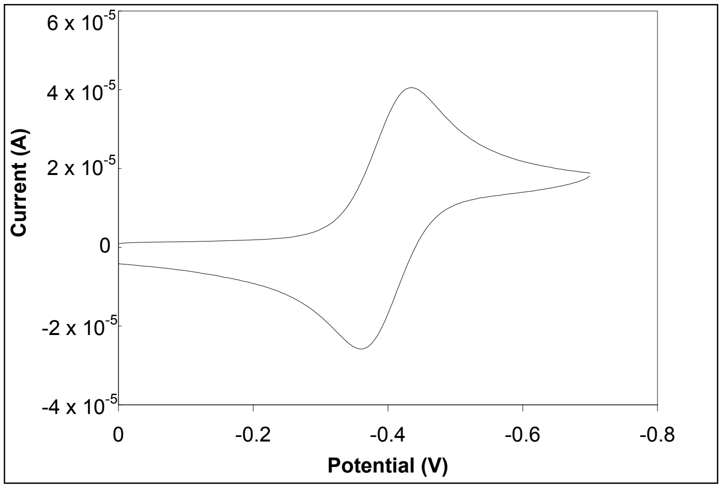

Figure 7. Cyclic Voltammogram of the unsubstituted phenyltricyanoethylene

Acknowledgements

We thank Virginia Tech Analytical Services for the use of their FTIR and NMR equipment, Professor Mark Anderson for the use of the CH Instruments potentiostat, Mark Harvey for the supply of vanadium hexacarbonyl, and the Petroleum Research Fund administered by the American Research Fund for funding this reserach. This research was performed under the direction of Professor Gordon Yee.

References

[1] Manriquez, J. M.; Yee, G. T.; McLean, R. S.; Epstein, A. J.; Miller, J. S. A room-temperature molecular/organic-based magnet. *Science* **1991**, *252*, 1415.

[2] Zhang, J.; Ensling, J.; Ksenofontov, V.; Gutlich, P.; Epstein, A. J.; Miller, J. S. [MII(TCNE)$_2$]×xCH$_2$Cl$_2$ (M = Mn, Fe, Co, Ni) molecule-based magnets with Tc values above 100 K and coercive fields up to 6500 Oe. Angewandte Chemie International Edition **1998**, *37*(5), 657-660.

[3] McQuaid, M.J.; Gole, James L. The effect of carbonyl complexation on highly exothermic vanadium oxidation reactions. Chemical Physics **2000**, *260*, 367-382.

[4] Vickers, Elaine B.; Senesi, Andrew; Miller, Joel S. Ni[TCNE]$_2$•zCH$_2$Cl$_2$ (Tc = 13 K) and V$_x$Ni$_{1-x}$[TCNE]y•zCH$_2$Cl$_2$ solid solution room temperature magnets. *Inorganica Chemica Acta* **2004**, *357*, 3889-3894.

[5] Kaul, B. B.; Yee, G. T. Two new acceptor building blocks for 'high Tc' coordination polymer magnets. *Inorganica Chemica Acta* **2001**, *326*, 9-12.

[6] Jiles, D. Chapter 4. *Introduction to Magnetism and Magnetic Materials*. Chapman & Hall: London, 1991.

[7] Haskel, D.; Islam, Z.; Lang, J.; Kmety, C.; Srajer, G.; Pokhodnya, K. I.; Epstein, A. J.; Miller, J. S. Local structural order in the disordered vanadium tetracyanoethylene room-temperature molecule-based magnet. *Physical Review B* **2004**, *70*(5), 054422.

[8] Torre, Edward D. Chapter 1. *Magnetic Hysteresis*. Institute of Electrical and Electronics Engineers, Inc.: New York, 1999.

About the Author

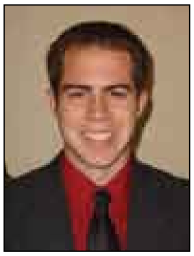

Joseph M. Zadrozny

Joe Zadrozny is a fifth year undergraduate at Virginia Tech. His major is chemistry and he is currently completing a minor in mathematics. After he finishes this year, he will be going to graduate school. His current top choice schools are mostly on the west coast where the weather is consistently great (note: he is not even considering going anywhere near Seattle). He enjoys reading and cycling in his spare time, and sometimes he has even been known to fold origami.

Simulation of Damage in Human Cortical Bone with Nonlinear Finite Element Analysis in MATLAB

Steven F. Kemeny

Virginia Polytechnic Institute and State University, Department of Engineering Science and Mechanics
Blacksburg, VA 24061

Abstract

This paper examines bone fatigue damage using Finite Element Analysis (FEA) to predict changes in modulus, damage and cycles to failure. The MATLAB-coded material model has been previously implemented in a full FEA package. It is based on published models of damage verified with experimental data. The MATLAB program inputs a finite element mesh and simulates the damage iteratively. Four meshes are examined: a machined tensile specimen of the bone, a machined bending specimen, a single strut of cancellous bone, and a 2-D slice of cancellous bone. This model is a fast testing method for ideas, allows easy comparison of different test geometries and material damage models, and may help to bring the study of bone damage to a broader audience.

Keywords: Bone mechanics, fatigue damage, finite element analysis

1. Introduction

Accurate bone damage simulation can lead to better prediction of bone life, which can be used in prosthetic design and may aid clinical studies of disease such as osteoporosis. A number of in vitro fatigue studies have been performed, establishing phenomenological models. One such model relates damage rate per cycle, to the “normalized stress” (stress divided by initial modulus) applied in cyclic loading.[1]

Finite element analysis is widespread in stress analysis of bone-implant systems. It allows complex shapes to be input to determine stresses, strains, and displacements. Earlier studies have incorporated damage models in fatigue FE studies of bone using MSC.Marc and user defined subroutines in FORTRAN.[2] This technique was powerful, but requires in-depth knowledge of expensive specialized software and limits the user to the corporate software designer. MATLAB is widely used at universities and elsewhere in the engineering community. The goal of this work is to implement the Cotton damage law into MATLAB and demonstrate its utility to simulate various 2-D bone structures. Modeling damage with MATLAB can bring the study of bone damage to a larger population.

2. Procedure

2.1 Making the Meshes

First, the two-dimension finite element meshes were created in the finite element analysis package Marc (MSC Software, Santa Ana, CA, USA). There were four different meshes created: a tensile specimen, a bending specimen, a cancellous bone strut, and a slice of trabecular bone (Figure 1). The tensile and bending specimens are modeled after fatigue tests specimens used by Zioupos.[3] The cancellous strut assumes symmetry and homo-

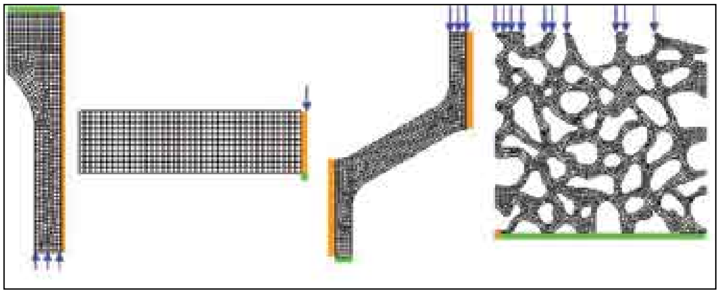

Figure 1. Finite element meshes of all four structures. From left to right, the tensile specimen (divided into a quarter of the structure for symmetry), the bend test specimen (divided in half for symmetry), the cancellous strut, and the cancellous slice. Green bars represent vertical axis constraints, orange bars represent horizontal constraints. Blue arrows represent the applied load.

geneity of a regular hexagonal cellular solid, and was presented earlier by Cotton.[4] The cancellous slice has been previously modeled by Taylor.[2] The finished geometric mesh of nodes and elements were imported into MATLAB and converted into an input structure designed for the model. Material properties, nodal constraints, and loads were added to the input structure. For all models, Young's modulus of the bone tissue was taken as 15 GPa, Poisson's ratio of 0.35. Loads were applied such that peak stresses were on the order of 30 to 150 MPa.

2.2 Static Testing of the Meshes

All four meshes were simulated statically with a finite element analysis function modified from Zaicenco.[5] Our modifications included redesigning the data into a hierarchical structure. The FE function took the input structure and solved for the stresses and displacements in the mesh. The original graphical output was modified to better examine the stress tensors and nodal displacements. Results were tested and compared to calculated static results for verification for the tensile and beam meshes.

2.3 Modeling the Damage Laws

The damage laws were coded in MATLAB functions and were applied at each cycle and repeated until the sample "broke", defined as a stiffness reduction of 90%. The damage law[1] defined the damage rate, ΔD/ΔN, as a function of "normalized stress," σ/E*, by using a power law expression

$$\frac{\Delta D}{\Delta N} = A\left(\frac{s}{E^*}\right)^B \qquad (1)$$

where A and B where constants fit to experimental data, E* was the initial modulus and σ was the major (maximum magnitude) principle stress at the node. The use of normalized stress is widespread in bone mechanics, and allows for accurate extrapolation of material laws to bone of greatly different types. The damage, D(n), at cycle n, is defined as the fractional loss of stiffness

$$D(n) = 1 - \frac{E(n)}{E^*} \qquad (2)$$

where E(n) is the modulus. The constants A and B were 1035.5 and 17, respectively. As these tests were in tension, values needed to be adjusted to represent compression. Compressive tests of bone show fatigue failure strengths and damage rates of roughly 50% of the respectively tensile results.[6] The elements were adjusted whose major principle stress was negative, by multiplying the stress factor inserted into Equation (1) by 0.69.

This model was run in MATLAB through a number of loading cycles. For each cycle, the FEA was used to determine stresses then the values were inserted into the damage law routines. The process was automated to repeat cyclically until the specimen failed.

2.4 Simulations Run

The tensile specimen was run through a simulation from zero to maximum tension (0-T) fatigue tests of different load magnitudes to verify accuracy. Stress versus cycles to failure (S-N) curves were generated and compared to published data. Bending, strut and cancellous samples were run to observe the effects of fatigue on these structures.

3. Results and Discussion

3.1 Static Testing of the Meshes

The four meshes created are presented, along with loads and constraints, in Figure 1. In a static analysis they all showed stresses and displacements predicted by analytic calculation (for tensile and beam), or that were consistent with earlier FE studies (strut and slice).

3.2 Modeling the Damage Laws

The damage function was first tested with the tensile mesh. The mesh was cyclically loaded with a constant maximum load. With each cycle, the damage accumulated until failure. The damage increase is shown in Figure 2. As this figure shows, in the areas that damage quickly in the start of the simulation, damage levels out with more cycles. This figure also shows uniform damage in the mesh within the gage length. This uniform damage level becomes the largest in the model only after approximately 100 cycles. The simulated specimen life gave an

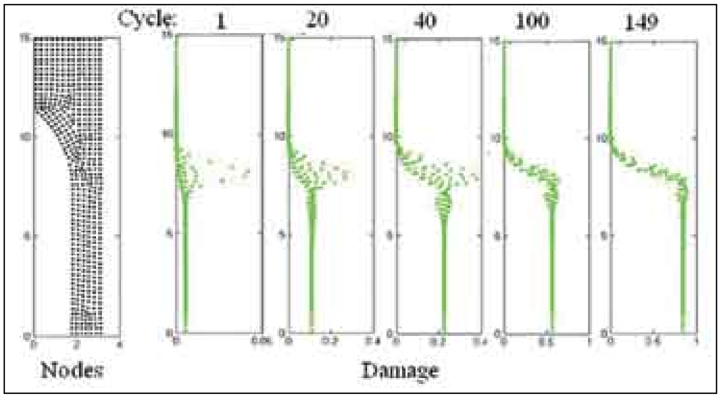

Figure 2. This is the damage through the height of the tensile specimen at different cycles during the fatigue simulation. The plot to the far left shows the element midpoints where the damage is calculated. A test was run with a normalized applied load of 6021 με (or nondimensional strain times 106). This test failed at 150 cycles.

error between 5 and 20% of the predicted life values from the published formula as shown in Figure 3. The error in damage levels are also plotted in Figure 4. As the number of cycles to failure decrease, the error increases. This is explained by the peak stresses in the shoulder of the sample seen in early cycles of Figure 2. With lower stresses and higher cycles to failure, these peak stresses and high damage areas smooth out and failure occurs in the gage length as the test is designed to do.

3.3 Other Models

Other models were also used to simulate fatigue damage in the beam, the bending specimen, strut and cancellous slice models. All models showed localized damage conforming to the location of maximum stress.

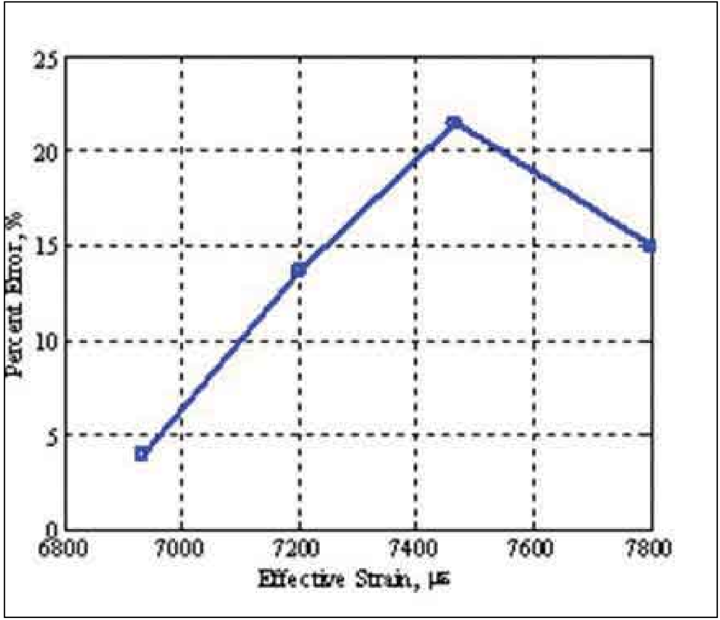

Figure 3. Error of the cycles to failure and damage

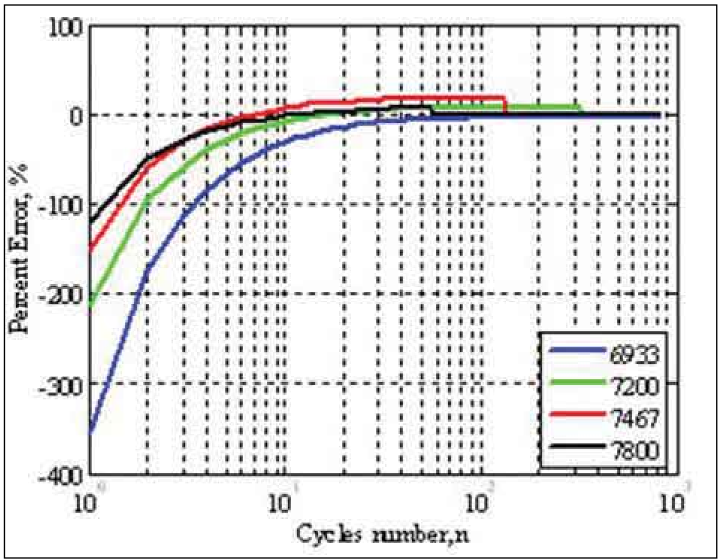

Figure 4. Error of the apparent strain for the tensile model showing agreement with calculated results with lower applied normalized stress.

The beam was run with an applied load of 7.8 N, which resulted in a maximum initial strain of 5800 με in compression. The sample failed on the lower tensile surface at 2.25 million cycles. This is a much higher life than predicted by the tensile laws, due to the sample's outer surface damaging, dropping peak stresses there and raising stresses into the depth. These results are consistent with bending fatigue tests of bone, in that they fail in tension despite the additional compressive load from the

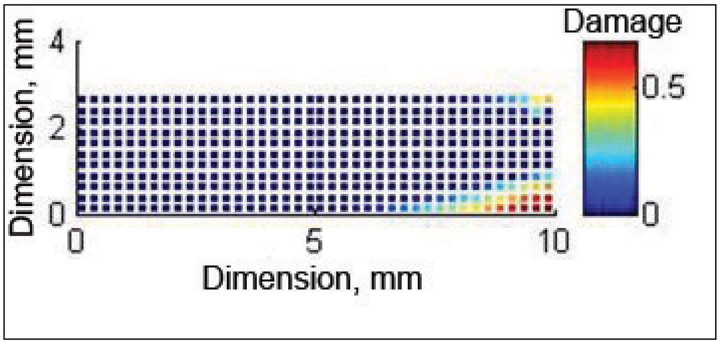

Figure 5. Damage in the beam specimen during the fatigue test. The bottom tensile surface shows greater damage than the top compressive surface. Damage is highest mid-span (right side of FE model) where the bending moment is highest.

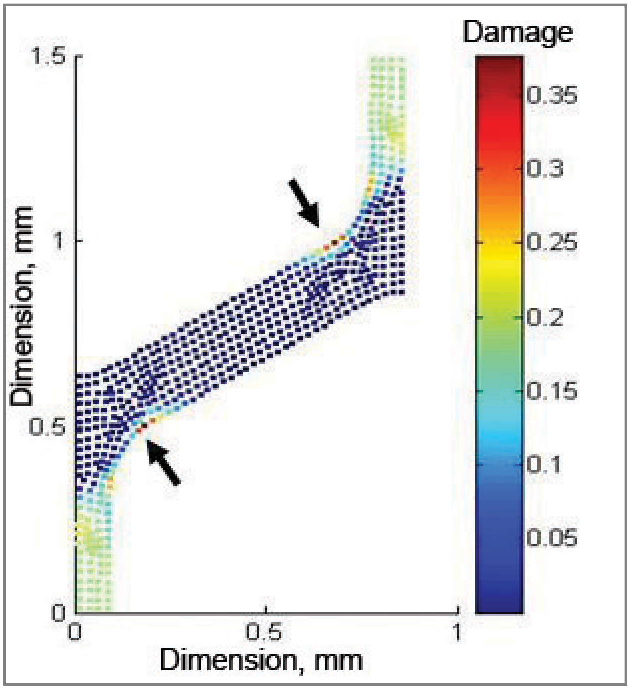

Figure 6. Damage in the cancellous strut during the fatigue test. Damage is highest near the arrows where the compression from the vertical section adds to the compression from bending in the horizontal trabeculae. Tension on the bottom surface is small enough not to damage noticeably

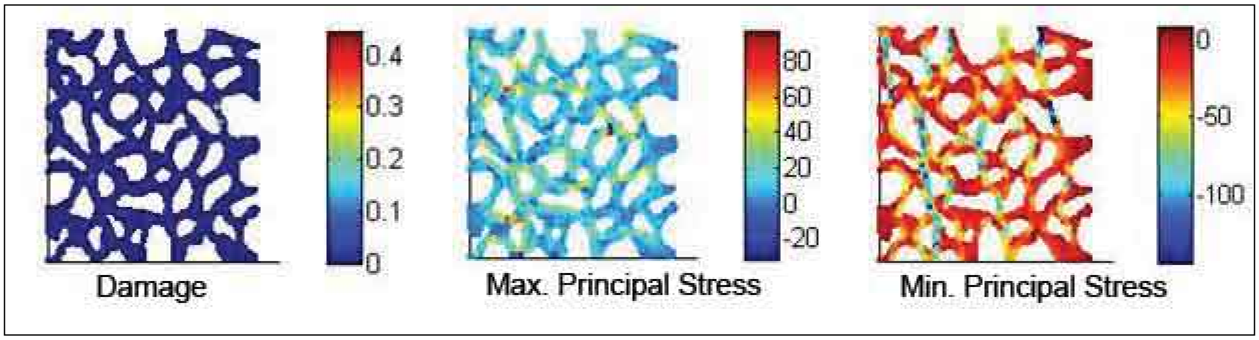

Figure 7. Damage in the cancellous slice during the fatigue test. Maximum and minimum principle stresses are shown. Typical of cancellous bone, although the slice has an apparent stress of only 6.3 MPa, local areas experience stresses in excess of 10 times greater. This leads to localized damage in high stress areas.

load on top surface. It is worth noting that choosing a different definition of failure results in grossly different definitions of life, for example the 20% loss of stiffness used elsewhere would lead to a simulated life of 180,000 cycles. Damage distribution in the beam at 150,000 cycles is presented in Figure 5.

The strut was run with an apparent stress (net load divided by cross sectional area) of 7.39 MPa, which resulted in a maximum initial strain of 7441 με in compression. The sample failed in compression at 29,000 cycles. These results differed from the work of the previous simulations where tensile failure in bending occurred.[3] This is because this simulation constrained the strut model on both horizontal limits. Damage distribution in the strut during the test is presented in Figure 6.

The cancellous slice was run with an apparent stress (net force divided by whole cross sectional area) of 6.3 MPa, which resulted in a maximum initial strain of 11800 με in compression. Damage distribution in the slice at 379 cycles, is presented in Figure 7. It can be seen that only a few select areas experience any damage. Although these elements may have damage of 45% at this point, the entire structure has shown negligible loss of stiffness (< 0.1%). This is consistent with earlier FE studies.

4. Conclusions

Bone damage simulation was performed in MATLAB, a widely used software in the science community. This simulation is more accessible and adaptable than typical FEA packages. The model is accurate with its predictions of the damage, modulus change, and cycles to failure. In the future, other damage laws[7,8] could be added to the model and many different specimens configurations could be tested. This tool will readily allow both cross-comparison of different damage laws and interpretation of differences in test geometries and configurations, helping to broaden our understanding of bone damage.

Acknowledgements

John Cotton, Assistant Professor in Engineering Science and Mechanics at Virginia Tech, advised Mr. Kemeny with this project as an independent study and provided various modifications to the downloaded FE code. Frances Davis, a senior undergraduate in ESM at Virginia Tech, also worked on the FE code for a separate project and provided useful modifications of several of the graphics routines used.

References

[1] Cotton, J. R.; Winwood, K.; Zioupos, P.; Taylor M. Damage Rate is a Predictor of Fatigue Life and Creep Strain Rate in Tensile Fatigue of Human Cortical Bone Samples, *Journal of Biomechanics*, **2005**, *127*(2), 213-9.

[2] Taylor, M.; Cotton, J.; Zioupos, P. Finite element simulation of the fatigue behaviour of cortical and cancellous bone, *Meccanica*, **2002**, *37*, 419-429.

[3] Zioupos, P.; Wang, X.T.; Currey, J.D. The Accumulation of Fatigue Microdamage in Human Cortical Bone of Two Different Ages in Vitro, *Clinical Biomechanics*, **1999**, *11*(7), 365-375.

[4] Cotton, J. R.; Winwood, K.; Zioupos, P.; Taylor, M. Simulated material property degradation during fatigue of human cancellous bone, as modelled by a regular honeycomb structure, ASME Summer Bioengineering Conference, Snowbird, Utah, June 27-July 1, 2001.

[5] Zaicenco, A. "FEA for solid mechanics with MATLAB", MATLAB code downloaded from Matlab Central, http://www.mathworks.com/matlabcentral, Posted 12/15/2004.

[6] Winwood K.; Zioupos, P.; Currey, J. D.; Cotton, J.R.; Taylor, M. Development rates of plastic and elastic components of strain in human cortical bone during tensile, compressive and shear fatigue loading and implications to bone biomechanics, *Journal of Biomedical Materials Research*, in press.

[7] Pattin, C.A.; Caler, W.E.; Carter, D.R. "Cyclic Mechanical Property Degradation During Fatigue Loading of Cortical Bone. *Journal of Biomechanics*, **1996**, *29*(1), 69-79.

[8] Griffin, L.V., et al., Model of Flexural Fatigue Damage Accumulation for Cortical Bone. *Journal of Orthopedic Research.*, **1997**, *15*, 607-614.

About the Author

Steven Kemeny

Steven Kemeny is from West Chester, Pennsylvania and went to Unionville High School. He is now a senior in Engineering Science and Mechanics at Virginia Tech. He is focusing his studies in biomechanics and mathematics. Steve wants to have a career in biomedical engineering. He is in the Marching Virginians, one of the marching bands at Virginia Tech. He plays the trumpet and has been a rank leader for two years.

Effect of Carbon Addition and Sintering Temperatures on Densification and Microstructural Evolution of Sinter-Hardening Alloy Steels

Neerav Verma and Saurabh Anand

Department of Materials & Metallurgical Engineering
Indian Institute of Technology, Kanpur, India 208016

Abstract

The iron-copper-carbon alloys are used extensively in powder metallurgy due to their superior dimensional control; however, they possess lower mechanical properties, corrosion resistance and wear resistance than their wrought counter part. In recent years, there have been concerted attempts to engineer ferrous alloys with high dimension tolerance and enhanced mechanical properties. One such approach is to use prealloyed iron powder instead of pure iron, mixed with copper and carbon. SH737-2Cu-C is one such alloy. The present study focuses on the effect of carbon addition on diffusion of Cu in SH737 alloys system via microstructural studies. SH737-2Cu alloys were compacted, sintered and characterized. The materials were characterized according to their density, densification parameter, shape factor, and pore size distribution. The microstructural studies revealed bimodal pore distribution in the sample with no carbon, due to the presence of primary and secondary porosity. The shape factor distribution showed more roundedness in the case of carbon added alloys. The size of the primary pores depends on compaction pressure and powder size distribution. On the other hand, size and morphology of the secondary pore strongly depends on Cu powder size, its homogeneity and sintering temperature. Also, an increase in the sintering temperature increased the roundedness and the pores became coarser.

Keywords: Transient liquid phase sintering, SH737-2Cu alloys, shape facto, pore size, distribution, pore coarsening, primary and secondary pores

1. Introduction

In recent years, ferrous alloys processed using the powder metallurgy (P/M) route have been used extensively in automobile applications. P/M has become a preferred route over other manufacturing processes for a variety of reasons: P/M offers economic advantages, ease in the manufacturing of small-sized pieces with complicated shapes, high dimensional accuracy, greater material utilization (>95%), and flexibility to tailor the composition and engineer the microstructure.[1] P/M products also have greater microstructural homogeneity. The significant advances in powder production technology, new alloy design with novel properties, compaction, and sintering furnace technologies have boosted the growth of powder metallurgy.

Alloying methods of iron are divided into groups: admixed powders, partially prealloyed powder, hybrid powder and coated powder. In furnace alloys, typical alloying additions include Ni, Mo, Mn, Cr, Cu and C. Most of these alloying additions enhance the strength through solid solution hardening during sintering. In addition, these alloying additions also enhance the hardenability by shifting the continuous cooling transformation curve to the right. Subsequent heat treatment results in enhancing the toughness of ferrous alloys.

One of the most common alloying elements used in ferrous powder metallurgy is copper. The use of copper in ingot metallurgy is restricted to weathering steel only. In P/M, because of its low melting point, copper is known to activate sintering at low temperature, which ensures homogeneous mixing of the powder. Presence of copper during liquid phase sintering results in compact swelling. his phenomenon has been mostly observed and extensively investigated in steels containing less than 20 wt% Cu.[2-6] Kayesser *et al.*[6] determined that the molten copper penetration through grain boundaries is the greatest contributor to the swelling phenomenon. It has been observed that compact swelling can be compensated for by the addition of carbon in steels. Dilatometric studies of Fe-C-Cu found that the large expansion associated with the copper growth phenomenon decreases with increasing carbon content.[7-9] Originally this beneficial effect of carbon was attributed to the reduction of Cu solubility in iron and development of a liquid phase.

For the last few decades, there has been an increased desire to use powder metallurgy products as structural components. Structural components require a high relative density for excellent mechanical properties and therefore must have low porosity.[10] A pore acts as a stress concentrator and plays an important role in material failure. The role of porosity on mechanical and physical properties of sintered materials has been studied frequently.[11-14] Formation of secondary pores at the site of original Cu particles is an inevitable consequence of transient liquid phase sintering; therefore, these sintered steels contain numerous largely spherical secondary pores in addition to the pores originating from the green compact. Tina M. Cimino and others observed that mechanical properties of FC-0205 and FC-0208 steels improved with increasing sintering temperature, which is due to the difference in pore morphology and different diffusion mechanism of Cu and Ni during the sintering process. Many researchers observed that copper particle size has no significant effect upon final pore shape.[15-17] The current study was designed to provide quantitative metallography data to understand pore size distribution and the change in pore morphology with different sintering temperatures.

Transient liquid phase sintering of low copper based steel (<9% Cu) forms small secondary pores due to transient liquid formation and large primary pores due to packing characteristic of the powder and binder burn out. In addition to these residual pores, ferrous P/M steels exhibit heterogeneous microstructures due to inhomogeneous distribution and incomplete diffusion of alloying elements. The influence of chemical and microstructural homogeneity on the mechanical properties of sintered material has been studied by a number of researchers.

Table 1. Composition of the powder

Elements	Fe	Mo	Mn	Ni	Cu	C
% (by wt)	94.03	1.25	1.4	0.42	2	0.9

Table 2. Characteristics of experimental powder

Source	D_{10} (µm)	D_{50} (µm)	D_{90} (µm)	Mode size, (µm)	Width of distribution (µm)	Apparent Density, (g/cm^3)	Tap Density, (g/cm^3)	Flow Time, (s/50g)
Hoeganaes	32	58	88	75	0.47	3.62	3.98	20

This study focuses on the investigation of one such alloy SH737 (designated) which has a nominal composition of Fe-1.25 Mo-1.4 Ni-0.42 Mn (wt%). This grade of powder has also been referred as sinter-hardening grade, which achieves sintering and hardening in a single step.

2. Experimental Procedure

For the present investigation, two partially prealloyed powder mixtures, (a) and (b), were made by a proprietary process developed by Hoeganaes Corp viz.[18-19]

(a) Fe, 1.4 wt % Ni, 1.25 wt % Mo, 0.42 wt % Mn, 2 wt % Cu or SH737-2Cu

(b) Fe, 1.4 wt % Ni, 1.25 wt % Mo, 0.42 wt % Mn, 2 wt % Cu, 0.9 wt % C or SH737-2Cu-0.9C

The as received powder was characterized for its flow behavior, apparent, and tap density using set MPIF standards. The results are tabulated in Tables 1 and 2. The cumulative weight percent of the powder particles vs. particle size is displayed in Figure 1. A SEM image of the powder used for sample preparation is shown in Figure 2.

Powders were pressed at 600 MPa in a 50 ton uniaxial hydraulic press (APEX construction Ltd, UK). Densities of the compacted specimens were between 6.99 and 7.02 g/cm^3. To minimize friction, the compaction was carried out using zinc stearate as a die wall lubricant. The powder contains 0.75 wt.% acrawax, which was added to the powder to facilitate its compaction during sintering. The sintering response on densification

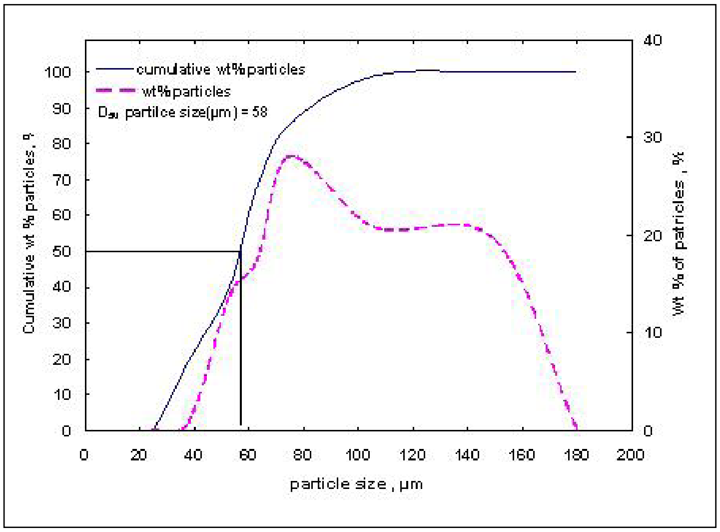

Figure 1. Cumulative weight % of the powder particles vs particle size

and microstructures were evaluated on cylindrical pellets (16 mm diameter and 6 mm height). The wax was removed from the green compacts in a tubular silicon carbide (SiC) furnace under N_2-20% H_2 atmosphere. The lubricant was removed from the green samples using a heat treatment at 850 °C for 30 min. To prevent cracking of green compacts by thermal shock, the green samples were heated at 3 °C/min. Then the compacts were sintered at two different temperatures, 1120 °C and 1180 °C, for 30 min in a tube furnace with SiC heating elements. The thermal profiles for the sintering are shown in Figure 3. All the sintering was carried out under N_2-20% H_2 atmosphere.

The sintered density was obtained by dimensional measurements. The densification parameter was calculated to determine the amount of densification that occurred during sintering. It is expressed as:

$$\text{Densification parameter} = \frac{(\text{sintered density - green density})}{(\text{theoretical density - green density})} \quad (1)$$

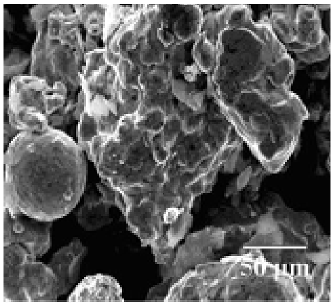

Figure 2. SEM image of the powder used for sample preparation

Standard metallographic practices were employed for sample preparation for microstructural examination. The sintered samples were mounted, with the help of epoxy, and wet polished in a manual polisher (model: Lunn Major, supplier: Struers, Denmark) using a series of SiC emery papers followed by cloth polishing using a suspension of 1 µm and 0.03 µm alumina.

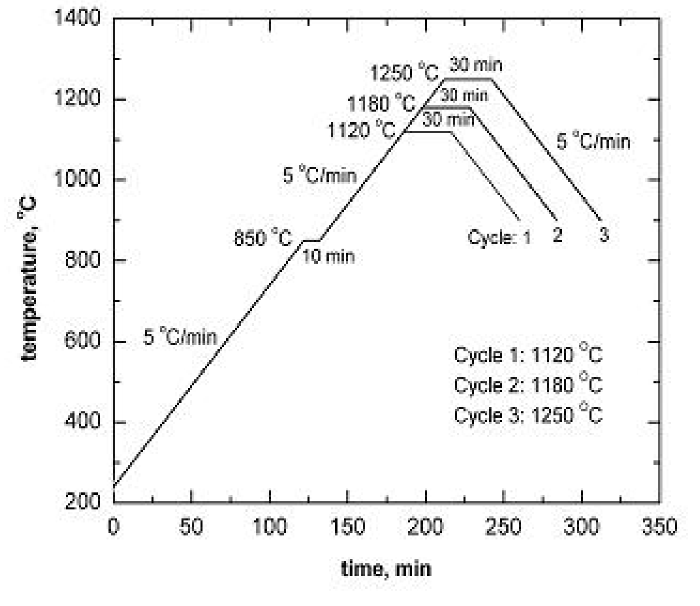

Figure 3. Sintering temperature profiles for SH737Fe-2Cu-0.9C for different temperatures

An optical microscope with digital image acquisition capability (model: LABORLUX 12 ME S, supplier: Leitz Germany) was used to obtain the micrographs of sintered polished samples. Pictures (20 at each sintering temperature) were taken randomly with an optical microscope at a magnification of 100X. The size of pores was measured manually with a precision of 1 mm. For each sample, more than 5,000 readings were taken in order to eliminate experimental errors and get statistically correct results.

At the same time, quantitative metallographic analysis was performed on the samples, according to standard pixel analysis method, on a calibrated image analysis system.

Some basic parameters were determined from quantitative analysis. A well-known and often used characteristic for particle irregularity characterization is roundness of the object (RN). It is defined as:[20,21]

$$RN = P^2/4\pi A \qquad (2)$$

where P is the circumference and A is the area. The roundness of a circle is equal to one. If the object's shape approaches a line segment, it approaches infinity. To characterize the roundness, sometimes a shape factor SF=1/RN is used, where SF predicts the degree of irregularity. A shape factor equal to one represents a circular pore. As the number decreases from one, the degree of irregularity increases. The roundness factor proposed by Salek *et al.*[12] RFN is define by the relationship

$$RFN = P/d_A \qquad (3)$$

where d_A is the diameter of the circle with the same area as the particle.

In addition to quantitative analysis of the unetched microstructure, optical microscopy was conducted on samples in the etched condition and the SF calculated.

3. Results and Discussion

The current study provides a quantitative metallography analysis protocol to understand pore size distribution and

Table 3. Average volume % of porosity for the sintered samples

Sintering Temperature(°C)	Pore Volume percent (%)	
	0% C	0.9% C
1120	11.75±0.67	12.52±0.84
1180	13.14±0.59	11.89±0.76

change in pore morphology with addition of carbon and different sintering temperatures for SH737-2Cu alloys.

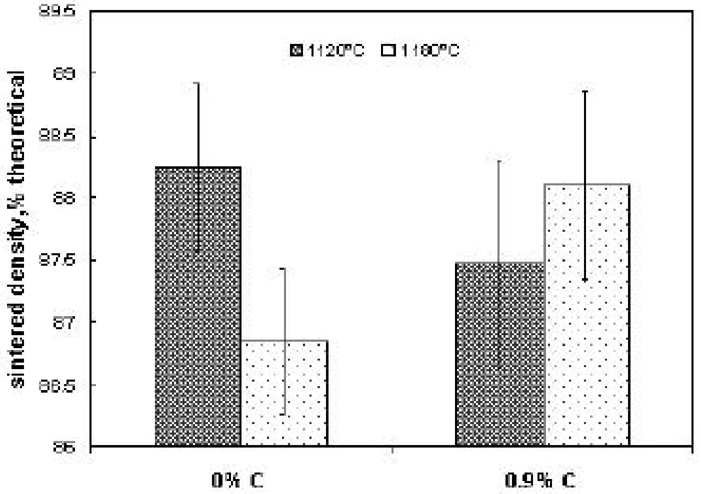

Figure 4. Effect of sintering temperature and carbon addition on sintered density (% theoretical) of SH737-2Cu system

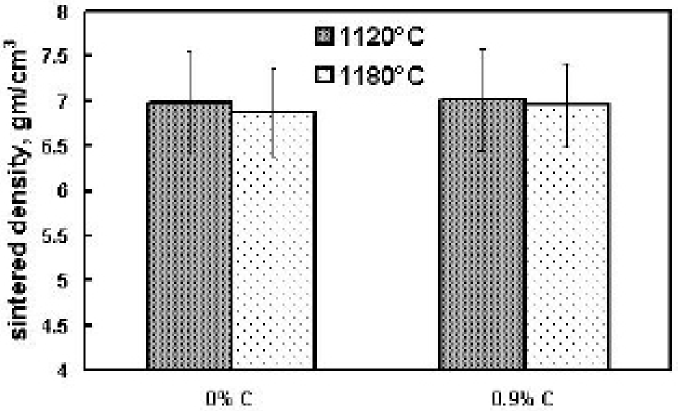

Figure 5a. Effect of sintering temperature and C addition on sintered density of SH737-2Cu system

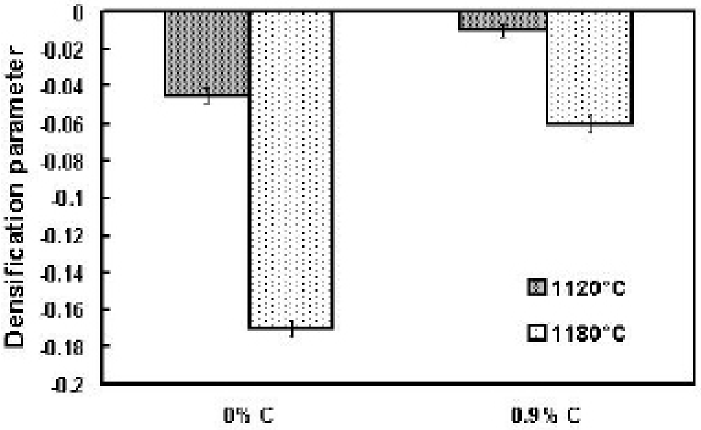

Figure 5b. Effect of sintering temperature and C addition on densification parameter of SH737-2Cu system

Cylindrical samples with green density of 6.98 ± 0.02 g/cm³ were used for sinter density measurement and pore volume fraction calculation, as shown in Table 3. For all the cases, the volume fraction of pores lies between 11 and 14%. The total porosity was determined through quantitative image analysis.

The residual porosity after sintering may be characterized as either primary or secondary pores. Primary pores are large pores that result from geometric packing of the particles or from binder burn out. Secondary porosity is typically smaller in nature and may be attributed to residual porosity from liquid phase formation and diffusion of alloying addition, such as copper. Due to secondary pore formation, the sintered density is lower than the green density in this alloy. The effect of sintering temperature and carbon addition on sintered density (percent theoretical), in the SH737-2Cu system is shown in Figure 4. Figure 5a compares the effect of carbon and sintering temperature on the density of SH737-2Cu alloys. The sintering density varies marginally with sintering temperature and addition of carbon. Figure 5b shows the effect of sintering temperature and carbon addition on the densification parameter of the SH737-2Cu system.

The densification parameter gives an account of whether swelling or shrinkage is occurring in the sample. As can be clearly seen, in both cases we obtain swelling in the sample. In the absence of carbon, we obtain slight swelling due to the diffusion of copper. As the amount of carbon is increased, the sintered density is observed to rise and swelling is reduced.

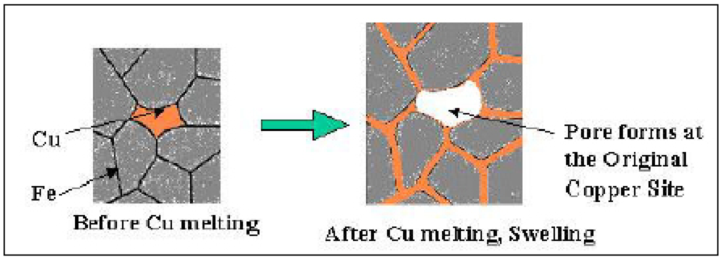

Figure 6. Process of transient liquid phase sintering resulting in the diffusion of copper, porosity, and swelling in sintered hardened samples

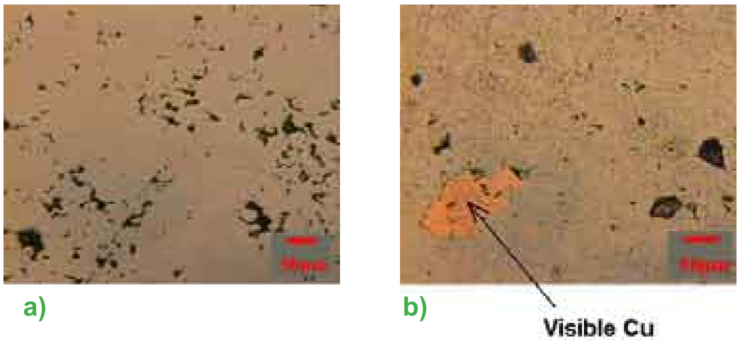

Figure 7. Optical microstructures of a) SH737-2Cu, b) SH737-2Cu-0.9C, showing absence of visible copper in case of SH737-2Cu due to Cu diffusion into the matrix of iron

More swelling corresponds to a more negative value of densification parameter, so more swelling was obtained for the sample without any carbon addition due to the free diffusion of the copper into the matrix as a result of transient liquid phase sintering. This can be seen in Figure 6 at 1120 °C and 1180 °C.

Carbon hinders "copper growth," preventing excessive penetration of copper rich liquid along grain boundaries or interparticle boundaries. Because of the increase in the dihedral angle between iron and copper, there was a reduction in swelling due to the carbon addition. This process of hindering of copper diffusion can be seen in Figure 7, where unalloyed metallic Cu can be seen at distinct places in optical microstructures in the case of 0.9% carbon addition.

Figure 8 shows the shape factor distribution of pores in samples SH737-2Cu and SH737-2Cu-0.9C at (a) 1120 °C and (b) 1180 °C as sintering temperatures. In case there was no carbon, we obtained a bimodal distribution because of two types of pores forming:

(a) Primary pores formed at the time of compaction process

(b) Secondary pores formed at the time of sintering process due to copper diffusion due to transient liquid phase sintering

In the case of 0.9% addition of carbon, the average SF approaches unity, i.e. more roundedness. This increase in roundness results from the contribution of pores, which is only due to compaction; therefore, more circular pores are obtained, implying relatively more roundedness of primary pores as compared to secondary pores.

In the case of no carbon addition, the average SF decreases. This decrease is now due to contribution of two things: firstly due to secondary pores, which are more irregular; secondly due to primary pores, which are relatively spherical and have shape factor value close to unity. We can then deduce that in the bimodal distribution, the right peak is for the primary pores

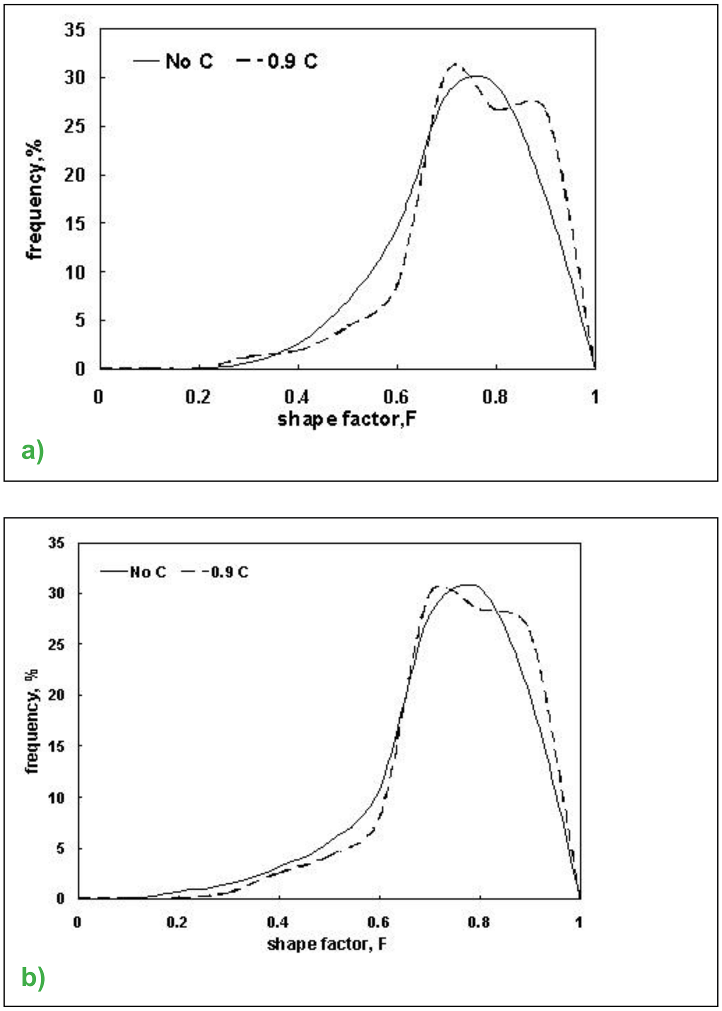

Figure 8. Variation of frequency % with shape factor of pores in samples SH737-2Cu and SH737-2Cu-0.9C at a) 1120 °C and b) 1180 °C as sintering temperatures

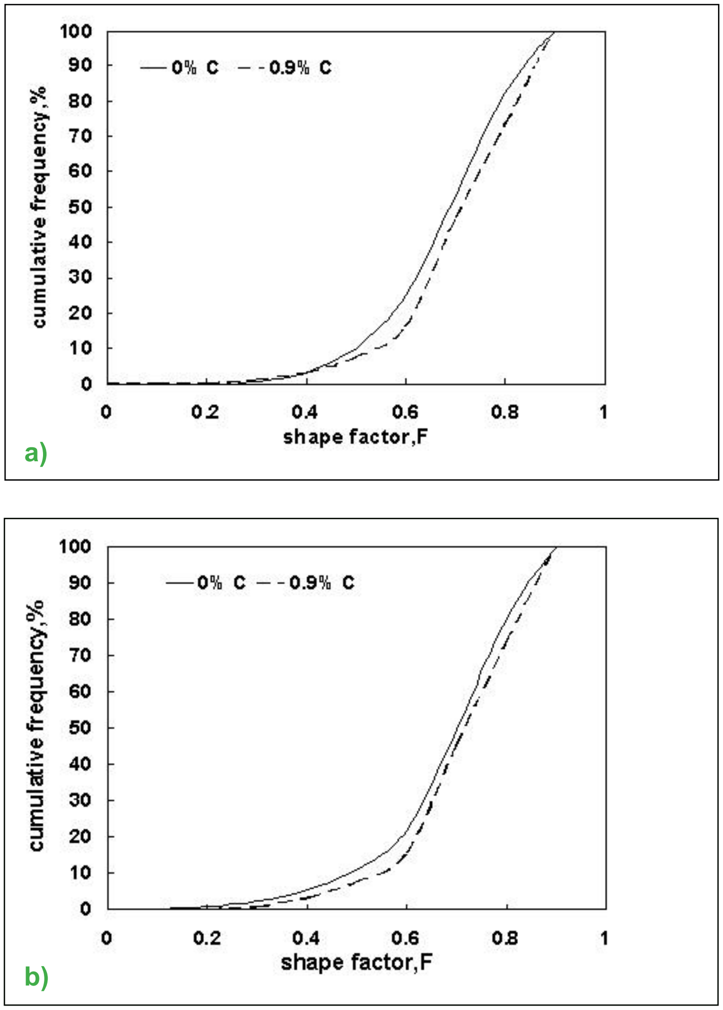

Figure 9. Cumulative frequency distribution of SH737-2Cu and SH737-2Cu-0.9C at a) 1120 °C and b) 1180 °C as sintering temperatures

showing more spherical nature of such pores, and the left peak is for the secondary pores which are relatively more irregular.

More average roundedness of pores (SF approaching to one) in the case of 0.9% carbon can clearly be seen from Figure 9, which shows cumulative frequency distribution of SH737-2Cu and SH737-2Cu-0.9C at sintering temperature of a) 1120 °C and b) 1180 °C. For both sintering temperatures, the plot of 0.9% C is consistently shifted to the right of 0% C plot, and thus more average roundedness in case of carbon addition.

Figure 10 shows the distribution of pore SF for different sintering temperatures (i.e. 1120 °C and 1180 °C) for (a) SH737-2Cu and (b) SH737-2Cu-0.9C. The SF gives a quantitative measure of pore morphology. A SF equal to one represents a circular pore in the plane of analysis, and as the number decreases from one, the degree of irregularity increases. The shape analysis graph shows that pores at 1120 °C sintered samples are more irregular. With an increase in temperature, the peak of the graphs shift marginally towards the right side for both (a) and (b); therefore, overall irregularity of the mass of pores decreases with increasing sintering temperature. Because the SF is a ratio of pore area and pore perimeter, the frequency vs. SF plot does not predict the effect of pore size on SF.

Figure 11 shows the effect of pore size on SF. From this figure, it is obvious that pores below 100 μm^2 have a SF between 0.3 and 0.85. It is also clear from this figure that pores in this range have a wide distribution in shape. Furthermore, results indicate that pores above 100 μm^2 are more irregular and have a SF from 0.4 to 0.15. It can also be seen that at higher sintering temperature the large pores become more irregular. Figure 12 and Figure 13 show the pore size distribution of SH737-2Cu and SH737-2Cu-0.9C samples for sintering temperatures of (a) 1120 °C and (b) 1180 °C.

As can be clearly seen, the maximum pores have a size below 100 μm^2, which is true for both sintering temperatures. From Figure 11, pore coarsening is clearly visible at higher sintering temperature (1180 °C)—the frequency of large pores (pore area of about 1500 μm^2)—increases with increasing sintering temperature. Pore coarsening can also be seen in Figure 12,

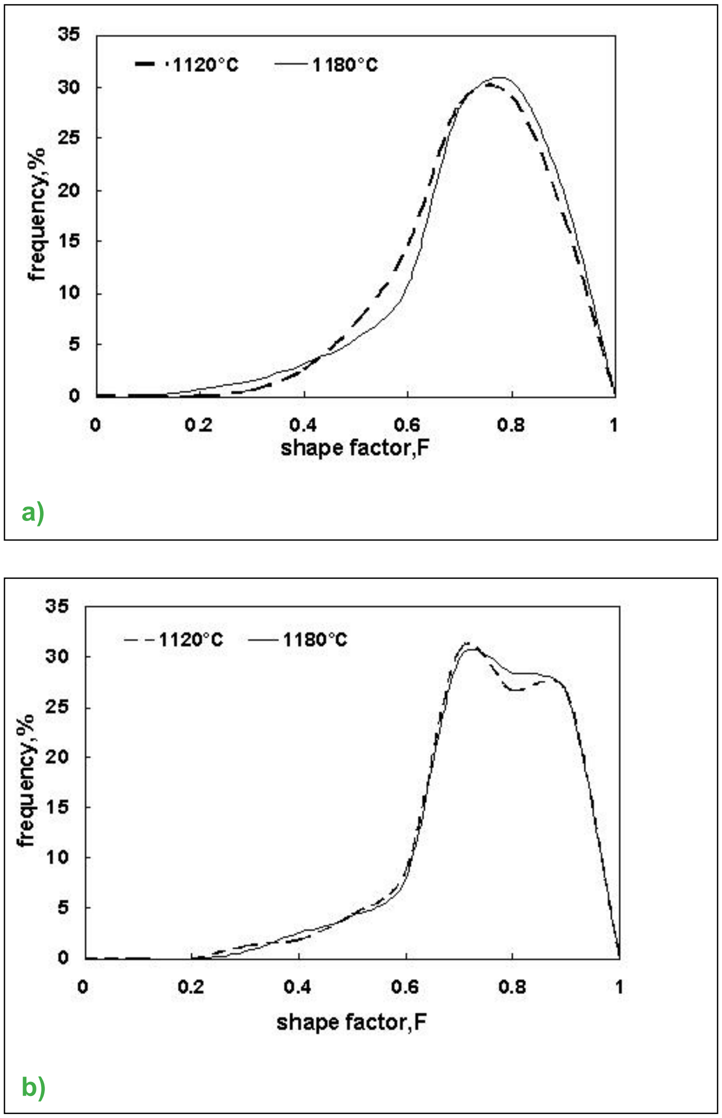

Figure 11. Variation of frequency % with shape factor of pores in samples a) SH737-2Cu and b) SH737-2Cu-0.9C at 1120 °C and 1180 °C as sintering temperatures

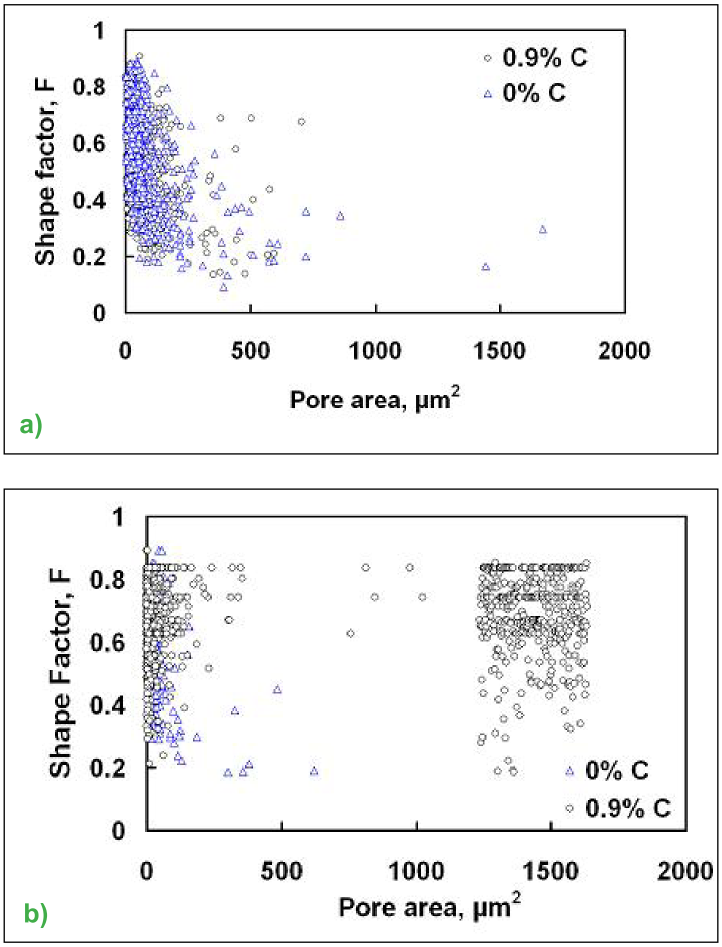

Figure 12. Variation of SF of pores with pore area of SH737-2Cu and SH737-2Cu-0.9C samples for sintering temperatures of a) 1120 °C and b) 1180 °C

which shows pore size distribution dependence on sintering temperature. Figure 13(a) and (b) show that as the sintering temperature increases, the frequency of larger pores increases and the frequency of smaller pores decreases. Pore coarsening can also be noticed in the optical microstructures shown in Figure 14.

4. Conclusions

In this study, the effect of sintering temperature and addition of carbon on the microstructure and pore morphology of a sintered alloy steel was examined. The following conclusions can be made based on the results obtained from this study:

- Carbon hinders "copper growth," preventing excessive penetration of copper rich liquid along grain boundaries or interparticle boundaries, thus reducing the swelling.
- Pore coarsening occurs in the alloy at higher sintering temperature. The average pore size increases from 7 μm to 10 μm with an increase in sintering temperature from 1120 °C to 1180 °C. At higher sintering temperature, coarser pores (> 18 μm) tend to be more irregular. However, on average, the pores tend to attain a more rounded morphology at higher sintering temperature.

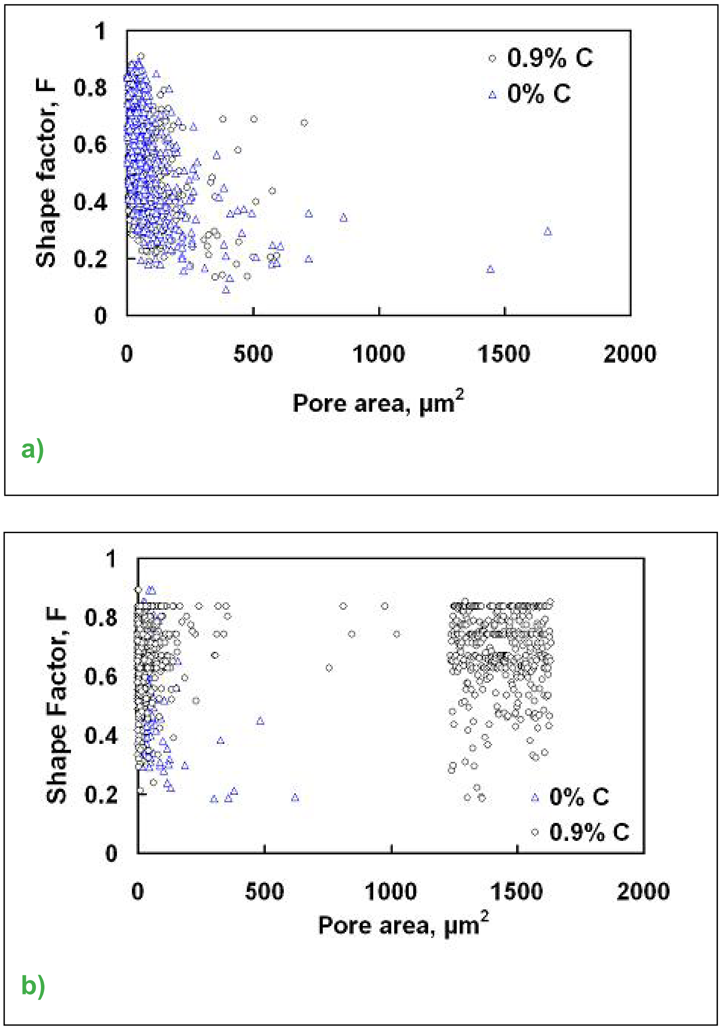

Figure 13. Pore size distribution of SH737-2Cu and SH737-2Cu-0.9C samples for sintering temperatures of a) 1120 °C and b) 1180 °C

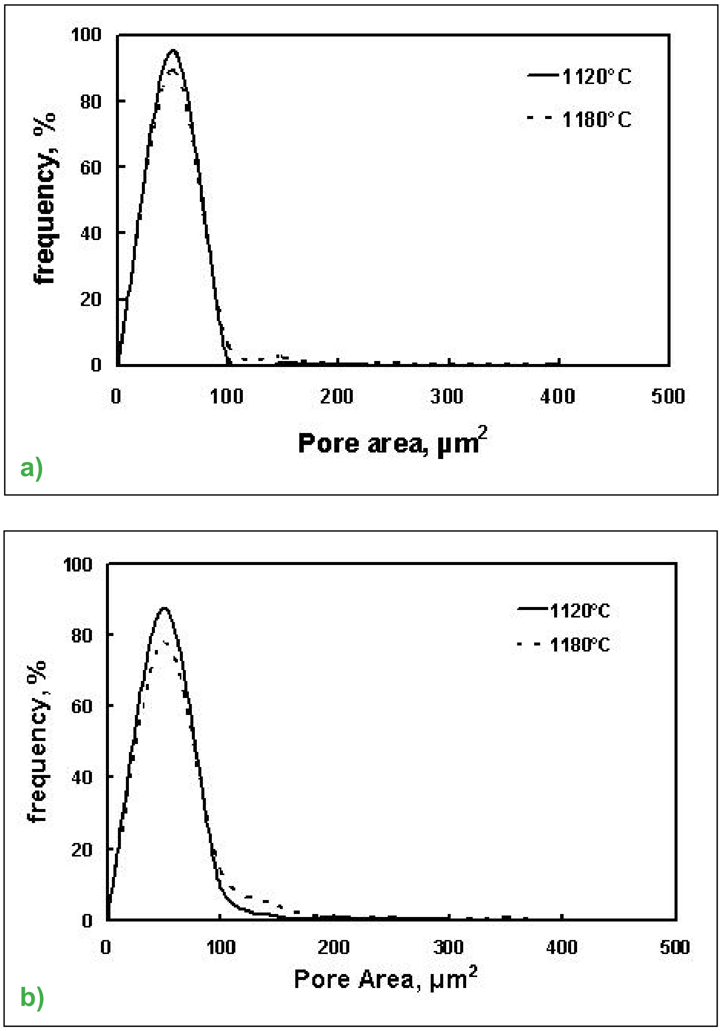

Figure 14. Effect of sintering temperature on pore size distribution for a) 0% C and b) 0.9%C

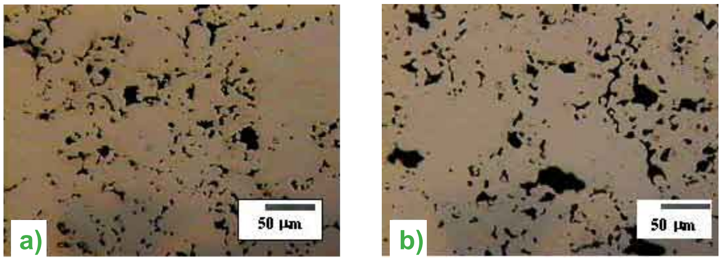

Figure 15. Optical microstructures of SH737-2Cu sintered at a) 1120 °C and b) 1180 °C showing pore coarsening occurring at higher sintering temperatures

- A bimodal SF distribution was obtained in the case of no carbon addition, primarily due to the presence of both types of pores, namely primary and secondary.

Acknowledgments

The authors gratefully acknowledge Dr. Anish Upadhyaya, Associate Professor, Department of Metallurgical and Materials Engineering, IIT Kanpur, for his supervision and Dr. Narasimhan from Hoeganaes Corporation for providing us with the working powders and for his suggestions and support.

References

[1] Upadhyaya, G. S. *Sintered Metallic and Ceramic Materials Preparation, Properties and Applications*. J. Wiley & Sons: New York, NY, USA, 1999; Vol. 1,

[2] Durdallar, C. The Effect of Additions of Cu, Ni and C on the Sintered Properties of Iron-Base Sintered P/M Parts. *Progress in Powder Metallurgy* **1969**, *25*, 73.

[3] Lenel, F. V.; Hwang, K. The Mechanical Properties of High Density Iron-Copper Alloys from a Composite Powder. *Powder Metallurgy Internationals* **1980**, *12*(20), 89.

[4] Krantz, T. Effect of Density and Composition on the Dimensional Stability and Strength of Iron-Copper Alloys. *International Journal of Powder Metallurgy* **1969**, 5(3), 35.

[5] Trudel, Y.; Angers, R. Properties of Iron-Copper Alloys made from Elemental or Prealloyed Powders. International *Journal of Powder Metallurgy and Powder Technology* **1975**, *11*(1), 5.

[6] Berner, D.; et. al. Swelling of Iron-Copper Mixtures during Sintering and Infiltration. *Modern Developments in Powder Metallurgy* **1973**, *6*, 237.

[7] Tabeshfar, K.; Chadwick, G. A. Dimensional Changes During Liquid Phase Sintering of Fe-Cu compacts. *Powder Metallurgy* **1984**, *27*(1), 19.

[8] Jamil, S. J.; Chadwick, G. A. Investigation and Analysis of Liquid Phase Sintering of Fe-Cu and Fe-Cu-C compacts. *Powder Metallurgy* **1985**, *33*(2), 65.

[9] Lawcock, R. L.; Davies, T.A. Effect of carbon on Dimensional and Microstructural Characteristics of Fe-Cu compacts during sintering. *Powder Metallurgy 1990*, *33*(2), 147.

[10] Brian James, W. *International Journal of Powder Metallurgy and Powder Technology* **1985**, *21*(2), 163.

[11] Karlsson, B.; Bertilsson, I. Scand. *Journal of Metallurgy* **1982**, *11*, 267.

[12] Salak, A.; Miskovic, V.; Dudrova, E.; Rudnayova, E. *Powder Metallurgy International* **1974**, *6*, 128.

[13] Kreher, W.; Siegel, S.; Tecza, W. *Proc Int. PM Conf. DDR, Dresden*, **1977**, *1*, 13.

[14] Haynes, R. *The Mechanical Behaviour of Sintered Metals*; Freund Publishers: London, 1981.

[15] Danninger, H. *Powder Metallurgy International* **1987**, *19*, 1.

[16] Cimino, T. M.; Graham, A. H.; Murphy, T. F. *Industrial Heating* **2000**, *September*.

[17] Christian, K. D.; German, R. M. *International Journal of Metallurgy* **1995**, *31*, 1.

[18] Chawla, N.; Fillari, G.; Narasimhan, K. S. in *Powder Materials: Current Research and Industrial Practices*. F.D.S. Marquis. Ed. TMS: Warrendale, PA, 1999; pp 247.

[19] Luk, S. H.; Hamill. Jr., J. A. *Advances in Powder Metallurgy and Particulate Materials*. Metal Powder Industries Federation: Princeton. NJ, 1993 ; pp 153.

[20] Kulu, P.; Tümanok, A.; Mikli, V.; Käerdi, H.; Kohutek, I.; Besterci, M. Possibilities of Evolution of Powder particle granulometry and morphology by image analysis. *Proc. Estonian Acad. Sci. Eng.* **1998**, *4*, 3.

[21] Saltykov, S. A. *Stereometric Metallography*. Metallurgiya, Moscow, 1976 (in Russian).

About the Authors

Neerav Verma

Neerav Verma is a senior undergraduate student of Materials and Metallurgical engineering in Indian Institute of Technology, Kanpur, India. The versatile field of Material science has always captivated him and the research areas in it have inspired him to explore them and ameliorate his knowledge to come up with decent research work. He has been involved in a rigorous research work in the field of Powder Metallurgy which included "Investigation Of Densification And Microstructural Evolution Of Sinter-Hardening Alloy Steels." He has also worked in the field of characterization of Construction Materials during his 2006 summer internship at LMC Lab, EPFL, Lausanne, Switzerland.

Saurabh Anand

Mr. Anand is currently pursuing his degree from the Department of Materials and Metallurgical Engineering at the Indian Institute of Technology, Kanpur. He has always been fascinated by the practical application of intellectual and conceptual knowledge. Recently, he has become absorbed in empirical works on powder metallurgy. Saurabh worked on a paid research project on sintered hardened grades of steel powders which included investigation of its densification, mechanical properties, and microstructural evolution. He recently completed a summer internship in an exchange program by the Australian government working on "Nanostructured Materials and Materials with Inhomogeneous Microstructure."

Particle Spacing Effects on the Strengthening of Discontinuously-Reinforced Polymer Matrix Composites

Steven A. Kyriakides and A. Ramsey Persing

Virginia Polytechnic Institute and State University, Department of Materials Science and Engineering
Blacksburg, Virginia 24061

Abstract

In metal matrix composites, the spacing between discontinuous reinforcements can affect strengthening by interfering with the motion of dislocations through the metal. This project looks for similar phenomena in polymer matrix composites (PMCs), since the molecular activity of the polymer chains should be altered in the vicinity of the reinforcements. Awareness of such a trend can improve the understanding of PMC mechanics, which in turn can improve PMC characterization and selection techniques. This project sought a relationship between particle spacing and overall strengthening in a discontinuously-reinforced PMC test case composed of alumina particles in a polyphenylene sulfide matrix. Tensile tests were run on hot-pressed composite samples with varying reinforcement volume fraction and particle size. Data showed that composite strength increases as particle spacing increases, except at high volume fractions where this trend reverses. These results provide preliminary data but demonstrate a need for more in-depth investigation.

Keywords: Spacing, strength, PMC

1. Introduction

As designers and engineers implement polymer matrix composites (PMCs) into an increasingly wide variety of applications, the need for accurate and detailed information about the characteristics and properties of these materials grows.[1-4] Engineers commonly use strength data as a means for comparing and selecting materials for industrial application. The amount of reinforcement by volume and its effect on composite strength is the most frequently studied relationship in most discontinuously-reinforced (DR) composites. In contrast, the effect of the reinforcement spacing, which accounts for volume fraction and size of reinforcements, on composite strength is still unclear in DR PMC systems, though there are well-understood behaviors observed in metal-matrix composites (MMCs).[5-7]

To control the spacing in these systems as an independent variable in strength tests, the particle size can be varied for a constant reinforcement volume fraction (V_R). Producing samples to test this effect requires a processing method that can produce high-quality specimens with minimal variation between batches. From these specimens, tensile tests provide strength values that can be statistically analyzed to identify any relationships present between particle spacing and composite strengthening.

2. Theory

Current research contains little on the particle spacing effect on strength in PMCs. Since little research was found in PMCs, the work in MMCs was consulted for a basis in forming a hypothesis. When considering the strength of a metal or MMC, the Orowan effect tells us that the presence of small, incoherent phases or particles can increase the overall strength of the material. As dislocations move past these particles, they form loops that surround the particles and interfere with subsequent dislocation motion, thus raising the strength of the material.[8, 9] This phenomenon implies that a small particle spacing will provide the best composite strengthening. It is also known that if the spacing between these particles is too small, then the dislocations will not pass between the particles; in contrast, widely spaced particles affected by these loops do not typically impact the strengthening significantly. An intermediate distance between the particles must therefore be determined to obtain the optimum strengthening.

Though this phenomenon accurately describes the behavior of MMCs, it cannot be directly applied to PMCs, since dislocations are not present within polymers. With the basic understanding that polymer deformation is achieved primarily through the motion of polymer chains, particle spacing in a DR PMC should also affect the strength of that composite material. For two PMC samples with an equal V_R but different spacing between the particles, implying varied particle sizes, the specimen with larger particles having more material between them should have more space available for the polymer chains to freely move. In contrast, smaller closely-packed particles should impede the motion of those chains, thereby strengthening the composite.

3. Experimental

To test for a relationship between particle spacing and composite strengthening, techniques were developed to process a DR PMC and to obtain tensile test specimens from the processed composite.

3.1 Material Selection and Characterization

The matrix needed to be a nontoxic, semicrystalline thermoplastic with a glass transition temperature (T_g) above room temperature; polyphenylene sulfide (PPS) was selected based on these criteria. Alumina (Al_2O_3) polishing powder in 5.0-µm and 0.05-µm particle sizes was selected as the reinforcement phase. Tabulated densities of both materials and particle sizes of the reinforcement were verified through characterization prior to using these values in calculations.

3.2 Processing Options

Both V_R and $L_{e\cdot e}$ were varied to observe strengthening trends with respect to the particle spacing. Volume fractions of 1%, 3%, and 10% alumina were selected. Edge-to-edge spacing $L_{e\cdot e}$ values for these conditions are reported in Table 1 according to Equation 1 below:[10]

$$L_{e\cdot e} = 1.25\, r\left(\frac{2p}{3V_R}\right)^{1/2} - 2r\sqrt{\frac{2}{3}} \qquad (1)$$

Table 1. Theoretical particle spacing values in µm

Particle Size, µm	Volume Fraction, V_R		
	1%	3%	10%
0.05	0.8229	0.4406	N/A
5.00	82.2852	44.0565	20.4379

As shown in Table 1, the spacing between particles decreases with increasing volume fraction and with decreasing particle size. These values illustrate the selected conditions (5.0 and 0.05 µm particles with 1%, 3%, or 10% V_R) should produce significantly differing spacings.

Two techniques, injection molding and hot pressing, were considered for producing the DR PMCs for this project. Injection molding, using a Dynisco LMM injection molder, involved mixing the alumina with melted PPS; poor mixing and the settling of the alumina particles clogged the injection nozzle several times and did not produce any testable samples.

Hot pressing yielded better results, producing 7.5 cm x 12.5 cm composite plates. For this method, PPS and alumina powders were mixed by ball milling. The processing method developed for this experiment entailed hot pressing under the following parameters:

- 10 minute melt time
- ~1.25 MPa applied pressure
- 275 °C top plate, 285 °C bottom plate

These conditions allowed for a sufficient amount of time to ensure a fully melted sample while minimizing porosity and particle settling

3.3 Sample Preparation

Tensile test specimens were made from the pressed plates of composite through two steps: cutting blanks from the plates and punching dogbone specimens from each blank.

Using the punch on a material as brittle as the PMC in this lab causes substantial cracking in the surrounding part; to avoid excess material waste, small rectangles were cut from the large plate using a band saw. These blanks were cut slightly larger than the dogbones. Through this technique, a dozen dogbones can be quickly made from a single hot-pressed plate.

3.4 Tensile Testing

A Texture Technologies Corp. TA-XT2i Texture Analyser was used for the tensile testing. This machine proved to be suitable to our experiment by having a small test frame with a 50 g (~500 N) load cell; difficulties with this machine included a relatively fast strain rate (0.1 mm/s) and uncertainty in the calibration of the equipment. For this reason, exact values of the data presented herein are may not be accurate, though the observed trends should still apply. Flaws produced during the processing and sample preparation stages (porosity, notches, cracks) caused an extremely large scatter among the data, which is typical of failure testing of other brittle materials.

4. Tensile Test Results and Discussion

Preliminary tensile testing was performed to try and observe any general trends present in the strengthening of the PMC. Tables 2 and 3 present data for increasing volume fraction for particle sizes of 0.05 and 5 μm, respectively.

The strength values for both particle sizes show a decrease as V_R is increased from 1% to 3%, indicating that strength decreases with particle spacing. With the 5.0 μm particles, though, strength increased from 3% to 10% V_R, meaning that strength increases as particle spacing decreases. This discrepancy could occur because 3% may correspond to V_{min} similar to that described by Agarwal; this V_{min} would represent the V_R for which the composite strength is at a minimum, even compared to the strength of the unfilled matrix.[11]

Tables 4 and 5 show the strength effects of increasing particle size for V_R values of 1% and 3%, respectively.

For both V_R values, increasing the particle size (thereby increasing the particle spacing) increases the strength of the composite. This matches the trend observed when increasing from 1% to 3% V_R for a constant particle size but disagrees with the trend hypothesized in Section 2 (that strength should increase with decreasing particle spacing).

5. Conclusions and Future Work

5.1 Conclusions

Hot pressing successfully produced DR PMCs. Using a punch to produce dogbones caused some imperfections that affected the tensile test results. It may be necessary to abandon punching dogbones and to cut samples (not necessarily dogbones) by some other means.

Results from tensile testing demonstrate that for lower particle volume fractions, increasing the V_R (decreasing the particle spacing) decreased the composite strength, though at higher V_R values this trend is reversed. For a constant V_R, increasing the particle size (decreasing the particle spacing) increased the strength. Overall, these results show that composite strength increases with particle spacing, though the specific strengthening mechanism cannot yet be determined. These results are only preliminary; further research is necessary to draw any definite conclusions about the effect of particle spacing on PMC strengthening.

5.2 Future Work

To continue using a PPS matrix, more tensile tests must be performed, since PPS is a brittle materials and its failure can only be properly studied through in-depth statistical analysis. Using a more ductile material like polyethylene would allow the yield strength to be measured instead of fracture strength. In this situation, fewer samples would be necessary, since the yield phenomenon is less variable than fracture. This is because yield values generally show less variation than do fracture strength measurements.

While it appears that the processing method described above is adequate for producing DR PMC samples with good particle dispersion, additional characterization can be applied to verify this. Accurate microscopy could verify the spacing values predicted or scanning electron microscopy (SEM) could be used to look for particle agglomeration and flaws on fracture surfaces. Further characterization of the polymer matrix (i.e. crystallinity, molecular weight) could also help to explain the observed results. Finally, a more accurate and easily controlled tensile tester should produce more reliable data. In particular, a test frame with a high load capacity (~500 N), slower strain rates (0.01 mm/s or less), and finer resolution for measuring extension or strain (0.005 mm or less) would be ideal.

Acknowledgments

The investigators would like to thank the Materials Science and Engineering department at Virginia Tech for funding this senior design project. They are also extremely grateful to Dr. Jon Geibel of Chevron Phillips for donating the PPS used in this project and to Dr. Garth Wilkes of Virginia Tech for his advice and support. Dr. Brian Love's and Dave Berry's assistance

Table 2. Data for 0.05 μm particles at 1%, 3%, and 10% V_R

		1%	3%
Median Tensile Strength	(MPa)	19.87	15.32
Average Strength	(MPa)	24.98	18.01
Coefficient of Variation		0.5523	0.6132

Table 3. Data for 5.0 μm particles at 1%, 3%, and 10% V_R

		1%	3%	10%
Median Tensile Strength	(MPa)	28.68	21.73	25.79
Average Strength	(MPa)	31.63	28.36	30.85
Coefficient of Variation		0.2267	0.6445	0.3610

Table 4. Particle size (spacing) effects on strength for 1% V_R

		0.05 μm	5.0 μm
Median Tensile Strength	(MPa)	19.87	28.68
Average Strength	(MPa)	24.98	31.63
Coefficient of Variation		0.5523	0.2267

Table 5. Particle size (spacing) effects on strength for 3% V_R

		0.05 μm	5.0 μm
Median Tensile Strength	(MPa)	15.32	21.73
Average Strength	(MPa)	18.01	28.36
Coefficient of Variation		0.6132	0.6445

with the testing and processing equipment is also appreciated. Finally, thanks go to Dr. Marie Paretti and Dr. William Reynolds for supervising and advising the MSE senior design projects.

References

[1] Guhanathan, S; Devi, M. "Physicochemical Characterization of the filler–Matrix Interface in Elastomer-Encapsulated Fly Ash/Polyester Particulate Composites," *Journal of Applied Polymer Science*, **2005**, *97*, 171-184.

[2] Al-Kandary, S.; Ali, A.A.M.; Ahmad, Z. "Morphology and thermo-mechanical properties of compatibilized polyimide-silica nanocomposites," *Journal of Applied Polymer Science*, **2005**, *98*, 2521-2531.

[3] Kumar, A.A.; Alagar, M.; Rao, M. "Preparation and characterization of siliconized epoxy/bismaleimide (N,N -bismaleimido-4,4 -diphenyl methane) intercrosslinked matrices for engineering applications," *Journal of Applied Polymer Science*, **2001**, *81*, 38-46.

[4] Gardiner, G. "Thermoplastic Composites Gain Leading Edge on the A380," *High-Performance Composites*, **2006**, *March*.

[5] Aldrich, D.; Fan, Z. "Microstructural characterisation of interpenetrating nickel/alumina composites," *Materials Characterization*, **2001**, *47*, 167-173.

[6] Zu, Z.W.; Yan, H.C.; Wu, G.H.; Kong, X.L.; Yang, S.Q. "Interface structure and strength of ultrasonic vibration liquid phase bonded joints of Al2O3 / 6061A1 composites," *Scripta Materiala*, **2005**, *53*, 835-839.

[7] Ramesh, C.; Khan, A.R.A.; Ravikumar, N.; Savanprabhu, P. "Prediction of wear coefficient of Al6061-TiO2 composites," *Wear*, **2005**, *259*, 602-608.

[8] Aiken, R.M. "The Mechanical Properties of In-Situ Composites," *JOM*, **1997**, *8*, 35-39.

[9] Reed-Hill, R.E. *Physical Metallurgy Principles; 3rd edition*, PWS Publishing Company: Boston, MA, 1994.

[10] Martin, J.W. *Micromechanisms in Particle-Hardened Alloys*. New York: Cambridge University Press, 1980.

[11] Agarwal, B.D.; Broutman, L.J. *Analysis and Performance of Fiber Composites*. New York: John Wiley & Sons, 1980.

About the Authors

(L-R) Authors A. Ramsey Persing and Steven A. Kyriakides

Steven A. Kyriakides

Steven, a native of Richmond, Virginia, graduated from the Virginia Tech Materials Science and Engineering department in May of 2006. During his time there, he was heavily involved with the music department and actively participated in several engineering organizations. He has also served on the editorial board for *JUMR* since its founding. At the time of publication, he is studying for his Masters' degree with the VT MSE department.

A. Ramsey Persing

Ramsey graduated with a degree in MSE from Virginia Tech this past May. All four years of college he was involved in Campus Crusade for Christ, a campus ministry. He has decided to devote a few years of his life to serving in this ministry full time. He is currently serving in Thailand sharing his heart with college students in the city of Chiang Mai.

Processing and Characterization of Cr-Cu Alloys through Liquid Phase Sintering for Vacuum Circuit Breakers

Kanwar S. Nalwa

Indian Institute of Technology, Department of Materials & Metallurgical Engineering
Indian Institute of Technology, Kanpur, India 208016

Abstract

Powder metallurgical processing of Cr-Cu has advantages over other processes. Vacuum Cirbuit Breakers are well known as vacuum interrupters (VI). The essential properties required for materials used in VI are high electrical conductivity, good skeleton strength and spark erosion resistance. The effect of sintering temperature, compaction pressure and composition on microstructure, sintered density, mechanical properties (tensile strength, hardness) electrical conductivity and skeleton strength of Cu-Cr contacts was investigated. The effect of microstructure on net-shape consolidation and macrostructure evolution during sintering are also detailed. Liquid phase sintering of Cr-Cu alloys resulted in better density without any significant shape distortion. Tensile strength increased with compaction pressure and chromium content. Higher compaction pressure also led to increased bulk hardness. Electrical conductivity increased with increasing compaction pressure and Cu content.

Keywords: Cr-Cu, liquid phase sintering, vacuum interrupters

1. Introduction

In power delivery engineering, cronium-copper (Cr-Cu) powder metallurgy (P/M) contact materials developed in the past have been widely accepted for medium-voltage, high-current vacuum circuit breakers (VCB) or vacuum interrupters (VI).[1-3] Based on processing, there are two main groups of Cr-Cu contact materials: one is synthesized by powder metallurgy (either by infiltration or sintering), and the other is by vacuum induction melting (VIM) and casting[2] or surface alloying.[3] In spite of other processing routes, powder metallurgical processed Cr-Cu contact materials have more than half share of the VI market. In Cr-Cu, Cu acts as an electric conductor and Cr serves the purpose of giving strength and erosion resistance to the whole material. Cr also initiates the breakdown for the circuit because of its low dielectric strength.[1] Microstructure plays an important role during breakdown.

Even though infiltration (powder metallurgical process) is a well established technique for Cr-Cu vacuum interrupters, it is not economical because the material has to be machined to the net shape. Our objective is to process these materials by a sintering technique, which is economic and saves the time in machining. For our experimental studies, we took two different compositions (wt%) 50Cu-50Cr and 75Cu-25Cr and three different temperatures 1100 °C, 1200 °C and 1400 °C.

2. Powder Characterization

The as-received powder was characterized using scanning electron microscope (SEM) for the morphological studies, as shown in Figure 1. Figure 1a) revealed the presence of pores in the Cu powder which was well understood with the gas atomization process. Figure 1b) shows the chromium powder, which was produced by a reduction process followed by milling. Energy Dispersive X-ray Analysis (EDAX) analysis, to analyze the elemental composition of the powders, shows the presence of oxygen (2.5 wt%) in copper powder (Table 1). The powder size distribution was obtained by using MALVERN Instruments particle size analyzer which works based on the principle of laser diffraction. Apparent density and flow rate of the powders were experimentally measured by using a Hall-flow meter. In addition to the above analysis, specific surface area of powders was measured by using a BET.

2. Experimental Procedure

For the present investigation, copper and chromium powders were supplied by Crompton Greaves Ltd., Mumbai (India). The composition and characteristics of the as-received chromium and copper powders are presented in Table 1. The chromium and copper composites (with 50 and 25 wt% Cr) were prepared by mixing in a Turbula mixer (model: T2C, supplier: Bachoffen, Basel, Switzerland) for 2 hours. The mixed powders were uni-axially compacted at 200 MPa and 600 MPa using a semi-automatic hydraulic press (model: CTM-50, supplier: FIE, Ichalkaranji, India) with a floating die. All the powder mixes were pressed into cylindrical pellets (12 mm diameter and 6 mm height) and tensile bars, as illustrated in Figure 2, to different green densities, which are shown in Table 2. Zinc stearate was used as die wall lubricant during compaction to minimize friction. Sintering was carried out in a $MoSi_2$-heated horizontal tubular furnace (model: OKAY 70T-7, supplier: Bysakh, Kolkata, India). The samples were heated at a constant rate of 5 °C/min in pure hydrogen atmosphere (dew point: -35 °C). The compacts were liquid phase sintered at 1100 °C, 1200 °C and 1400 °C respectively. The sintered density was measured through dimensional measurements and by using Archimedes' principle. The densification response was expressed numerically in terms of densification parameter, which is shown in Equation 1.

$$\text{Densification parameter} = \frac{(\text{sintered density - green density})}{(\text{theoretical density - green density})} \quad (1)$$

The sintered compacts were prepared for metallographic study without using any etching reagent. The microstructural observations and quantitative analysis were carried out using an optical microscope (model: Q5001W, supplier: Leica Imaging System Ltd., Cambridge, UK) attached to a computer. After the metallographic studies, hardness of the composites was measured by using a Vickers hardness tester (supplier: Blue Star, Mumbai, India) at a load of 5 kg using a diamond indenter. Composites were measured for electrical conductivity using a digital electrical conductivity meter (supplier: TechnoFour, Pune, India) with the advantage of the Weidmann-Frenz Law; thermal conductivity of composites was obtained from the electrical conductivity. For measuring the chromium skeleton strength, copper was removed by dissolving the sample in 70% nitric acid (HNO_3). Finally, segregation studies were done by analyzing the change of microstructure throughout the cross section of the composite. Tensile testing of the samples was done by hydraulic assisted automatic tensile testing machine, at 10 kN load and with a head speed of 5 mm/min.

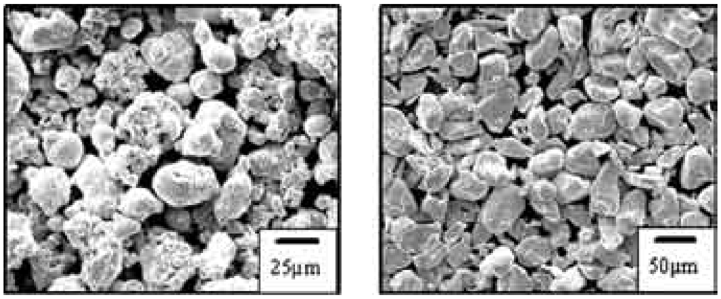

a) b)

Figure 1. Scanning electron micrographs of as-received: a) copper and b) chromium powders

Table 1. Characterization of the powders in as-received condition used in the present study

	Chromium	Copper
Particle size (µm)		
D_{10}	18.9	23
D_{50}	35	52
D_{90}	58	114
Apparent Density (g/cc)	2.91	2.89
Flow rate (s/50g)	47	29
Specific surface area (m^2/g)	0.219	0.145
Theoretical density (g/cc)	7.14	8.9
Melting point (°C)	1907	1083

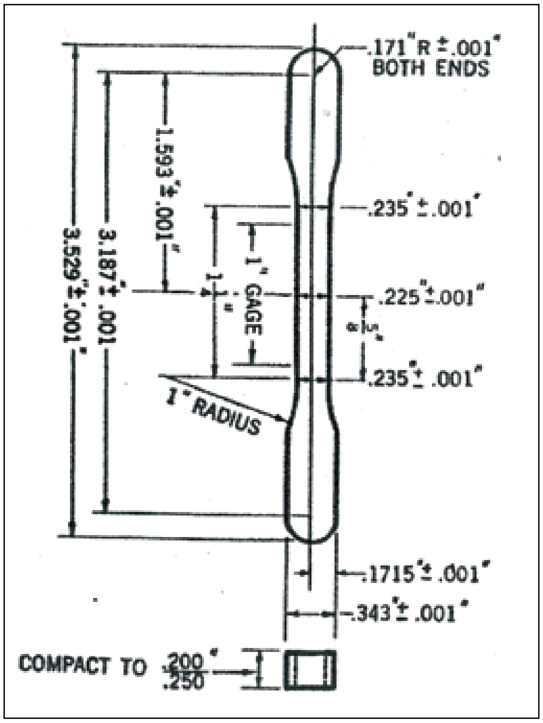

Figure 2. Dimensions of the tensile bar used for present study

3. Results and Discussions

Figure 4 shows the effect of sintering density variation with the compaction pressure and the temperature. Except for the 75Cu-25Cr composite compacted at 600 MPa and sintered at 1400 °C, all other composites show improvement in sintered density with higher compaction pressure and higher sintering temperature. When the composites were compacted at 600 MPa, the number of contacts it makes with the nearby particles is increased. This improves contacting surface area, which makes the diffusion better. There are two mechanisms by which densification occurs: one is capillary induced pore filling by the liquid melt, and the other is dissolution-reprecipitation. In liquid phase sintering, a liquid melt is formed and fills the pores present by capillary action. The grains also dissolve in the liquid melt and reprecipitate as bigger grains, leading to Ostwald ripening. The final sintering response depends on the dominant mechanism by which densification takes place at particular conditions. It is clear from the Cr-Cu phase diagram (Figure 3), that with the increase of temperature from 1100 °C to 1400 °C, the chromium solubility in copper increases. At all temperatures (1100 °C to 1400 °C), the chromium solubility in copper is more than the copper solubility in chromium. If this is not the case, liquid phase sintering does not yield densification. Instead, it results in swelling because more liquid copper goes inside the chromium

Table 2. Green density of various composites compacted at different compaction pressures

Composition	Pressure (MPa)	Green density (g/cc)	Green density (%th.)
50Cu-50Cr	200	5.62	70.64 ± 0.2
	600	7	87.7 ± 0.9
75Cu-25Cr	200	6.09	72.49 ± 0.1
	600	7.58	90.27 ± 0.2

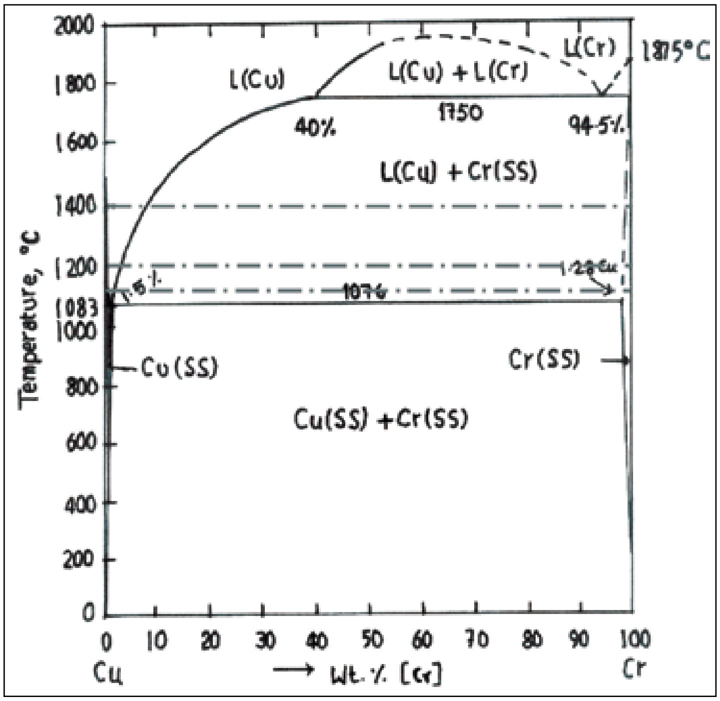

Figure 3. Cr-Cu phase diagram [wt. %]

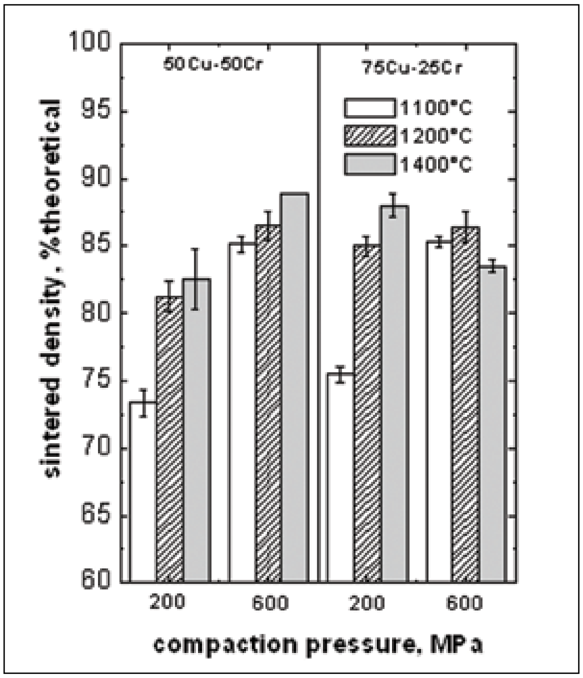

Figure 4. Sintered density at different tempera-

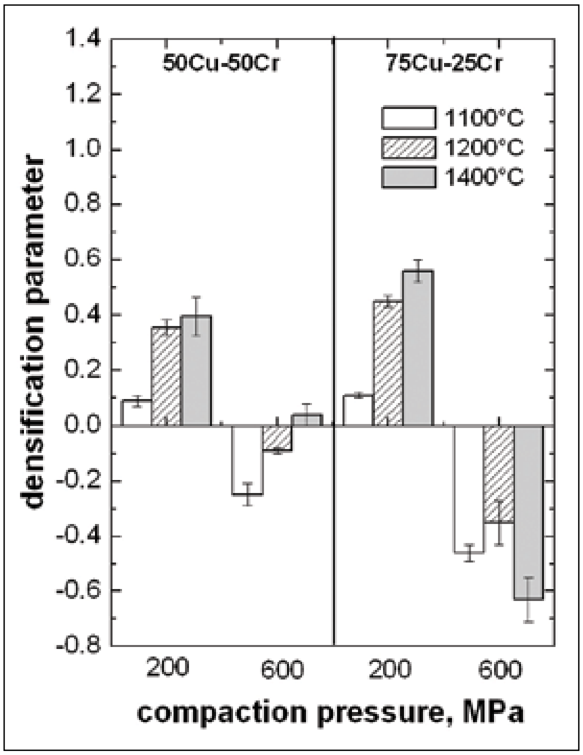

Figure 5. Densification parameter at different temperatures for different Cu-Cr composites

solid solution. When the temperature is lowered, the solubility decreases, and the copper comes out leaving pores in chromium solid solution, hence leading to swelling. The solubility limit of chromium and copper in each other, at different temperatures, is tabulated in Table 3.

At higher temperatures, as the solubility also favors the dissolution-reprecipitation mechanism, it can also contribute to the enhancement of densification. As the copper powder is processed by the gas atomization technique, it inherits some oxygen, which causes the swelling of the compact, mainly when sintering is carried out in a hydrogen atmosphere. Compacts pressed at 200 MPa can easily accommodate the swelling of the powders compared to those pressed at 600 MPa because of a higher volume fraction of pores. This swelling is predominant for the compacts pressed at higher pressures (600 MPa). From Figure 5, it is clearly visible that the compacts pressed at 600 MPa show a negative response to densification. In spite of a negative densification parameter, final sintered density is better at higher sintering temperatures and higher compaction pressures.

Figure 6 shows the optical microstructures of 50Cu-50Cr pressed at 200 MPa, 600 MPa and sintered at different temperatures. It is evident from the figure that increasing the compaction pressure increases the contiguity and connectivity, shown in Figure 6b. This is because of increased number of contacts at higher compaction pressure, which leads to better diffusion through them. Higher sintering temperature leads to the improvement in shape factor (roundness) of chromium grains due to enhanced solubility at higher temperature. When the solubility is high, the sharp edges of the chromium dissolve in copper and reprecipitate at other areas. Because of this high solubility, grain coarsening is observed at higher temperature. This phenomenon is also called Oswald ripening. With the combined effects of higher pressure and higher temperature, the quantity of open porosity decreases and the solid phase becomes more rounded. Figure 7 shows the optical microstructures of 75Cu-25Cr composites. In this case, temperature and pressure have a similar effect as with 50Cu-50Cr. As the copper content is higher in this case, roundness of the chromium grains is improved.

Variation of hardness for different composites sintered at different temperature is shown in Figure 8. Higher compaction pressure results in higher hardness, which could be because of a more contiguous microstructure of chromium phase.

Table 3. Solubility limits of Cu in Cr and Cr in Cu at different temperatures

Temperature (°C)	Cr(Wt.%) in Cu	Cu(Wt.%) in Cr
1100	1	1.2
1200	3.3	1
1400	8	0.68

Figure 9 shows the stress-strain curves for the Cu-Cr composites sintered at 1100 °C. A slight deformation in shape was observed at higher sintering temperatures due to the liquid phase sintering. This deformation makes the samples unsuitable for tensile testing. The measurements obtained from the curves are shown in Table 3. Composites which were pressed at 200 MPa showed less strength and elongation as compared to 600 MPa, due to the lower sintered density and relatively lower contiguous microstructure in the former one. Composites containing higher copper content resulted in high ductility, because the copper phase is softer. Because the chromium content is high in 50Cu-50Cr alloy, it resulted in a higher young's modulus.

Figure 10 shows the electrical conductivity variation of the all the composites. It is clear that, except for the 75Cu-25Cr pressed at higher pressure and sintered at 1400 °C, all the composites follow the same trend as density (Figure 3). When the copper fraction of composite increases, there is an enhancement in

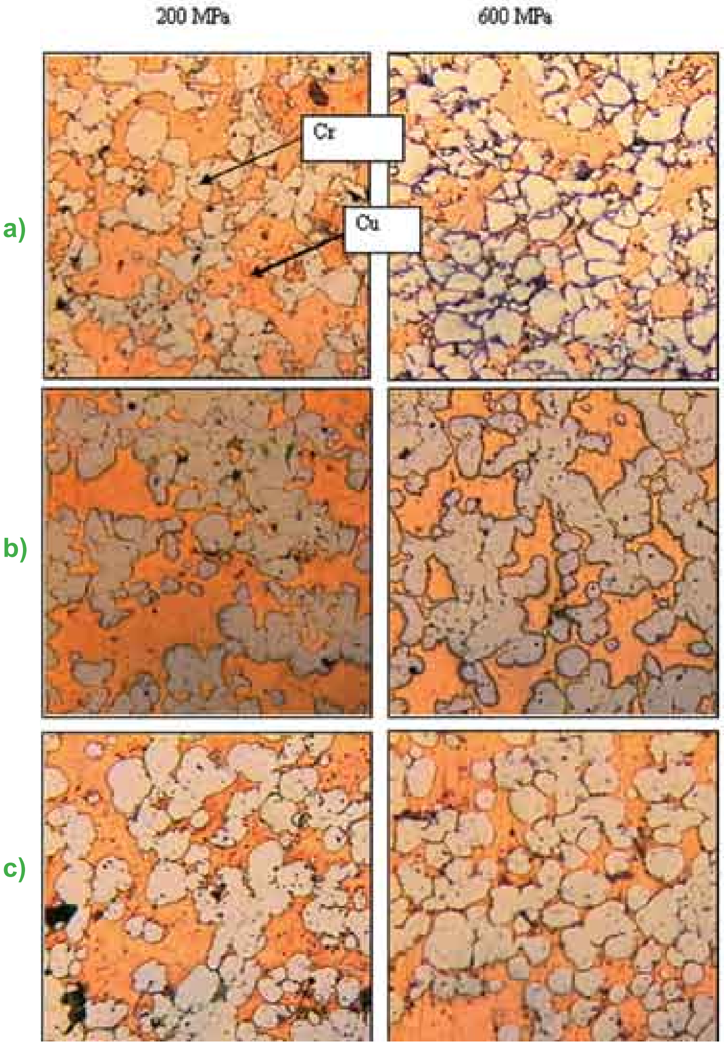

Figure 6. Optical microstructures of 50Cu-50Cr composites sintered at a) 1100 °C, b) 1200 °C and c) 1400 °C which were compacted at 200 MPa (left) 600 MPa (right)

electrical conductivity, because copper is the main constituent contributing to electrical conductivity. As thermal and electrical conductivity are related to the motion of electrons, thermal conductivity can be obtained from the electrical conductivity by using the Wiedemann-FranzLaw.

$$\frac{k}{\sigma} = LT \qquad (1)$$

$$L = \frac{\Pi^2 k^2}{3e^2} \qquad (2)$$

k = Boltzman's constant ($1.38 \times 10^{-23} JK^{-1}$)
e = electron charge (1.6×10^{-19} C)
T = temperature (K)
σ = electrical conductivity ($ohm^{-1}m^{-1}$)
100% IACS = $58*10^6\ \Omega^{-1}m^{-1}$
K = thermal conductivity ($Wm^{-1}k^{-1}$)
L = Lorentz Number (unitless)

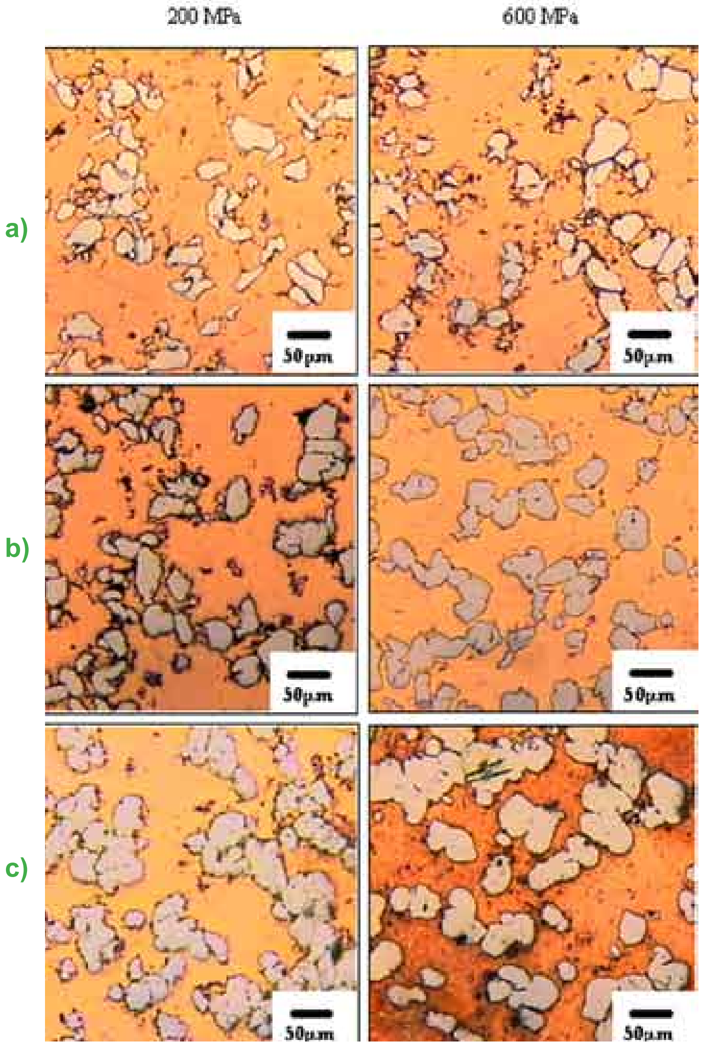

Figure 7. Optical microstructures of 75Cu-25Cr composites sintered at a) 1100 °C, b) 1200 °C and c) 1400 °C which were compacted at 200 MPa (left) 600 MPa (right).

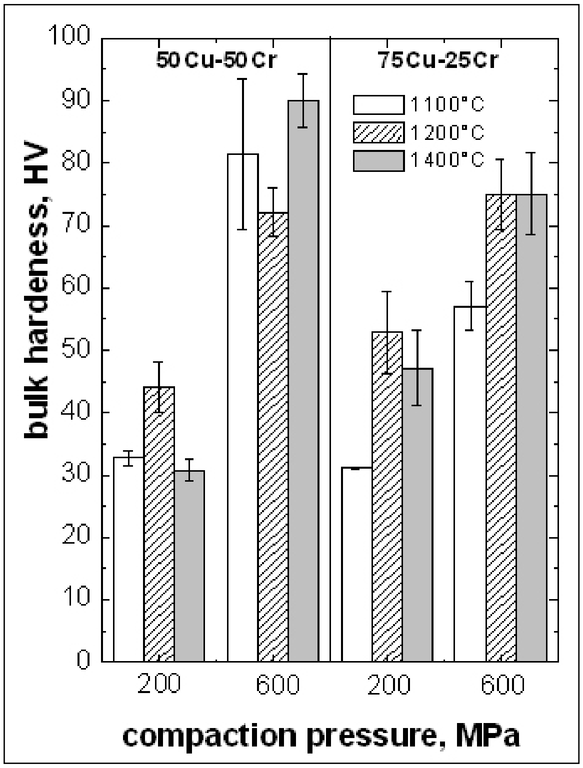

Figure 8. Optical microstructures of 75Cu-25Cr composites sintered at a) 1100 °C b) 1200 °C and c) 1400 °C which were compacted at 200 MPa (left) 600 MPa (right)

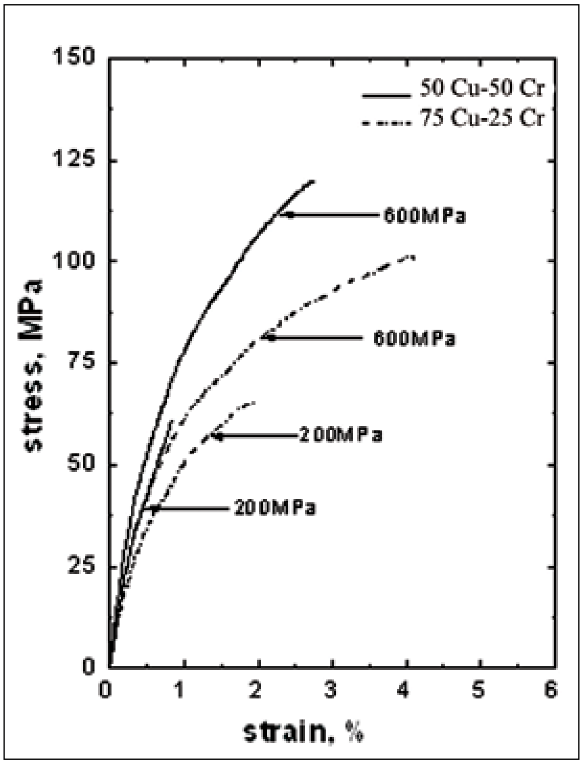

Figure 9. Stress-Strain curves for different Cu-Cr composites sintered at 1100 °C

From the above formulas (Equation 2 and 3), it is well understood that thermal conductivity is directly proportional to electrical conductivity. The obtained thermal conductivity is shown in Figure 11.

4. Conclusions

For optimized sintering, the compaction pressure and the sintering temperature should be high so that it leads to higher densification. However, too high sintering temperatures can lead to shape distortion, segregation, and grain growth. Also, high copper content leads to higher electrical conductivity but lower skeleton strength, so the proportion of copper and chromium should be determined in function of desirable properties. Below is a summary of how properties varied with change in processing conditions:

- Liquid phase sintering of Cr-Cu alloys resulted in better density without any significant shape distortion
- Sintered density increased as sintering temperature increased
- Tensile strength increased with compaction pressure and chromium content
- Bulk hardness increased with compaction pressure
- With increasing compaction pressure and copper content, electrical conductivity increased

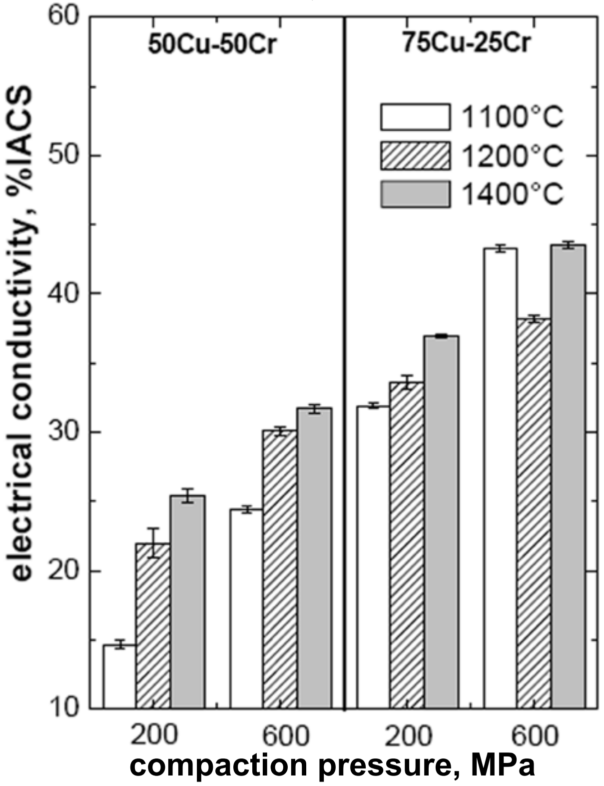

Figure 10. Electrical conductivity variation for different Cu-Cr composites at different temperatures

Acknowledgements

The author is thankful to Prof. A. Upadhyaya for his guidance and encouragement. The assistance provided by Mr. E.R. Tagore in experiments is also gratefully acknowledged. This work was financially supported by Corporate R&D Center, Crompton Greaves Ltd, Mumbai, India.

References

[1] Ding, Bingjun; Yang, Zhimao; Wang, Xiaotian. Influence of Microstructure on Dielectric Strength of Cu-Cr Contact Materials in a Vacuum. *IEEE transactions on Components, Packaging, and Manufacturing Technology-Part A*, **1996**, *19*(1), 73-81.

[2] Temborius, S.; Lindmayer, M.; Gentsch, D. Switching Behavior of Different Contact Materials for Vacuum Interrupters under Load Switching Conditions. *IEEE 19th International Symposium on Discharges and Electrical Insulation in Vacuum-Xi'an*, **2000**, *2*, 519-523.

[3] Li, Wangpei; Thomas, Robert L.; Smith, R. Kirkland. Effects of Cr Content on the Interruption Ability of Cu-Cr Contact Materials. *IEEE Transactions on Plasma Science*, **2001**, *29*(5), 744-748.

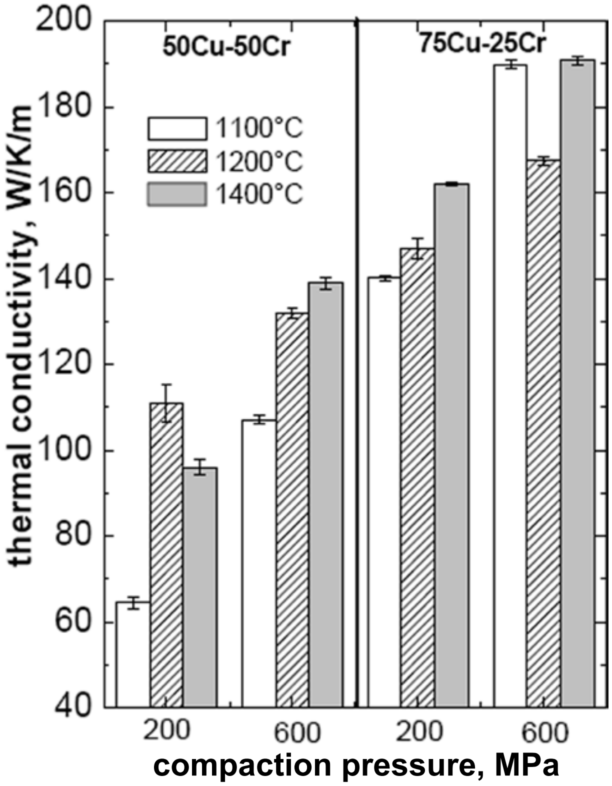

Figure 11. Thermal conductivity variation for different Cu-Cr composites at different temperatures

Reaction Synthesis of TiAl-TiB_2 Metal Matrix Composites

David Berry and Michael Wooddell

Virginia Polytechnic Institute and State University, Department of Materials Science and Engineering
Blacksburg, VA 24061

Abstract

The objective of this study was to define and develop measurable processing parameters to guide the synthesis, design and characterization of reaction-synthesized TiAl-TiB_2 composites. Measurements of energy release during the high temperature self propagating reaction between Ti, Al, and B were used to determine the effects of environment (air or helium), atomic percent Al, and volume percent TiB_2 on the reactivity of the sample. Experimental results were compared to theoretical models developed using published thermodynamic data in order to inspect the adiabatic nature of the reaction. The compositions tested were those of Ti-50Al + 30, 40 and 50 volume percent TiB_2, Ti-43Al + 30, 40 and 50 volume percent TiB_2, and Ti-35Al + 30, 40 and 50 volume percent TiB_2. Experimental results showed that compositions tested in a helium atmosphere provided inconsistent results in both ignition temperature and heat of reaction that were counterintuitive to trends predicted by the theoretical models. Experimental results of compositions tested in an air atmosphere provided better consistency in ignition temperature, along with considerably higher heats of reaction which were much closer to predicted values. These results qualitatively followed the trends produced by the theoretical models.

Keywords: Intermetallic matrix composites, self-propagating high temperature synthesis, titanium diboride, titanium aluminde

1. Introduction

The properties of particulate reinforced metal matrix composites rely heavily on the nature of the interface between the reinforcement and matrix materials, as well as the size, geometry, and volume fraction of the reinforcing phase. Traditional processing methods such as casting, powder metallurgy, and mechanical alloying have several drawbacks that encourage the use of non-conventional processing techniques. In traditional processing schemes, the reinforcing phase is added directly to the molten or powder material, leading to surface contamination and poor wettability between matrix and reinforcing phases. This weak particle matrix interface ultimately leads to poor mechanical properties.[1] These problems have been combated through the development of alternative processing schemes such as combustion synthesis, also known as self-propagating high-temperature synthesis (SHS).

1.1 Combustion Synthesis (SHS)

Combustion synthesis involves heating a green compact of elemental or pre-alloyed powder material to an "ignition" temperature that initiates a highly exothermic reaction that can reach temperatures in excess of 2700 K. Subsequently, the heat evolved provides the thermal energy needed to react the remaining elemental powder. The reaction proceed as a self-propagating reaction front, hence the term self-propagating high temperature synthesis.[1,2] In the case of intermetallic matrix composites (IMMC), combustion synthesis is known as an in situ procedure in which the reinforcement phase is synthesized in situ by the self propagating reaction.[1] SHS offers several practical and theoretical advantages over conventional processing because of the thermodynamically stable matrix/reinforcement interfaces that form during the process.[2] However, despite this obvious advantage, SHS still has drawbacks that must be addressed in order to fully utilize the potential of the reaction. In particular, in many cases of combustion synthesis, the reaction between individual components is hard to control due to the highly exothermic nature of the process as well as rapid reaction rates.[1] This study will begin to address the issue by correlating reactant products to synthesis parameters which will allow reaction design regardless of speed or exothermicity.

1.2 Factors Affecting Combustion Synthesis and Composite Microstructure

As mentioned, the size, shape and distribution of reinforcing phases within a composite microstructure significantly influence its mechanical properties. When IMMC's are produced using combustion synthesis, the above factors are typically related to the reaction parameters such as the amount of heat evolved during the reaction as well as the highest temperature achieved. Several studies have identified key variables, including heating method/rate, particle size, elemental ratios, porosity, and environment, that affect the heat of reaction, the maximum temperature reached, and ultimately the mechanical properties of the composite.[1-5] Kampe and Martin et al. have studied the TiB_2/TiAl system, where both the reinforcing and matrix phases contribute to the exothermicity of the reaction. Their study examined the effects of alloy composition, (volume percent of TiB_2), on the resulting microstructure and adiabatic temperature (highest temperature reached during reaction). However they did not examine fully the correlation between reaction parameters and the resulting microstructure and mechanical properties. Kampe and Martin explored the effects of volume percent of TiB_2 on the theoretical adiabatic temperature and heats of reaction. They concluded that the diameter of the TiB_2 particulates increased with the nominal formulated percentage. From analysis of the predicted adiabatic temperature, they suggest that the larger TiB_2 particles resulted from the higher temperatures associated with the formation of higher volume fractions of the exothermic TiB_2 during synthesis.[2]

1.3 Research Objectives

Based on the previous research of Kampe and Martin, this project sought to define and develop measurable processing parameters which can serve to guide the synthesis, design and characterization of reaction-synthesized TiAl-TiB_2. Specifically, measurements of energy release during synthesis reactions will provide an independent means to characterize the influence of atomic percent Al in the matrix, volume percent of TiB_2 reinforcement, and environment on the reactivity and the microstructural characteristics of the final product. The specific matrix compositions tested were those of Ti-34Al, Ti-43Al, and Ti-50Al with volume percent of TiB_2 at 30, 40 and 50 volume percent. The reaction was studied in both helium and air.

1.4 Theoretical Heat of Reaction and Adiabatic Temperature

A theoretical model was developed to determine the expected heats of reaction and adiabatic temperatures as a function of atomic percent Al and volume percent TiB_2, using published thermodynamic data and incorporating all phase transitions for both reactants and products. The adiabatic temperature is

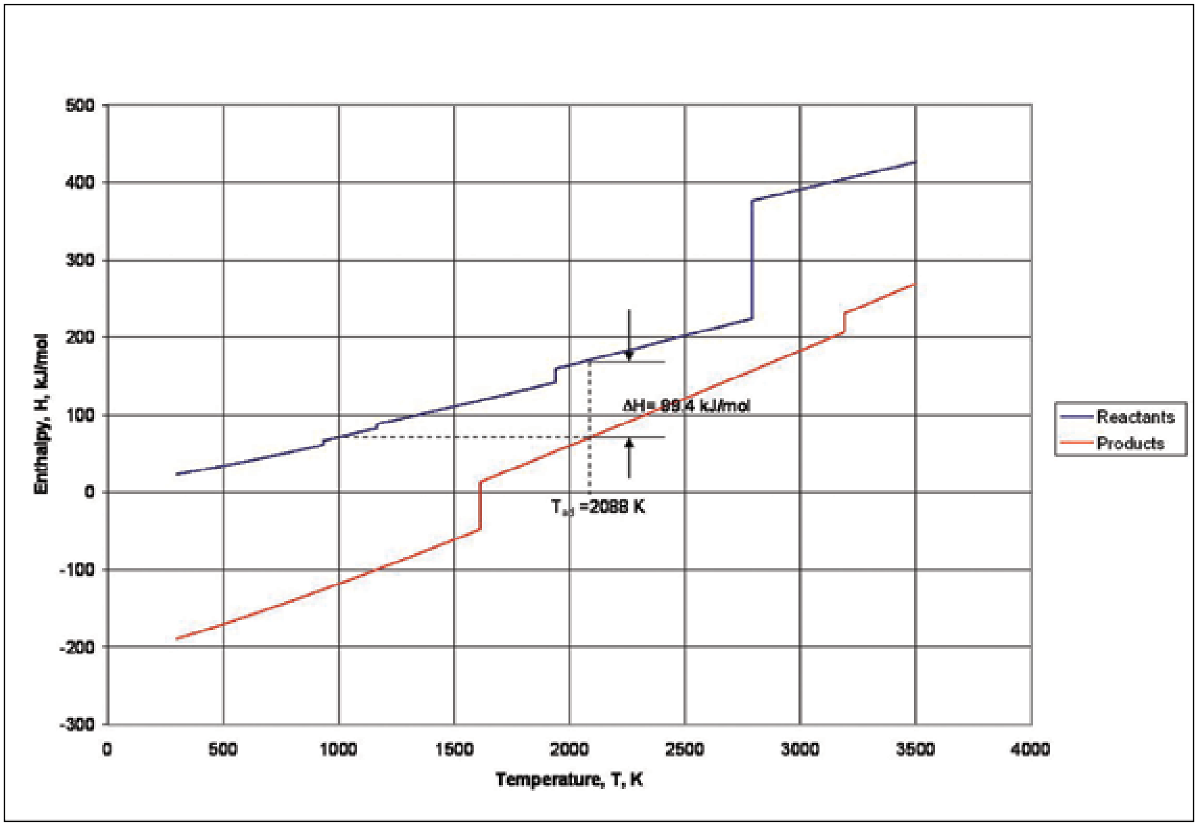

Figure 1. Theoretical enthalpy vs. temperature for Ti-34Al + 20 volume percent TiB_2

defined as the difference in the heat of products and heat of reactants measured an ignition temperature. In the case of the Ti-Al-B system, it is assumed to be 1000 K, or approximately the melting point of aluminum. It is thus assumed that the all the heat generated by the reaction acts to increase the temperature of the remaining unreacted material. The heat of reaction is taken as the difference in reactant and product enthalpies at the adiabatic temperature. Figure 1 graphically depicts the definitions of both reaction enthalpy and adiabatic temperature.

Table 1. Constituent amounts for each sample composition

Composition	TiB2 in Vol. %	Ti (g)	Al (g)	B(g)
Ti-50 Al	30	6.5680	2.3526	1.0794
Ti-50 Al	40	6.6201	1.9723	1.4076
Ti-50 Al	50	6.6699	1.6084	1.7218
Ti-43Al	30	6.9746	1.9699	1.0555
Ti-43Al	40	6.9610	1.6575	1.3815
Ti-43Al	50	6.9482	1.3562	1.6957
Ti-34Al	30	7.4667	1.5066	1.0268
Ti-34Al	40	7.3774	1.2730	1.3496
Ti-34Al	50	7.2904	1.0461	1.6635

2. Procedure

2.1 Powder Constituent Calculations

The elemental constituent powders needed for each composition were titanium, aluminum and boron. The titanium powder used was >325 mesh, the aluminum powder was >100 mesh and the boron was >100 mesh. The amount of each varies based on the target matrix and reinforcement volumes. Three target compositions of α2-phase Ti_3Al and γ-phase TiAl were chosen. Each of the three compositions was chosen based on the modeled thermodynamic transitions and attempted to represent the full α2+ γ phase of the Ti-Al phase diagram. Of these three matrix variations the volume fraction of reinforcement loading was varied between 30 and 50 volume percent. The reinforcement phase is TiB_2.

A previous iteration of a Matlab program was utilized to aid in quickly determining the matrix and reinforcement weight percents and volume percents. The amounts listed in Table 1 are based on a 10 gram batch of sample.

2.2 Sample Preparation

To optimize the thermal analysis measurement, each composition was cold compacted before testing. The sample was pressed to 20 Ksi with a 0.5 inch diameter compaction die. The optimum differential scanning calorimetry (DSC) sample weight was 10 mg.

2.3 Thermal Analysis

Crucibles made of alumina were used with the Netszch Simultaneous Thermal Analysis system. Each sample was placed into an alumina crucible, covered and loaded into the Netszch DSC. Tests were run in both helium and air. The helium

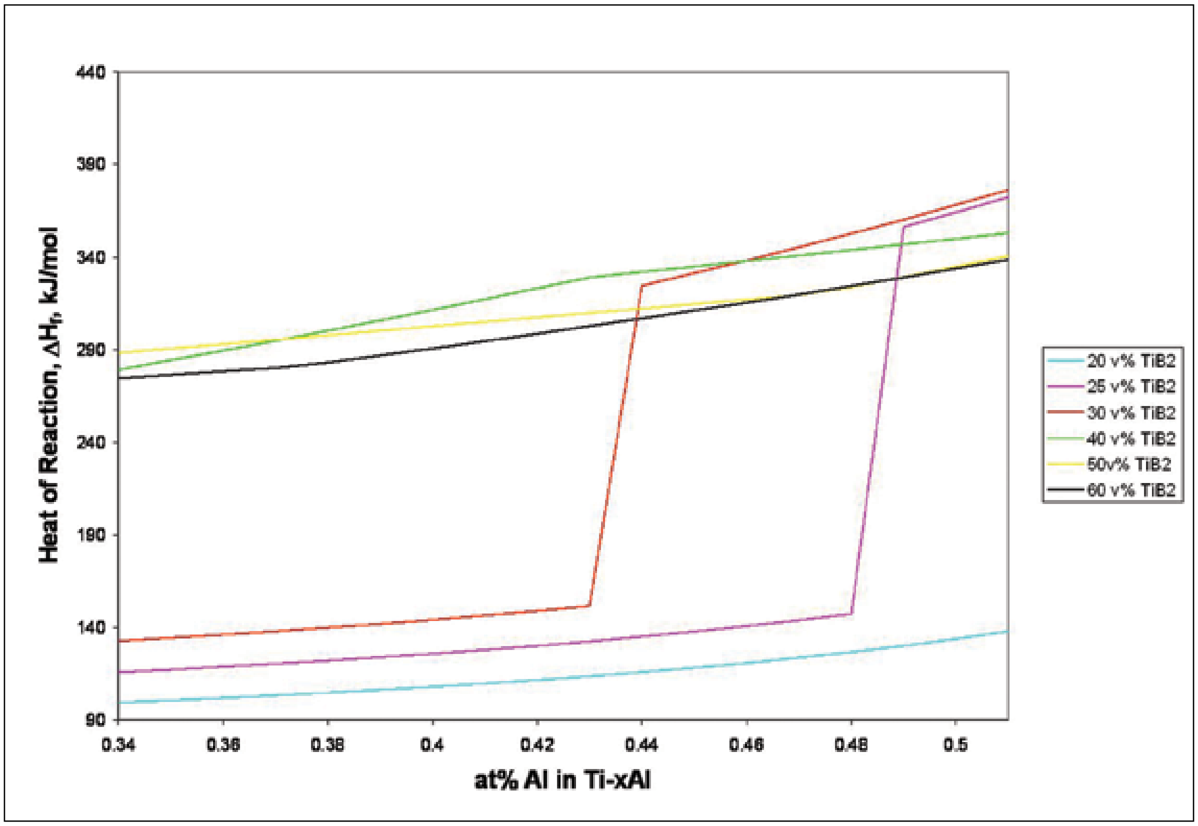

Figure 2. Theoretical heat of reaction vs. atomic percent Al

temperature profile starts at 40 ºC and ramps to 1050 ºC at 40 ºC/min. However, the tests run in oxygen/nitrogen mixture need to be heated to 1200 ºC at 40 ºC/min.

3. Results and Discussion

The DSC results showed that the compositions tested in the helium atmosphere produced large variations in heat of reaction and ignition temperature, as well as values of heat of reaction that were an order of magnitude smaller than those predicted by theoretical models. Those compositions tested in the air atmosphere produced results that were much more repeatable heats of reaction and ignition temperature, as well as values of heat of reaction that were on the same order of magnitude as those predicted by the theoretical models.

3.1. Theoretical Model Results

The results from the theoretical models were used to determine the compositions to be tested experimentally based on variations in predicted reaction characteristics. Theoretically, as shown in Figure 2, the heat of reaction varies significantly with atomic percent Al and volume percent TiB_2.

As shown in Figure 2, the amount of heat evolved increases with increasing amounts of both Al in the matrix and volume percent of TiB_2 in the composite. Also, there is a large jump in the heats evolved for all atomic percentages of Al. This large jump occurs because the reaction reaches the vaporization temperature of Al. The 50 atomic percent of Al demonstrates this large jump in heat evolved much sooner than the 34 and 43 atomic percentages of Al. This shows that, theoretically, increasing the atomic percent of Al increase the reactivity of the system.

As with the heat of reaction, the adiabatic temperature also increases with increasing amounts of Al in the matrix and volume percent of TiB_2 in the composite, as shown in Figure 3. Both the 34 and 43 atomic percentages of Al show a plateau region in adiabatic temperature. In this region, T_{ad} equals the melting temperature of TiB_2, or 3193 K

3.2 Differential Scanning Calorimetry Results

3.2.1 Helium Atmosphere

The DSC results in the helium atmosphere demonstrated a significant amount of scatter in both heat of reaction and ignition temperature for all samples tested, as exemplified by the three DSC traces of the Ti-34Al +30 volume percent TiB_2 composition in Figure 4. In this trace, endothermic reactions appear as upward peaks, while exothermic reactions appear as downward peaks.

Figure 4 presents DSC traces that demonstrate representative variation in ignition temperature and heat of reaction. The first endothermic peaks represent that of the melting of aluminum. These peaks were found to be very consistent in heat of fusion and melting temperature for all compositions tested, indicating

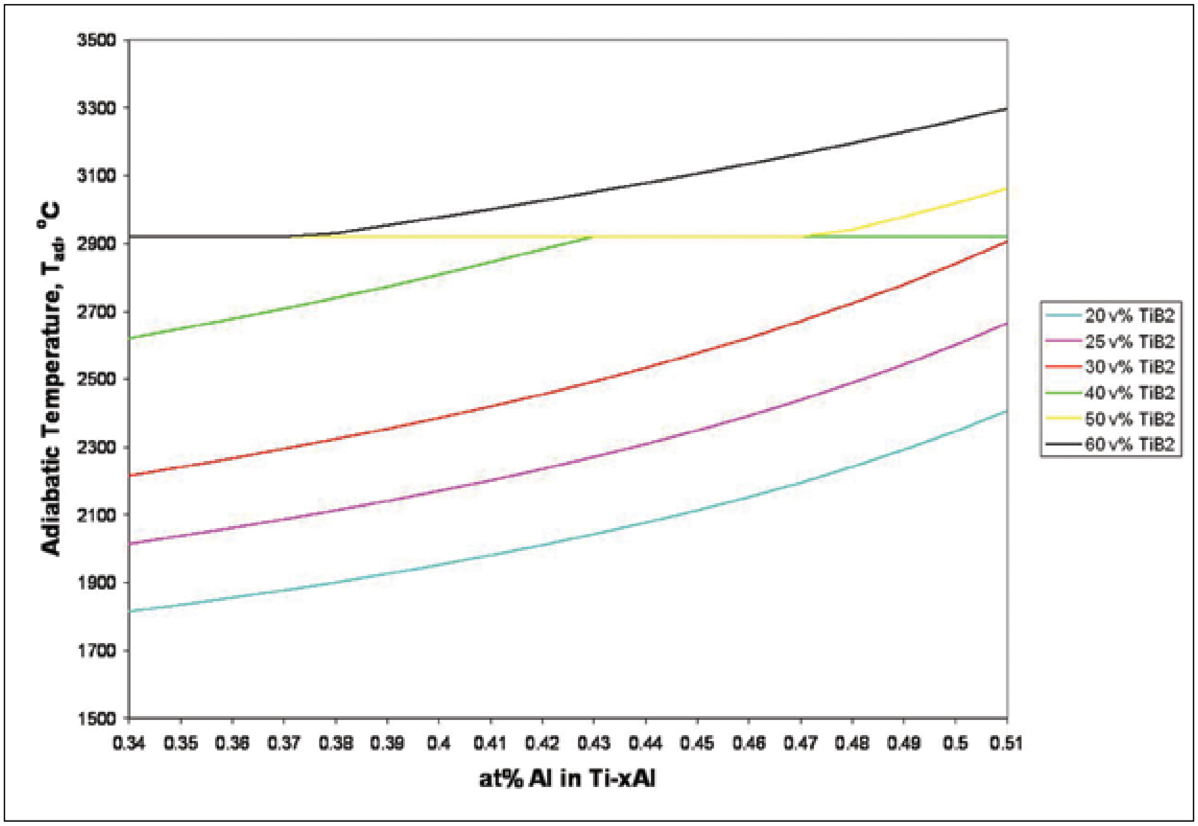

Figure 3. Theoretical adiabatic temperature vs. atomic percent Al

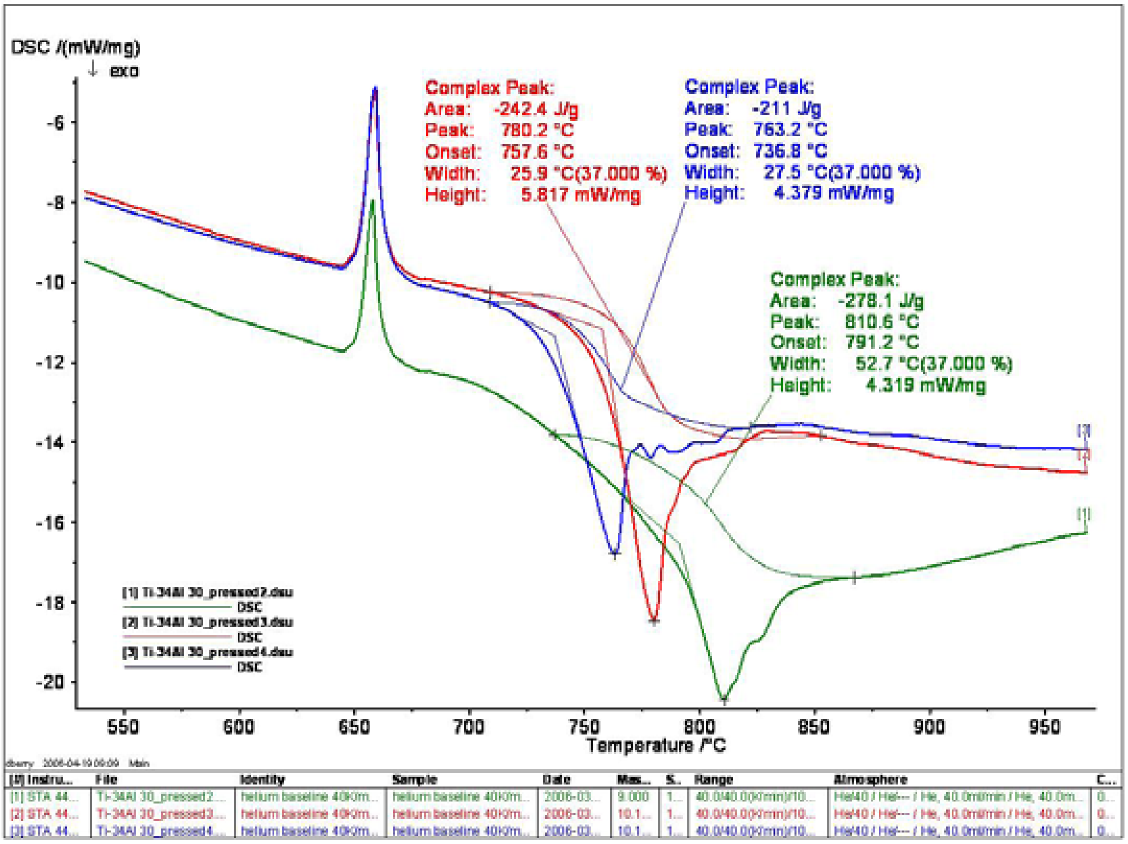

[#] Instru...	File	Identity	Sample	Date	Mas...	S..	Range	Atmosphere	C...
[1] STA 44...	Ti-34Al 30_pressed2...	helium baseline 40K/m...	helium baseline 40K/m...	2006-03...	9.000	1...	40.0/40.0(K/min)/10...	He/40 / He/--- / He, 40.0ml/min / He, 40.0m...	0...
[2] STA 44...	Ti-34Al 30_pressed3...	helium baseline 40K/m...	helium baseline 40K/m...	2006-03...	10.1...	1...	40.0/40.0(K/min)/10...	He/40 / He/--- / He, 40.0ml/min / He, 40.0m...	0...
[3] STA 44...	Ti-34Al 30_pressed4...	helium baseline 40K/m...	helium baseline 40K/m...	2006-03...	10.1...	1...	40.0/40.0(K/min)/10...	He/40 / He/--- / He, 40.0ml/min / He, 40.0m...	0...

Figure 4. DSC trace of Ti-34Al + 30 volume percent TiB_2

that the variations in the amount of aluminum did not affect when or how much of, the aluminum melted. The exothermic peaks in Figure 4, however, showed large variation in both ignition temperature and heat of reaction. Two of the peaks also demonstrated oscillations near the end of the exotherm. These could possibly indicate several small reactions occurring after the initial heat evolution. The DSC results for all compositions tested in helium are presented in Table 2.

Table 2. DSC results in Helium

Atomic % Al	Volume % TiB_2	run 1 (J/g)	run 2 (J/g)	run 3 (J/g)	run 4 (J/g)	Avg. heat J/g	Standard Deviation in % of Avg.
50	30	227.3	310.9	312.7		283.63	17.20
50	40	112.1	270.6	186.0		189.57	41.84
50	50	64.8	173.1	207.0	132.8	144.43	42.33
43	30	289.2	231.9	310.2		277.10	14.63
43	40	114.3	197.8	260.2		190.77	38.37
43	50	313.83	124.4	129.3		189.18	57.08
34	30	278.1	242.2	211.0		243.77	13.78
34	40	151.8	131.0	149.1	112.6	136.13	13.37
34	50	91.58	102.3	1063.3		419.06	133.14

The data presented in Table 2 again shows the large variation in heats of reaction for all the compositions. These variations may result from density and composition variations within each sample material. Also, many of the average heats of reaction, with their standard deviations, overlap one another, thus making it impossible to determine the effects of varying compositional ratios on the reactivity of the material.

The resulting test of Ti-34Al + 50 volume percent TiB_2 shown in Figure 5 (green line), demonstrated a large increase in the exothermicity of that reaction. Also, two large exotherms were noted as opposed to small oscillatory reactions near the end of the exotherm.

3.2.2 Air Atmosphere

Compositions of Ti-34Al + 30 and 50 volume percent TiB_2, as well as Ti-50Al + 30 and 50 volume percent TiB_2 were tested in an air atmosphere consisting of 80%

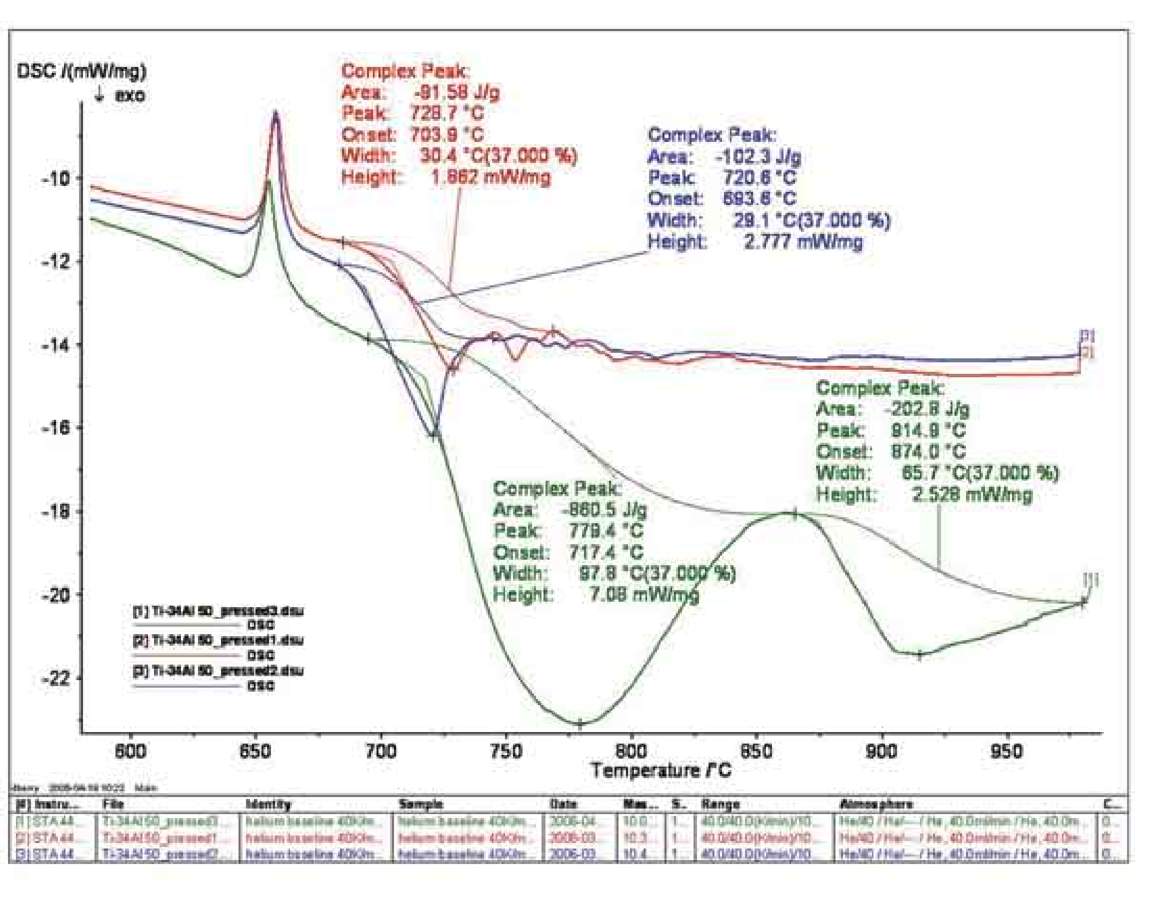

Figure 5. DSC trace of Ti-34Al + 50 volume percent TiB_2

nitrogen and 20% oxygen. The results of the DSC tests in air proved much more repeatable, and also demonstrated reaction exotherms that more closely resemble those expected from the theoretical models. For example, Figure 6 presents the DSC trace of Ti-34Al + 30 volume percent TiB_2

This graph illustrates a desirable and repeatable correlation between two samples of identical composition. The aluminum melting endotherm is still consistent in quantity and onset yet the reaction has three distinct exothermic reactions instead of the one large exotherm shown in tests with a helium atmosphere. Table 3 summarizes the results of the DSC tests in air atmosphere and tabulates the heats from all three reactions as indicated in Figure 6.

The average heat of reaction for each matrix composition and loading scenario in air are much greater than heats for similar compositions tested in helium. The standard deviation for these samples when compared to the average heat evolved is a much smaller ratio than shown for data in the helium atmosphere. The standard deviation for the Ti-50Al+50 volume percent TiB_2 in helium is 42.33% of the average heat compared to a value of 4.33% for the same composition tested in air.

Each of the samples tested in the air atmosphere revealed three reaction isotherms and an absence of oscillations. The placement of the isotherms for air samples changed with an increasing atomic percent of aluminum. An example DSC trace of a matrix composition with 50 at% Al is shown in Figure 7.

The arrangement of the reaction has shifted to the left (down in temperature) as the atomic percent of aluminum in the matrix increases. Three reactions still occur and the respective heats are tabulated as before with the first reaction and ignition temperature taken from the first noticeable exothermic peak. This exothermic reaction consumes the endothermic melt of aluminum, but the onset of aluminum melt remains consistent. Although the reaction timing has changed with the added aluminum in the matrix composition, the ignition temperatures remain constant with matrix composition and reinforcement percentage as shown in Table 4. The shift in onset temperature for these reactions is only a few degrees compared to the discrepancies as large as 50 ºC for similar compositions tested in the helium environment.

3.3 Experimental Theoretical Comparisons

3.3.1 Helium Results vs. Theoretical

It is difficult to objectively compare the theoretical results and the experimental results produced from testing in a helium atmosphere, because of the scattering of data points and the uncertainty associated with pellet compact composition and density. In addition, the theoretical model was based on the

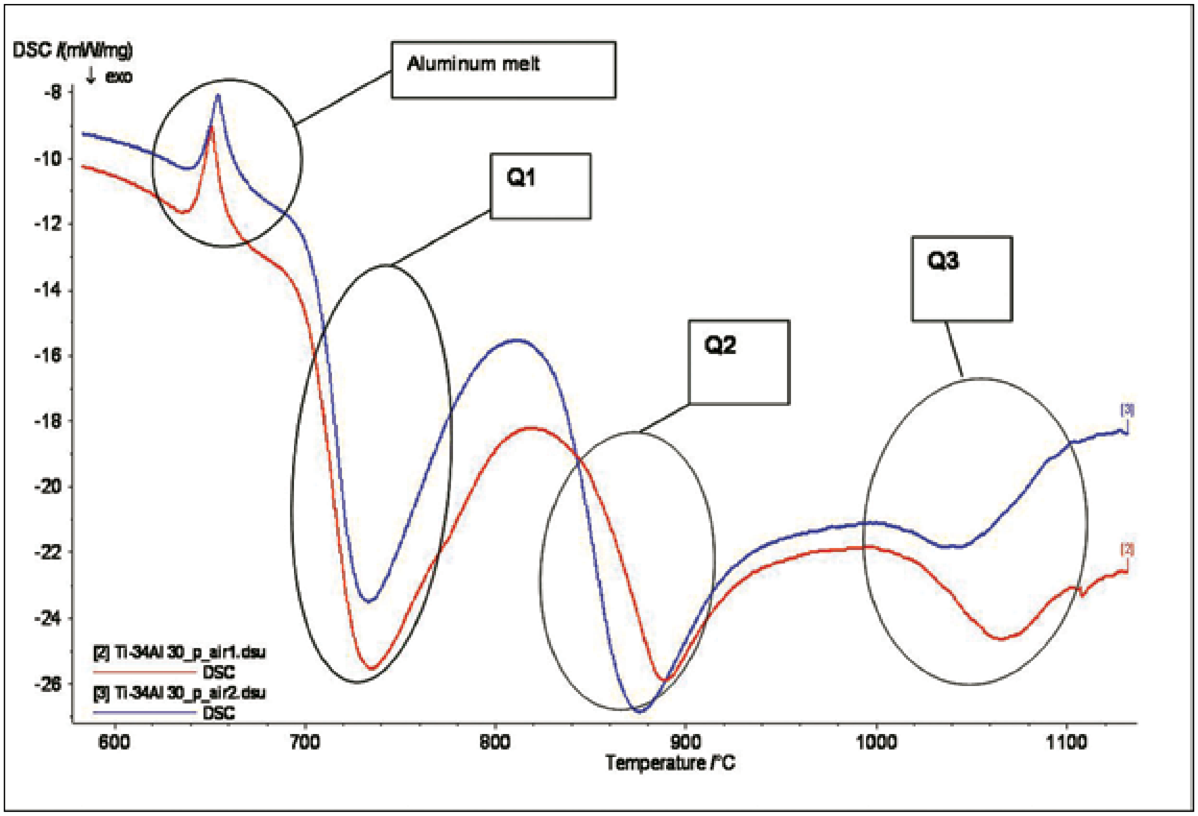

Figure 6. DSC trace for Ti-34 + 30 volume percent TiB_2 tested in air

assumption of 1 mole of products, and adiabatic conditions during the reaction and we have not proven those conditions occured. Comparing the theoretical and experimental values of heat of reaction as a function of atomic percent Al, as shown in Figure 8, reveals the data is an order of magnitude apart.

Also, neither the 34 nor 43 atomic percent Al follows the trend that was present in the theoretical model. However, the 50 atomic percent Al data does follow a downward trend similar to the same downward trend in the model

3.3.2 Air Results vs. Theoretical

The values obtained from the air atmosphere reactions also cannot be compared directly to the values determined by the theoretical model for several reasons. First, the actual reaction products found in the air reacted compositions can not be determined without further analysis, such as x-ray diffraction, electron discharge spectroscopy, or other elemental/compound characterization techniques. Also, the theoretical models were based on the assumption that no heat was lost to surroundings and that reaction ignited when the aluminum melted as we see did not happen to some compositions tested in air. However, it was recognized that the values of heat of reaction obtained from the air atmosphere experiments are an order of magnitude larger than those found using the helium atmosphere, thus closer to the theoretical values. This suggests that the reaction occurred at a greater fraction of its potential in air.

Table 3. DSC reaction heats for compositions tested in air atmosphere

Atomic % Al	Vol % TiB_2	Experiment 1 (J/g)			Total heat (J/g)	Experiment 2 (J/g)			Total heat (J/g)	Avg. heat (J/g)	standard deviation in % of avg.
		Q 1	Q 2	Q3	Q total	Q 1	Q 2	Q3	Q total		
50	30	1074.0	1375.0	457.9	2906.9	1415.0	959.6	278.0	2652.6	2287.0	7.86
50	50	1854.0	506.1	90.1	2450.2	1525.0	800.3	269.7	2595.0	2365.1	4.33
34	30	935.5	566.8	202.3	1704.6	807.5	1008.0	156.4	1971.9	1795.0	10.53
34	50	1786.0	365.8	270.0	2421.8	1535.0	350.2	184.1	2069.3	2250.1	11.08

Table 4. DSC ignition temperatures for compositions tested in air atmosphere

Atomic % Al	Vol % TiB2	Experiment 1 Ignition Temperature °C	Experiment 2 Ignition Temperature °C
50	30	542.1	555.10
50	50	544.4	540.90
34	30	702.6	705.60
34	50	708.2	707.00

4. Conclusion

4.1 Testing Repeatability and Theoretical Correlation

Results from the DSC testing machine indicate that a helium atmosphere provides inconsistent results in both ignition temperature and heat of reaction that are counterintuitive to trends predicted by the theoretical models. This inconsistency along with very large discrepancies between the theoretical and measured heats of reaction suggests that reactions are being suppressed by the helium atmosphere, and not allowed to go to completion. On the other hand, results from the DSC in an air atmosphere provided better consistency in ignition temperature, along with considerably higher heats of reaction which were much closer to predicted values. Also, these results qualitatively followed the trends produced by the theoretical models. However, more data needs to be gathered to verify these findings.

4.2 Reaction Oscillation/Propagation

Both helium and air atmospheres produced reaction curves that demonstrated multiple exothermic reactions. The exothermic peaks in the helium atmosphere appeared as small oscillations in the DCS trace, indicating that the reaction was short lived. In comparison the exothermic peaks in the air atmosphere showed pronounced separation and larger/longer oscillation peaks, indicating that the reactions were slower and or allowed to go to completion.

5. Future Work

The unexpected discrepancy arising from the change in atmosphere during testing leads to a need for more characterization of the reaction kinetics and the evolution of final product. To accurately determine a reliable trend, more data needs to be taken for each matrix composition and reinforcement percentage already tested in the air atmosphere. Although two samples of each composition resulted in uniform reaction parameters and repeatable ignition temperatures, more tests should be taken to establish a uniform distribution and narrow the standard deviation. In addition, different matrix compositions should be tested to define a trend in the shifting ignition temperature.

Finally, due to the oxidizing atmosphere, the product of the reaction is questionable. In theoretical models the product was assumed to be solely a composite of matrix material, Ti_3Al and TiAl, and its reinforcement phase, TiB_2. Because the sample exhibits oxidation in the air atmosphere, the product may con-

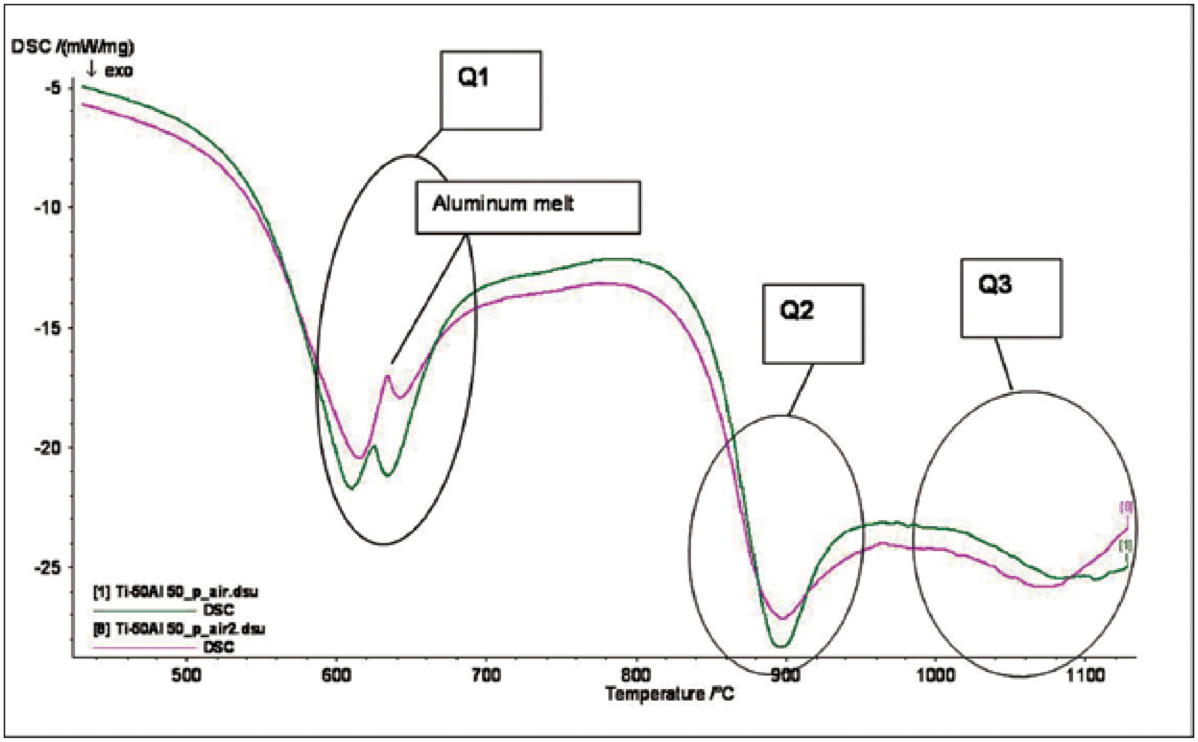

Figure 7. DSC trace of Ti-50Al + 50 volume percent TiB_2 in air atmosphere

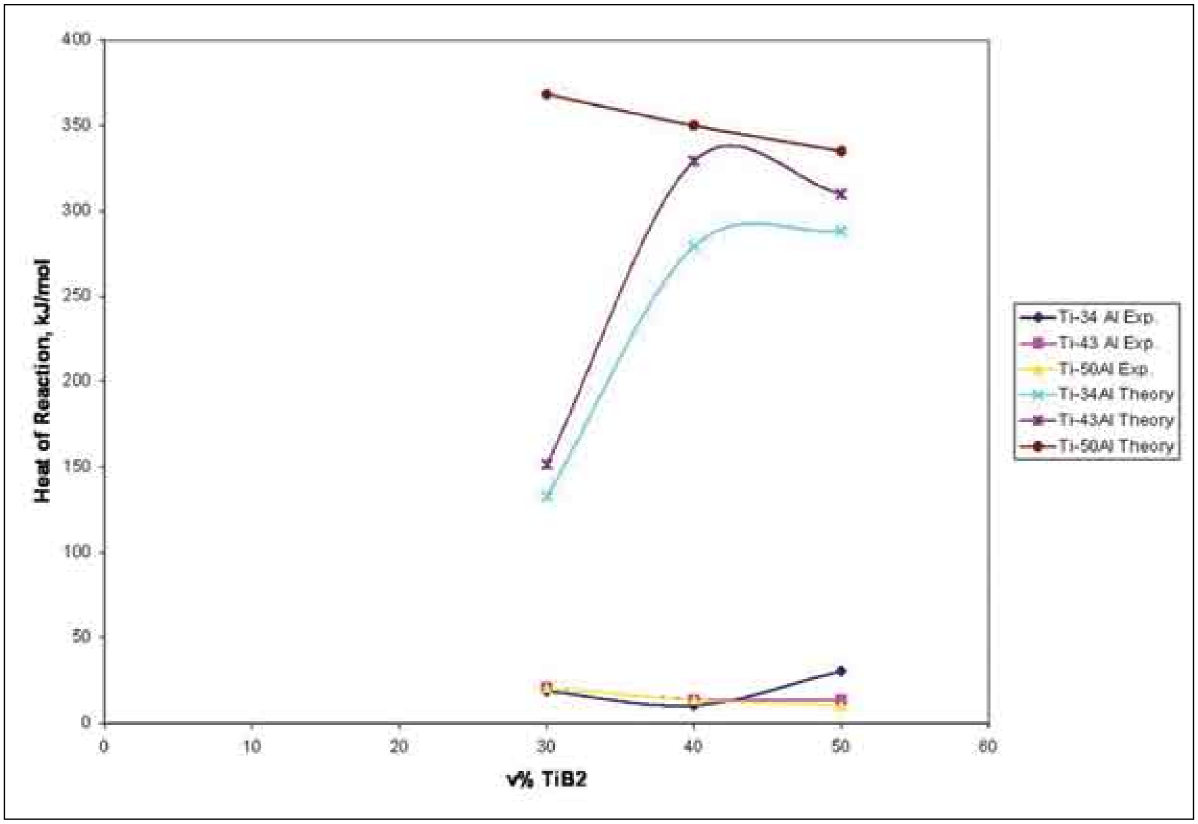

Figure 8. Comparison of theoretical variations of reinforcement with experimental variations of reinforcement

tain a percentage of alumina, Al_2O_3. This was not considered in earlier models and without proper molecular weight values, the conversion from DSC data in J/g to J/mol is inaccurate and a direct comparison would be invalid.

Overall characterization on intermediate products should be done using X-ray powder diffraction and SEM. X-ray data can be used to confirm constituents at phases of reaction completion. SEM analysis can confirm structure and size of phases and may allow further insight into formation of final reinforcement phases. The presence of three separate reaction fronts should allow for these characterization techniques at each phase of reaction to be analyzed.

Lastly, care should be taken in sample preparation. Possible sources of error may occur in sampling of blended powders. Given the small amount of sample needed for DSC testing, an accurate representation of the overall constituent powders may not be present. To improve testing scenarios, samples should be pressed to near testing weights and care should be taken to mix only small batches of material with accurate scales to insure proper ratios.

Acknowledgements

We would like to thank Dr. Stephen Kampe for his guidance and support throughout the course of this project. We would also like to thank Elizabeth Jeffers and Dr. Jeff Schultz for their time and input.

Reference

[1] Kwon, Yong-Jai and Makoto Kobashi. Fabrication of TiB_2/Al Combustion.Synthesis of Al-Ti-B System. *Materials Transactions*, **2002**, *43*(11), 2796–2801.

[2] Martin, R. and S.L. Kampe. Microstructure/Processing Relationships in Reaction-Synthesized Titanium Aluminide Intermetallic Matrix Composites. *Metallurgical and Materials Transactions A*, **2002**, *33A*, 2747–2753.

[3] Kuhlman, G.W. Forging of Titanium Alloys. ASM Handbooks Online. [Accessed 10/15/05]

[4] Lee, Seung-Hurn; Lee, Jong-Hyun; Lee, Yong-Ho; Shin, Dong Hyuk; and Kim, Yong-Seog. Effect of heating rate on the combustion synthesis of intermetallics. *Materials Science and Engineering*, **2000**, *A281*, 275–285.

[5] Xinghong, Z.; Qiang, X.; Jieaci, H.; and Kvanin, V.L. Self propagating high temperature combustion synthesis of TiB/Ti composites. *Materials Science and Engineering*, **2002**, *A348*, 41–46.

About the Authors

David Berry

David is a senior at Virginia Tech in the Materials Science and Engineering curriculum. He has been taking classes part-time while also maintaining a full-time, classified staff position as a Lab Instrument Technician within the same department. He has been employed with the department for nine years and will graduate in December 2006. He lives in Christiansburg, VA with his wife, Lori, and his son, Christian.

Michael Wooddell

Michael was born in Portsmouth VA, on March 4 1984. Michael attended Western Branch High School where he participated in National Honors Society and varsity wrestling. Virginia Tech was his first and only choice for college because he knew that it was the best engineering school in Virginia. Michael recently graduated with a B.S in Materials Science and Engineering from Virginia Tech in the summer of 2006 and is currently working on a M.S. degree in the same discipline. Michael hope to complete my thesis by the summer of 2007.

Join students, scientists and engineers from around the globe!

Become a student member of an MSE professional society:

MRS Materials Research Society

Materials Research Society

506 Keystone Drive
Warrendale, PA 15086-7573
Phone: 724-779-3003
Fax: 724-779-8313

Email: `info@mrs.org`

`http://www.mrs.org`

MATERIAL™ ADVANTAGE
The Student Program for Materials Science and Engineering

Material Advantage

provides a single low-cost student membership that provides access to the materials science and engineering professional's most preeminent societies:

- The American Ceramic Society (ACerS)
- Association for Iron & Steel Technology (AIST)
- ASM International
- The Minerals, Metals and Materials Society (TMS)

`http://www.materialadvantage.org`

The American Ceramic Society
www.ceramics.org

American Ceramic Society

735 Ceramic Place, Suite 100
Westerville, Ohio 43081
Phone: 866-721-3322
Fax: 614-899-6109

E-Mail: `info@ceramics.org`

`http://www.ceramics.org`

AIST
Association for Iron & Steel Technology

The Association for Iron & Steel Technology

186 Thorn Hill Road
Warrendale, PA 15086
Phone: 724-776-6040
Fax: 724-776-1880

Email: `info@aist.org`

`http://www.aist.org`

ASM International
The Materials Information Society

ASM International

9639 Kinsman Road
Materials Park, OH 44073-0002 USA
Phone: 800-336-5152 (U.S. and Canada)
800-368-9800 (Europe)
Fax: 440-338-4634

Email: `cust-srv@asminternational.org`

`http://www.asminternational.org`

TMS

The Minerals, Metals, and Materials Society

184 Thorn Hill Road
Warrendale, PA 15086-7514 USA
Phone: 800-759-4867 (U.S. and Canada Only)
724-776-9000 (Elsewhere)
Fax: 724-776-3770

E-Mail: `members@tms.org`

`http://www.tms.org`

UPCOMING MATERIALS CONFERENCES

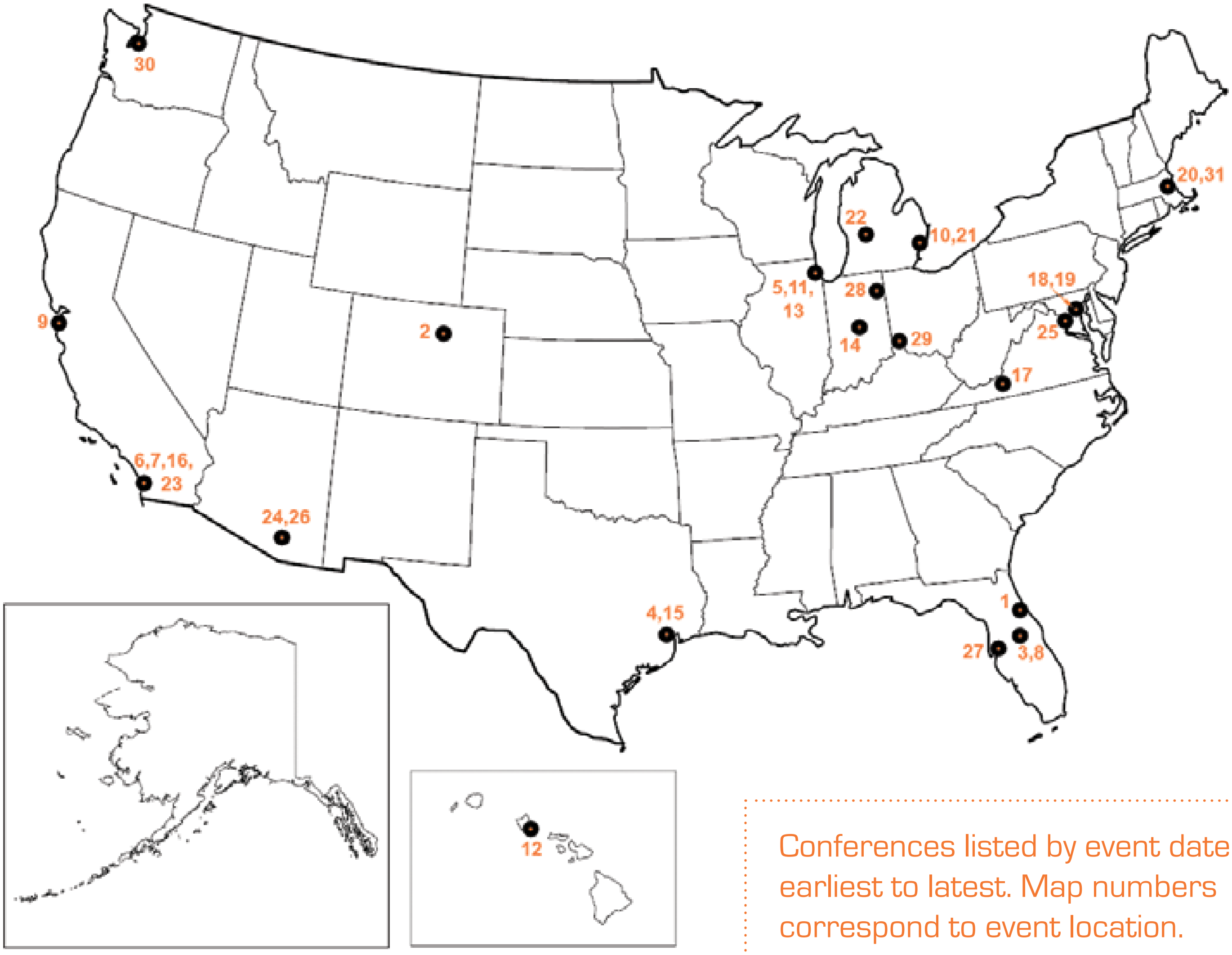

Conferences listed by event date, earliest to latest. Map numbers correspond to event location.

1) 31st International Cocoa Beach Conference & Exposition on Advanced Ceramics & Composites
January 21–26, 2007, Daytona Beach, FL
www.ceramicbulletin.org/calendar.asp

2) SME—Society for Mining, Metallurgy, and Exploration
2007 SME Annual Meeting & Exhibit and 109th National Western Mining Conference
February 25–28, 2007, Denver, CO
www.smenet.org/meetings/

3) TMS—The Minerals, Metals, & Materials Society
Annual Meeting
February 25–March 1, 2007, Orlando, FL
www.afsinc.org/Upcoming/Index.asp

4) SME—Society of Manufacturing Engineers
HOUSTEX 2007 Exposition & Conference
March 6–8, 2007, Houston, TX
www.sme.org/cgi-bin/events.pl?&&ENTER&rel&expo

5) ACS—American Chemistry Society
233rd ACS National Meeting
March 25–29, 2007, Chicago, IL
www.chemistry.org/portal/a/c/s/1/acsdisplay.html?DOC=meetings\calendar\calendr1.html

6) IEEE—Institute of Electrical and Electronics Engineers
Optical Fiber Communication Conference & Exposition & the National Fiber Optic Engineers Conference
March 25–30, 2007, Anaheim, CA
www.comsoc.org/confs/index.html

7) SME—Society of Manufacturing Engineers
WESTEC 2007 Exposition & Conference
March 26–29, 2007, Los Angeles, CA
www.sme.org/cgi-bin/get-event.pl?--001658-000007-020163--SME-

8) ASNT—American Society for Nondestructive Testing
16th Annual Research Symposium
March 26–30, 2007, Orlando, FL
www.asnt.org/events/events.htm

9) MRS—Materials Research Society
2007 Spring Meeting
April 9–13, 2007, San Francisco, CA
http://www.mrs.org/s_mrs/sec.asp?CID=4750&DID=164575

10) SAE—Society of Automotive Engineers

2007 SAE World Congress
April 16–19, 2007, Detroit, MI
www.sae.org/events/conferences/groundvehicle/

11) 2007 Society for Biomaterials Annual Meeting and Exposition

April 18–21, 2007, Chicago, IL
www.biomaterials.org/Calendar/calendar.htm

12) AIAA—American Institute of Aeronautics and Astronautics

48th AIAA/ASME/AHS/ASC Structures, Structural Dynamics, and Materials Conference
April 23–26, 2007, Waikiki, HI
www.aiaa.org/content.cfm?pageid=1

13) ECS—The Electrochemical Society

211th Meeting
May 6–11, 2007, Chicago, IL
www.electrochem.org/meetings/biannual/fut_mtgs.htm

14) AIST—The Association for Iron and Steel Technology

AISTech 2007
May 7–10, 2007, Indianapolis, IN
http://www.aistech.org/

15) AFS—American Foundry Society

111th Metalcasting Congress
May 15–18, 2007, Houston, TX
www.afsinc.org/Upcoming/Index.asp

16) SEI/ASCE—Structural Engineering Institute/American Society of Civil Engineers

2007 Structures Conference
May 16–20, 2007, Long Beach, CA
www.seinstitute.org/services/conferences.cfm

17) ASCE—American Society of Civil Engineers

18th Engineering Mechanics Division Conference
June 3–6, 2007, Blacksburg, VA
www.ce.jhu.edu/emd/news.html

18) SAMPE—Society for the Advancement of Materials and Process Engineering

SAMPE 2007 Symposium & Exhibition
June 3–7, 2007, Baltimore, MD
www.sampe.org/events/calendarevents.aspx

19) ASM International

18th Aeromat Conference & Exposition
June 25–28, 2007, Baltimore, MD
www.asminternational.org/aeromat07/

20) ACS—American Chemistry Society

234th ACS National Meeting
August 19–23, 2007, Boston, MA
www.chemistry.org/portal/a/c/s/1/acsdisplay.html?DOC=meetings\calendar\calendr1.html

21) MS&T '07

September 16-19, 2007, Detroit, MI
www.ceramicbulletin.org/calendar.asp

22) SME—Society of Manufacturing Engineers

Great Lakes 2007 Exposition & Conference
September 18–20, 2007, Grand Rapids, MI
www.sme.org/cgi-bin/events.pl?&&ENTER&rel&expo

23) BMES—Biomedical Engineering Society

Annual Fall Meeting
September 26–29, 2007, Los Angeles, CA
www.bmes.org/meetings.asp

24) SME—Society for Mining, Metallurgy, and Exploration

2007 Precious Metals Symposium
October 3–6, 2007, Tucson, AZ
www.smenet.org/meetings/

25) ECS— The Electrochemical Society

212th Meeting
October 7–12, 2007, Washington, DC
www.electrochem.org/meetings/biannual/fut_mtgs.htm

26) The Aluminum Association 74th Annual Meeting

October 15–16, 2007, Tucson, AZ
www.afsinc.org/Upcoming/Index.asp

27) ACMA—American Composites Manufacturing Association

Composites 2007
October 17–19, 2007, Tampa, FL
www.plasticsnews.com/subscriber/datebook/dbshow.html?id=1051215096

28) AFS—American Foundry Society

Midwest Regional Conference
October 21–23, 2007, Fort Wayne, IN
www.afsinc.org/Upcoming/Index.asp

29) SAMPE—Society for the Advancement of Materials and Process Engineering

SAMPE 2007 Fall Technical Conference
October 29–November 1, 2007, Cincinnati, OH
www.sampe.org/events/calendarevents.aspx

30) ASME—American Society of Mechanical Engineers

International Mechanical Engineering Congress & Exposition
November 11–16, 2007, Seattle, WA
calendar.asme.org/EventDetail.cfm?EventID=698

31) MRS—Materials Research Society

2007 Fall Meeting
November 26–30, 2007, Boston, MA
http://www.mrs.org/s_mrs/sec.asp?CID=2073&DID=92005

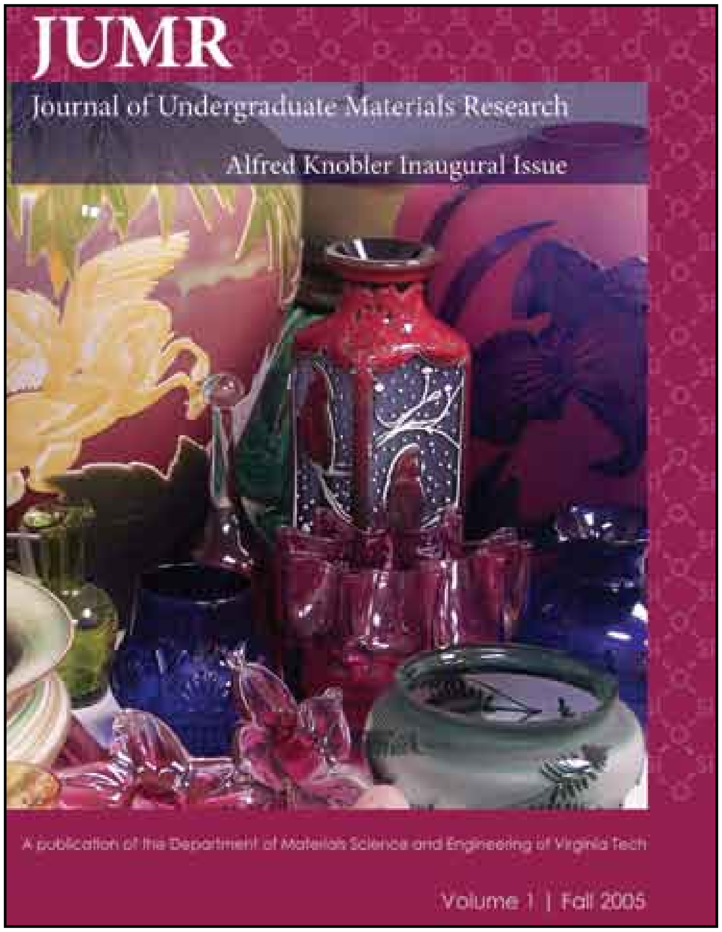

JUMR

Journal of Undergraduate Materials Research

Alfred Knobler Inaugural Issue

A publication of the Department of Materials Science and Engineering of Virginia Tech

Volume 1 | Fall 2005

Publish. Gain recognition.
Be part of something exciting.

Submit your paper for consideration in Volume 3

If you are an undergraduate student at any institution working on a materials-related project, here is your chance to become published. Your submitted paper will undergo a peer-review for consideration in Volume 3 of the *Journal of Undergraduate Materials Research*. Please submit your manuscripts by **5:00 PM**, **May 4, 2007.**

For submission requirements, see:
http://www.jumr.mse.vt.edu

Manuscripts or questions should be sent to:

JUMR
213 Holden Hall
Virginia Tech
Blacksburg, VA 24061
jumr@mse.vt.edu

JUMR
213 Holden Hall
Virginia Tech
Blacksburg, VA 24061
Email: jumr@mse.vt.edu
Website: www.jumr.mse.vt.edu
Fax: (540) 231-8919

Non-profit organization
U.S. Postage PAID
Blacksburg, VA 24060

Permit No. 28